Radiation Effects on Metal Fe and Core-Shell Ti-TiO_2 Nanoparticles by Molecular Dynamics Simulation

A Dissertation

Presented in Partial Fulfillment of the Requirements for the

Degree of Doctor of Philosophy

with a

Major in Physics

in the

College of Graduate Studies

University of Idaho

by

Mohammad Zahidul Hossain Khan

Approved by:

Major Professor: You Qiang, Ph.D.

Committee Members: Indrajit Charit, Ph.D.; Leah Bergman, Ph.D.; Ruprecht Machleidt, Ph.D.

Department Administrator: John Hiller, Ph.D.

December 2021

Abstract

Nanoparticles, due to their small size and radiation absorption property, are widely used in nano nuclear nanotechnology as well as radiation environment. Radiation-induced defects could negatively affect mechanical properties, potentially leading to accidents. In this study, the molecular dynamics (MD) method, as a powerful atomic-level simulation tool, is applied to investigate and characterize the formation and evolution of point defects in irradiated Fe nanoparticle (NP) and core-shell Ti-TiO_2 NP by using a recent updated many-body interatomic potential. MD especially helps us gain access to length and time scales that are not accessible experimentally and learn more about the multi-scale phenomena that occur during the irradiation of nanomaterials. Computer simulations provide information at the microscopic level, acting as a bridge to the experimental observations and giving insights into processes that take place at small time and length scales. The increasing computer capabilities in combination with recently developed scalable codes, and the availability of realistic potentials set the stage to perform large scale simulations, approaching phenomena that take place at the atomistic and mesoscopic scale in a more realistic way. This dissertation has focused on understanding the atomic-level mechanism of irradiation damages and defect formations in Fe nanoparticle (NP) and core-shell Ti-TiO_2 NP. To test the NPs compatibility for several neutron energy and temperature stability, a series of MD simulations have been done for Fe NP and core-shell Ti-TiO_2 NP. The results from the simulation provide the defect orientation on NP after irradiation and can be used to predict the experimental results.

Acknowledgements

At first, I thank Almighty Allah for all His blessings and give Him all the glory. I would like to acknowledge the Department of Physics at the University of Idaho (UI) for allowing me to study and work as a Teaching/Research assistant in the state of Idaho. I want to give a million thanks to my supervisor, Prof. You Qiang, for his constant support, tremendous encouragement, valuable advice, and timely guidance, which urged me to continue with my studies at the graduate level successfully and motivated me to perform research effectively at UI. From my PhD, my supervisor teaches and helps me much more than what a professor does, more like a parent educating and caring for his children, which makes me enjoy my research and life. His sincere attitude in science and optimism for life will affect me forever. From the bottom of my heart, I would like to say: “thank you so much, my dear professor; I am so lucky to meet you in my life”. I owe great thanks to Matthew W Anderson and Stephanie J. Parker from INL for their precious help for INL high-performance computing (HPC) through the Idaho national lab user facility projects.

I am grateful to Dr Indrajit Charit for teaching and giving me an insight into the radiation-induced defects in materials and fundamentals of nuclear materials during my study here at UI. I want to thank my family members, particularly my father MD Delwar Hossain Khan, my mother Jahanara Khanam, my wife Gulshan Ara Parvin Jui for being with me during difficult times, motivating me in my career. I also would like to convey my special love and gratitude to my brother and sister for their love, patience, support, encouragement, and prayers. I am grateful to all my friends in the Moscow-Pullman community and Palouse area for their constant support, encouragement, and prayers. At this time, I think of all my friends, relatives,

and well-wishers in Bangladesh and around the world, who played a vital role in my life in so many ways and shaped me to be the person I am today.

My completion of this project could not be accomplished without the support of my lab colleague Dr Lokendra Khanal, who have continuously supported and guided me during my PhD time. I would like to thank my fellow group members and friends Mr Ahmed Alalnazi, Mr Rabindra Khannal, for their constant support and cooperation.

Dedication

This is dedicated to my beloved parents MD Delwar Hossain Khan, Jahanara Khanam and my wife, Gulshan Ara Parvin Jui

Table of Contents

List of Figures

Statement of Contribution

Coauthors for this works are Dr. Lokendra Khanal, Rabindra Khanal, Jinming Zhang and You Qiang. The conceptualization for this project was supervised by my graduate advisor Dr. You Qiang. Simulation design, data works, and analysis were completed by me. The original draft was developed by me, and review and editing were conducted as a joint effort by Dr. Ruprecht Machleidt, Dr. Indrajit Charit, Dr. Leah Bergman and Dr. Qiang.

Chapter 1: Introduction to Radiation Effect on Nanoparticles

1.1 Nanoparticles and Nuclear Nano Technology:

The word nanotechnology is defined as "particles with two or three dimensions less than 100 nm and of a size greater than 1 nm and not exhibiting a size-related intensive characteristic". Nanoparticles are also defined as zero-dimensional nanomaterials, distinguished from one- and two-dimensional nanomaterials, which have dimensions larger than nanoscale. The differences between them and their bulk counterparts are based on size, chemical reactivity, mobility, energy absorption, etc[1]. Many bottom-up and top-down strategies have been developed over time, each giving the researchers a certain degree of flexibility to construct NPs with the desired capabilities. NPs can be categorized into various types based on their synthesis materials. Based on the nature of the parent material and other factors, different types of NPs have distinct properties and target applications. NPs have a range of properties depending on the synthesis strategy and experimental conditions, such as their size, shape, and surface area. The synthesis conditions can be modified to produce shape- and size-controlled NPs[2].

A significant benefit of nanotechnology is the ability to tailor the structures of materials at microscopic scales to achieve specific properties, thus greatly extending materials science's toolkit. Materials can be made stronger, lighter, more durable, more reactive, more sieve-like, or better electrical conductors, among many other characteristics, with nanotechnology. Along with various applications such as biomedical, environmental, sports, electronics, NPs also used in the nuclear industry.

The Nano-Nuclear Technology (NNT) focuses on applying nanomaterials to enhance nuclear energy capabilities and safety and bring new generations of power plants and a new advanced civilization. In the history of humanity, many lessons have been learned through the development of nuclear technology. Some of these lessons have been more significant than those gained through non-nuclear power stations. Around the world, scientists are working on various methods to achieve this goal, including Nano-Nuclear technology as an effective and efficient means to secure utmost safety and performance. Here are some of our most influential focuses in the nuclear fuel cycle, including the use of nanoparticles, nanostructured materials, and nano-processes to enhance mechanical, chemical, physical, and thermo-hydraulic properties.

Nanostructured-ODS Materials - There is potential to improve radiation tolerance and mechanical performance by using (in-core) materials like oxide dispersions strengthened (ODS) materials.

Nano-Scale Coatings - It is possible to include nanoscale coatings on the exterior or the interior of the fuel cladding to improve corrosion resistance, surface hardening, and pellet interaction on the cladding interior.

Nanomaterials for Fission Product Capturing - The use of nanoparticles and/or nano-porous materials on reprocessing operations and within reactor core assemblies can allow for the capture of fission product gases and, therefore, reduce the likelihood of releases during normal operations or accidents.

Nanotechnology Engineered Fuels - Nanotechnology integrated materials designed and/or engineered with enhanced fission gas retention, plasticity, radiation tolerance, heat transfer

capabilities, and reduced chemical and mechanical interactions with fuel cladding longer service lives reduced failure rates in typical or accident environments.

Nano Radiation Sensors, Detectors and Monitors - Sensors, detectors, and/or in-service monitors with nanotechnology that can measure radiation, temperature, pressure, material properties, corrosion, neutron flux, stress/strain, or even chemical composition with minimal impact on the system performance and with significantly improved sensitivity, performance, and functionality.

Nano Nuclear Waste separation - For reprocessing and reusing nuclear waste, chemical interaction and separation methods utilizing nanoparticles and nano porous materials are employed to isolate actinides from the wreckage.

1.2 Nuclear Radiation:

A common phenomenon in nature is radiation. The sources of cosmic radiation and terrestrial igneous decay are both factors contributing to their formation. The semiconductor and nuclear industries are notable examples of areas where radiation effects are finding increasing applications. A nuclear power application will expose materials to high-dose irradiation from highly energetic fission and fusion products. Fission products of existing nuclear power plants are converted into heat and electricity through thermodynamic conversion. In the future, thermonuclear reactions will provide energy for fusion reactors. In these applications, the particles' energy is converted into valuable energy by heating the material. Still, at the same time, it damages the material and compromises the properties essential for reactor operation, including mechanical, thermal, transport, and other properties. This is one of the central issues for fusion reactors where metal structural components must

withstand high neutron fluxes and radiation such as helium, which is intensely discussed[3–5]. Similarly, fission products, such as heavy nuclei and neutrons, and alpha decay processes, which produce heavy radioactive nuclei and alpha particles, may damage nuclear reactor materials. A further problem facing the nuclear industry relates to radiation damage in materials intended to encapsulate long-term radioactive waste[6–12]. Moreover, the public acceptance of nuclear power depends on the ability to immobilize nuclear waste.

1.3 Basic of Radiation Effects:

The radiation process involves the emission of energy by one body, which travels through a medium or through space to be absorbed by another body. Radiation refers to the emission of energy by microscopic particles, called photons. Radiation interacts with matter employing the fundamental interactions in our nature, primarily the electromagnetic (for charged particles and photons) and strong interactions (for hadrons). Generally, radiation falls into two categories: ionizing radiation and non-ionizing radiation. Radiation ionizing produces ion pairs, such as neutrons, protons, pion, muons, etc., which are not visible to the human eye, and appropriate instruments must detect that. Since neutrons are neutral particles, they do not ionize directly, but they produce ions through secondary mechanisms. The energy carriers in non-ionizing radiation do not generate ions in a physical medium, such as soft ultraviolet, infrared, visible light, microwave, radiofrequency, etc.

Radiation damage occurs when energetic particles displace atoms, which also replaces other atoms in the system. A collection of these atoms are often referred to as a “collision cascade"[13–15]. An average collision cascade produced by a 100 keV particle can spread and relax in a matter of picoseconds, spanning nanometers. As a result of these structural damages, amorphous pockets and point defects with their clusters and the evolution of these

defects over time determine how much the material's mechanical and thermal properties have been altered. For example, radiation-induced defects and their structures can reduce the materials' thermal conductivity, resulting in inefficient energy transfer in fission and fusion reactors, heat localization, and other undesirable effects, such as brittleness.

1.4 Importance of Molecular Dynamics (MD) Simulation:

The development of physical models is required to understand significant aspects of radiation interaction with solids, including radiation effects, defect investigation, ion-beam modification, electronic and ionic transports, materials characterization, and predicting the materials' behaviour under intense radiation environments[16]. Simulation can provide insights into the microscopic level that are not obtained by experiments. Computer simulation is a modern tool to study such phenomena.

Molecular dynamics (MD) provides access to the trajectory of the system in phase space. MD simulations solve the equation of motion F = ma numerically, describing the system at any time. In this regard, MD modelling is helpful when studying radiation damage in materials, as it provides detailed information on atomic-scale damage on time and length scales.

Radiation damage has been the subject of previous MD simulations that have provided interesting insights[17–20]. Although the size of the system limits MD simulations, the reported results are limited to energies of about 100 keV. For a particle moving with a velocity equivalent to high energy within an MD simulation box, a larger box size is required to accommodate the penetration path of the projectile. Until recently, computer resources only allowed for simulations of small systems, resulting in lower energy events. Energies relevant

to fission products and fusion have not been studied yet are essential to simulate and give us a more realistic view of the effects of high energy irradiation on matter[20]. The impact of iron knock-on atoms on 14 MeV neutrons in fusion reactors can produce energy of up to 1 MeV, with an average energy of approximately 0.5 MeV[20]. The fission products of nuclear reactions have energies between 50 and 100 MeV, transferring high energy to the surrounding material. It has been emphasized that realistic energy cascade simulations are necessary, which can contain novel qualitative characteristics.

1.4 Research Scope:

Previous documentation showed that core-shell NPs with oxide as the shell and metal NP as the core possess very sensitive electrical conductivity and magnetic properties even under an extremely low dose ion flux regime with hardly any effect of temperature up to 200 °C.[21]. Also, studies revealed that the core-shell arrangement of NPs is reduced under irradiation. Nanomaterials with core-shell cores are highly functional nanomaterials with modified properties. The ratio between the core and shell can be altered to alter the properties. Core-shell nanoparticles contain an interface between the core and shell, which acts as a defect sink[22]. When irradiating a defect, it is necessary to know how it reaches the surface or interface and how it is distributed. By analyzing this information, we can learn why the size of the core-shell structure changes when radiation is present.

1.5 Outline:

Chapter 2 primarily discusses the effects of irradiation on the properties and structures of nanomaterials. An overview of nanostructures' behaviour under the influence of high energy ions and neutrons is presented, along with some microscopic approaches and MD modelling results.

In Chapter 3, we give a brief overview of MD simulations. There are also descriptions of the basic features used in this thesis' simulations, as well as how the LAMMPS code's implementation works.

In Chapter 4, we study collision cascades in Fe NP caused by recoils that carry up to 40 keV of energy from high-energy neutrons radiation. We simulate collision cascades for different directions of the recoil in a system consisting of about 144431 atoms. A series of 6 cascades for each primary knock-on atom (PKA) energy (5 keV, 10 keV, 20 keV, 30 keV and 40 keV) was simulated to assure statistical precision. We describe the large-scale damage by describing the morphology of the cascade, and we discuss the damage mechanisms. Defect analysis is summarized, and new defect structures that have not been experimentally observed are presented.

In chapter 5, the radiation effect on core-shell Ti-TiO_2 nanoparticles is studied by using molecular dynamics simulations. A series of several cascades for each neutron recoil energy (50 keV, 100keV, 150keV, 200keV and 250 keV) for several temperatures (100 K, 300 K and 500 K) is simulated assure statistical precision. From these simulations, it has been observed that radiation creates a small number of defects. The defects are either single SIAs or Vs. In each of the cases, many defects accumulate both in the surface and interface zone. In all cases, the core remains intact, but the mean square displacement for core-shell NP changes with increasing recoil energy.

1.6 Reference:

1. Murthy, S. K. Nanoparticles in modern medicine: state of the art and future challenges. *Int. J. Nanomedicine* **2**, 129–41 (2007).

2. Sun, S. & Zeng, H. Size-controlled synthesis of magnetite nanoparticles. *J. Am. Chem. Soc.* **124**, 8204–8205 (2002).

3. Dudarev, S. L. *et al.* The EU programme for modelling radiation effects in fusion reactor materials: An overview of recent advances and future goals. *J. Nucl. Mater.* **386**–**388**, 1–7 (2009).

4. Stoneham, A. M., Matthews, J. R. & Ford, I. J. Innovative materials for fusion power plant structures: Separating functions. *J. Phys. Condens. Matter* **16**, (2004).

5. Ward, D. J. & Dudarev, S. L. Economically competitive fusion. *Mater. Today* **11**, 46–53 (2008).

6. Covill, A., Hyatt, N. C., Hill, J. & Collier, N. C. Development of magnesium phosphate cements for encapsulation of radioactive waste. *Adv. Appl. Ceram.* **110**, 151–156 (2011).

7. Bingham, P. A., Connelly, A. J., Cassingham, N. J. & Hyatt, N. C. Oxidation state and local environment of selenium in alkali borosilicate glasses for radioactive waste immobilisation. *J. Non. Cryst. Solids* **357**, 2726–2734 (2011).

8. Lee, W. E., Ojovan, M. I., Stennett, M. C. & Hyatt, N. C. Immobilisation of radioactive waste in glasses, glass composite materials and ceramics. *Adv. Appl. Ceram.* **105**, 3–12 (2006).

9. Geisler, T., Trachenko, K., Ríos, S., Dove, M. T. & Salje, E. K. H. Impact of self-irradiation damage on the aqueous durability of zircon (ZrSiO4): Implications for its suitability as a nuclear waste form. *J. Phys. Condens. Matter* **15**, (2003).

10. Weber, W. J. & Rubia, T. D. De. <1998_Weber_JMR.pdf>. **13**, (2008).

11. Ringwood, A. E. *et al.* Immobilization of high-level nuclear reactor wastes in SYNROC: A current appraisal. *Nucl. Chem. Waste Manag.* **2**, 287–305 (1981).

12. McGann, O. J. *et al.* The effects of γ-radiation on model vitreous wasteforms intended for the disposal of intermediate and high-level radioactive wastes in the United Kingdom. *J. Nucl. Mater.* **429**, 353–367 (2012).

13. Nordlund, K. Computational materials science of ion irradiation. *Nucl. Instruments Methods Phys. Res. Sect. B Beam Interact. with Mater. Atoms* **188**, 41–48 (2002).

14. Granberg, F. *et al.* Mechanism of Radiation Damage Reduction in Equiatomic Multicomponent Single-Phase Alloys. *Phys. Rev. Lett.* **116**, 1–8 (2016).

15. Souidi, A. *et al.* Dependence of radiation damage accumulation in iron on underlying models of displacement cascades and subsequent defect migration. *J. Nucl. Mater.* **355**, 89–103 (2006).

16. Sherwood, P. *et al.* QUASI: A general purpose implementation of the QM/MM approach and its application to problems in catalysis. *J. Mol. Struct. THEOCHEM* **632**, 1–28 (2003).

17. Calder, A. F., Bacon, D. J., Barashev, A. V. & Osetsky, Y. N. Computer simulation of cascade damage in α-iron with carbon in solution. *J. Nucl. Mater.* **382**, 91–95 (2008).

18. Morishita, K. & Diaz De La Rubia, T. A molecular dynamics simulation study of displacement cascades in vanadium. *J. Nucl. Mater.* **271**–**272**, 35–40 (1999).

19. Bacon, D. J., Osetsky, Y. N., Stoller, R. & Voskoboinikov, R. E. MD description of damage production in displacement cascades in copper and α-iron. *J. Nucl. Mater.* **323**, 152–162 (2003).

20. Stoller, R. E. & Greenwood, L. R. Subcascade formation in displacement cascade simulations: implications for fusion reactor materials. *J. Nucl. Mater.* **271**–**272**, 57–62 (1999).

21. Jiang, W. *et al.* In situ study of nanostructure and electrical resistance of nanocluster films irradiated with ion beams. *Adv. Funct. Mater.* **24**, 6210–6218 (2014).

22. Beyerlein, I. J., Demkowicz, M. J., Misra, A. & Uberuaga, B. P. Defect-interface interactions. *Prog. Mater. Sci.* **74**, 125–210 (2015).

Chapter 2: A Literature Review of Computational Simulation of Radiation Effect on Nanomaterials

2.1 Introduction:

Nanomaterials (NMs) are materials where at least one dimension is less than 100 nanometers. In this nanoscale, unique optical, magnetic, electrical and other properties emerge, which shows the potential for significant impacts in applications of electronics, medicine, radiation protection and other fields[1]. Over the past few years, NMs have been discovered for potential applications in various areas, including drug delivery, enhanced magnetic resonance imaging, information storage, reduction of carbon dioxide, groundwater remediation and nano-nuclear technology[2–6].

Nano-Nuclear Technology (NNT) deals with using the latest engineered nanomaterials in each phase of the nuclear fuel cycle to improve nuclear power performances and safety, bringing new generations of nuclear power units, and a new advanced technological civilization. The use of nanoparticles, nano-structured materials, and/or nano-processes to enhance mechanical, chemical, physical, or thermo-hydraulic properties and performance in nuclear fuel cycle applications, such as: a) Nanostructured-ODS materials that could improve mechanical performance as well as radiation tolerance, b) Nano-Scale coatings that could be included on the exterior or the interior of fuel cladding to improve corrosion resistance and surface hardening, and pellet-clad interactions on the cladding interior, c) Nanomaterials for fission product capturing that can enable techniques to capture fission product gases either from reprocessing operations or directly within a reactor fuel assembly thereby reducing the potential for releases from normal or accident conditions, d) Nano-Technology engineered

fuels that enable longer service lives, reduce fabrication process losses, and/or reduce the potential for failure in normal or accident conditions including increased fission gas retention, plasticity, radiation tolerance, heat transfer capability, as well as reduced fuel cladding chemical and/or mechanical interactions, e) Nano Radiation Sensors, detectors and monitors that can directly monitor for radiation, temperature, pressure, in situ diagnostics of material properties and mechanical response, corrosion, neutron flux, stress/strain or even chemistry with little effect on system performance with significantly reduced size and weight and increased sensitivity, performance, and functionality, and f) Nano nuclear waste separation that utilities nanoparticles and/or nano-porous materials for separating the actinides and other radioactive elements from the nuclear waste for reprocessing and reusing.

A typical picture of a solid body with radiation defects will give a better idea. In general, when high energy ions and neutrons irradiate any material, a partial energy transfer to the displaced atoms of crystalline lattice, which guides the formation of primary knocked-out particles (PKA). This process produces displacement cascades containing the Frenkel pairs because of a process in which an atom is displaced from a lattice site, coming to rest some distance away from its initial position. An initially occupied lattice site becomes a vacancy, and the atom that occupied the site becomes embedded in the lattice far away from its original position, forming a SIA defect. When these defects gather any places named cluster defects, it creates a vacancy loop or nanopores and dislocations. The point defects can collide and annihilate both at meeting each other along grain boundaries (GBs (A grain boundary (GB) is the interface between two grains or crystallites)), which can act as sinks for radiation defects. High intense radiation on materials conducts the following general effects based on

the material structure, properties, and content: amorphization; radiation hardening; high-temperature creep growth; material swelling; and some nuclear reactions and decays[7]. Compared to coarse-grain (CG) materials, the production of radiation defects, development and properties in various NMs, is relatively trivial since many of these studies are still in their infancy[8,9]. In the presence of a developed interface system in nanomaterials, the chance of radiation defect sinks increases and decrease the radiation effects, whereas this accumulation of radiation defects at GBs can introduce the nanostructure amorphization process during the displacement cascade development.

Here we mainly focus on radiation effect observation by using molecular dynamics simulation. We also include density functional theory (DFT), Monte Carlo simulations (MCS) and Rate theory for observing the radiation effect on nanomaterials. MD simulations can model the creation and evolution of collision cascades that are not accessible experimentally from time and length scales. DFT uses electronic configuration and MCS applies probabilistic theory to predict the radiation defect. The rate theory is for the amorphization process for nanostructured material. The internal observation from these simulations is vital for understanding the main physical phenomena during radiation damage and their effect on material properties.

Molecular dynamics is a simulation tool that has become a standard method for modelling materials at the atomistic level. MD simulates the time evolution of a system of classical particles by repeatedly solving Newton's second law of motion for each particle; It simulates the trajectories of individual particles rather than the material's bulk properties. In an MD

simulation, time is first discretized (i.e., represented by a discrete set of times t_i, where i = 0, 1, 2, and such that each time t_i is separated by a defined time interval Δt. Assuming that at some time t_i, the positions $\mathbf{r}(t_i)$, velocities $\mathbf{v}(t_i)$, and masses m of the particles are known, the MD algorithm will proceed as follows: 1) Using a user-provided potential V (r_0, r_1, $r_{2, \ldots}$), the net force $\mathbf{F} = -\Delta\mathbf{V}$ on each particle is computed at time step t_i. 2) Using Newton's second law $\mathbf{F} = \mathbf{ma}$, the acceleration of each particle is computed at time step t. 3) Using the acceleration $\mathbf{a}(t_i)$, the position $\mathbf{r}(t_i)$, and the velocity $\mathbf{v}(t_i)$ of the particles at the next time step, $r(t_i + 1)$ and $v(t_i + 1)$, are computed. 4) Steps 1-3 are repeated for time step t_i+1. The smaller the time step is, the more accurate is the solution of the equations of motion. After the changes have been performed, the process is continued by calculating the forces in the new positions. Molecular simulations' predictive power is primarily affected by the force field or interaction function used, and the degree of sampling applied to the relevant configurational degrees of freedom. Consequently, they determine how various accurate properties can be calculated from trajectories or configurational ensembles. Nonetheless, inadequate thermodynamic or spatial boundary conditions or simulation input parameters may compromise the accuracy of a simulation based on a properly calibrated force field and extensive sampling[10].

2.2 Threshold Displacement Energy:

Threshold displacement energy (TDE) is the minimum kinetic energy that an atom in a solid need to be permanently displaced from its lattice site to a defect position. It is also known as displacement energy (DE) or threshold energy (TE). The velocity of the recoil atom is much higher than the thermal velocity. One can imagine that produced defect depends only on its incident energy, but one model illustrated that TE depends on the direction of the recoil and

crystal lattice[11]. Several studies have investigated threshold displacement energy (TDE) probabilities to account for the radiation damages[12–14]. Bai and Uberuaga[15] have shown the defect productions depend on the initial distance of the PKA from the grain boundary after being used 2 keV Ti PKAs with grain boundaries at 300K and 1000K. They also found that fewer interstitial clusters produce at 1000K than 300K because of higher atomic mobility. The threshold energies are observed to occur very roughly around the crystal direction <1 2 3> found in Nordlund et al. [16]. In a study by Trachenko et al.[17,18], using uranium projectiles with 40 and 100 keV to observe radiation damage, they found point defects were produced, and atoms were displaced due to the radiation damage cascade. As opposed to PKA's initial distance, they found that the proportion of oxygen defects to titanium defects changes during the radiation cascade and that interstitials are best concentrated at the periphery of the cascade. Cluster analysis of the MD simulation confirms that the cluster of vacancies contains 10000 vacancies during the ballistic phase, whereas less than 1000 vacancies are present during the annealing phase[19]. L. A. Zepeda-Ruiz et al. [20] showed that TDE for vanadium varies from 13 to 51 eV, depending on the orientation and is nearly temperature independent between 100 K and 900 K. The lowest TDE is in the <1 0 0> direction. In addition, the study found that TDE is also direction-dependent for GaN, in agreement with experimental findings[21]. The other study showed that TDE varies with temperature as well[22]. Although this temperature effect is associated with thermally induced correlated recombination, it cannot be considered for primary radiation damage.

2.3 Radiation Damage in Nanocrystalline Metals, Non-metal and Amorphous:

Most of the computational simulation work to date have focused on the radiation response of nanocrystalline (NC) on pure metal systems from the literature review. Still, little work in NC metallic alloys systems will also be highlighted.

2.3.1 Radiation Damage in Metallic Nanomaterial:

Radiation damage in metals has been studied extensively last few years [23–25]. Metallic materials are widely used in nuclear reactors as structural materials, including nickel, copper alloy and austenitic stainless steels. In most cases, pure metals are irradiated as model systems, where the consequences of chemical reaction do not need to be considered. Radiation damage and its role in irradiation-induced changes in material properties depend on the crystal structures such as Body centred cubic (BCC), Face centred cubie (FCC) and Hexagonal closed packed (HCP). Nevertheless, the important parameters are not only the total number of Frenkel defects per cascade but also the population distribution within clusters, as well as the form and mobility of these clusters like faulted dislocation loop (faulted dislocation loops nucleate and grow because of the high mobility of interstitials), sessile loop (immobile dislocations called sessile) and glissile loop (mobile dislocations known as glissile). Bacon and his coworkers [26] have shown that self-interstitial atoms form clusters in the cascade process in all metals, and the extent of this clustering does appear to vary from metal to metal. Vacancy clustering is also variable. The mobility of all clusters depends on their dislocation character, crystal structure and stacking fault (a stacking fault is a planar defect that can occur in crystalline materials) energy. An analysis of cluster defects in different crystal structures is presented below based on MD simulations.

Multiple studies have been conducted regarding BCC metals and the requirement for a certain amount of energy in both defect formation and defect migration. According to BCC metals, the vacancies migration and vacancy formation energy are 0.5-2 eV and 1.6-3 eV, respectively. The BCC metals' high stacking flaw energies prevent large flaw dislocation loops from forming[27]. BCC metals have sessile loops with {1 0 0} habit planes with b = a <1 0 0>, whereas glissile loops have {1 1 0} habit planes with b = a/2 <1 1 1>[26]. Radiation damage in BCC Fe has been vastly investigated by simulations[24,28]. Moreover, E Zarkadoula et al. [24] demonstrated that three different types of damage were produced and relaxed, including reversible deformation by elastic expansion, irreversible structural damage by ballistic displacement, and smaller reversible deformation by shock waves. Nevertheless, MD simulation studies suggest that the interaction between two ½<1 1 1> loops could have several possible scenarios, one of which leads to the formation of <1 0 0> loops[24,29].

FCC: In FCC metals, vacancy migration energy varies from 0.7 to 1.7 eV, generally 50-70% less than the vacancy formation energy, and interstitial migration energy is 0.05-0.1 eV, which is significantly less than vacancy migration energy. It is well known that interstitials are more mobile even at room temperature, whereas vacancies generally move at high temperatures. This temperature-dependent property of defects has a good impact on the accumulation of radiation damage and void swelling in FCC metals and alloys. The Stacking fault tetrahedron (SFT) is another intriguing defect, often observed in irradiated FCC metals. MD simulations have observed the formation of SFTs. The Silcox-Hirsch mechanism showed that SFTs could emerge from vacancy clusters during MD simulations [30]. It has been demonstrated in several collision cascades that the stability of SFTs and loops and the

proximity of clusters of different natures influence defect formation when one cascade overlaps debris from another, as illustrated in Figure. 2.1a [25].

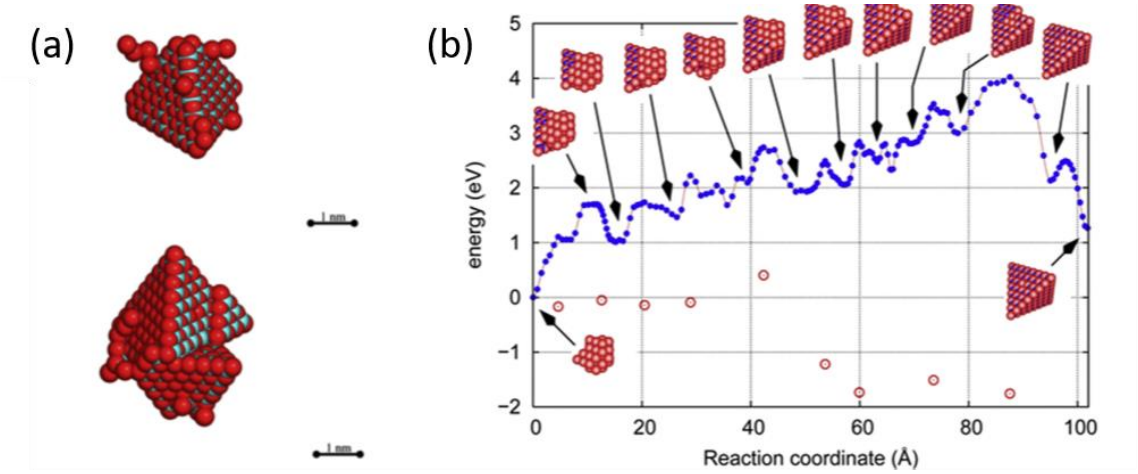

Figure 2. 1 (a) MD simulations on the formation and evolution of regular SFT and two adjunct SFTs in Cu[25]. (b)MD simulations show the development of a void into an SFT[31].

Additionally, the MD simulations reveal that vacancy clusters evolve even into void originating SFTs rather than Frank loops, as seen in Figure 2.1b. Even though entropy is a barrier to this transformation, an increase in potential energy is a factor[31]. From room temperature to below 600 K, 40% of the vacancy clusters contain more than three vacancies, while 80% of the interstitial clusters contain more than four interstitials[25]. Radiation temperatures that increase lead to a decline in vacancy cluster fractions, while radiation temperatures that increase lead to a rise in interstitial cluster fractions[25].

HCP: For light water reactors, HCP alloys based on Zr are employed as fuel cladding tubes, and MD simulations can be used to examine the effect of radiation on HCP materials. Metal HCP systems have more complex vacancies and interstitials than cubic systems. For

vacancies, the formation and migration energies are typically 0.6–2 eV and 0.3–1 eV, respectively. Based on [32,33], the formation of monovacancies generally ranges from 0.78 to 0.97 Ω. Zr has smaller activation energy for self-diffusion in the non-basal plane than Mg or Co, with less than the ideal ratio of c/a [32,33], and the vacancy migration occurs more isotopically for Mg and Co.

2.3.2 Radiation Damage in Non-metallic Nanomaterials:

MD Radiation studies on non-metallic NC materials are comparably limited to metallic materials. Radiation damage evolution, sintering, and many other technologically essential applications rely on how point defects interact with grain boundaries in oxides. As demonstrated by $MgAl_2O_4$, oxide grain boundaries can enhance annihilation of point defects, which causes zones of interstitial dislocation loops to vanish near boundaries, with greater porosity near grain boundaries under different radiation conditions[34]. In comparison with large grain counterparts, nanocrystalline oxides tend to be more radiation-tolerant[35]. Despite the importance of these interactions, there are many unanswered questions, especially regarding how boundaries that may be damaged during the irradiation process interact with residual defects throughout the grain. Blas Pedro Uberuaga et al. showed that how vacancies interact with three different grain boundaries in MgO. They compared the vacancy interaction with both pristine and 'damaged' boundaries. They found that the excess interstitials significantly changed the interaction of the vacancies with the boundaries, and this change was sensitive to the atomic structure of the boundary. They also observed the complex electrostatic effects dominate the interaction and boundaries absorb defects [34]. On a much shorter timescale, MD simulations can predict the disorder-based mechanisms

governing grain growth in ceramics, including ceramic oxides [36]. The mechanism described by Dilpuneet S. Aidhy and his colleagues observed the fast grain growth experimentally under both material synthesis and irradiation conditions.

2.3.3 Radiation Damage in Amorphous Nanomaterials:

In contrast to metallic and non-metallic materials, amorphous nanomaterials are very difficult to simulate using MD radiation. Fan Xiong and his colleagues undertook a simulation of the microstructural evolution of an amorphous-nanocrystalline alloy (ANA) under neutron irradiation [37]. They discovered that defects fully recover following cooling and structural relaxation, meaning ANA materials are highly resistant to neutron irradiation. In addition, they found that the nanocrystal-amorphous boundary is driven by localized melting of the melted local region, which can become nanocrystal during cooling, indicating a self-healing behaviour associated with the nanocrystal grain.

2.4 Defect Absorption and its Sink Strength by Nano Crystal Grain Boundary:

Radiation damage has long been reported to be mitigated by nanocrystalline materials with high grain boundaries. Yet, a complete mechanistic understanding of defect reduction has not been developed, especially the interaction between grain boundaries and clustered defects during irradiation.

2.4.1 Defect Absorption:

In irradiated materials, GBs are defined as the mitigated damages, the effects of which become noticeable when the average grain size forms near the mean free paths of the SIAs and Vs during the cascade events. It is possible to examine the effects of GB structure and character in MD simulations, which are difficult to investigate using irradiation experiments.

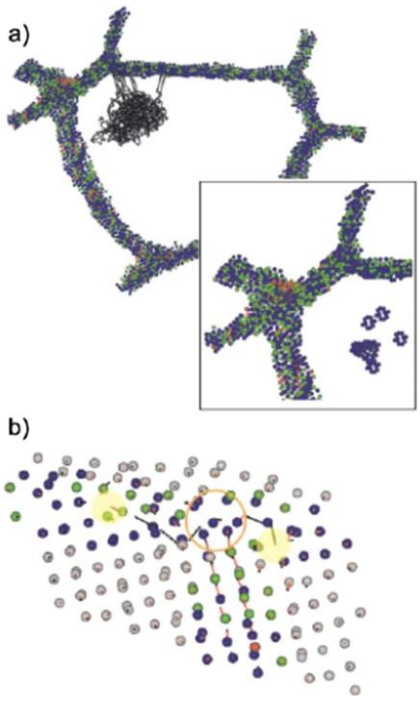

Figure 2. 2 (a) Selected area of the 12-nm NC grain size sample showing the grain boundary (GB) atoms and the displacement vectors (.1.5 Å) between the particles due to a 5 keV PKA. The inset shows a magnified view of the defect region after cooling down. (b) An example of the GB acting as an interstitial sink, by the annihilation of (RCS) interstitials with free volume in the GB (marked in yellow)[38].

GB structure at the nanoscale regime strongly affects the state of primary damage, according to M. Samaras. et al., Figure 2.2. GB often acts as an interstitial sink that allows defect resolidification and a defect structure dominated by the vacancy that can sometimes be removed entirely by nearby GB/TJ (triple junction) regions[38]. Using MD simulations at a resolution of picoseconds, one of the main benefits is determining the physical mechanism. The radiation-induced interstitials and vacancies also prefer to diffuse to the GB region energetically, with the interstitials being more active. Self-healing can explain this, as observed by Liang [39–42] Liu and colleagues.

On top of that, interstitials can quickly diffuse to the GB region and result in eradicating the bulk vacancies [43]. GBs have been shown to play a role in absorption effects in an interstitial emission model from Bai et al. [44]. According to Bai, SIAs move towards GBs much faster than Vs do, altering the formation and migration of other defects in the vicinity of SIAs (Figure 2.3). According to this simulation, point defects with their clusters are predicted to form in or near-pristine boundaries more often than in grain interiors since point defects end up being more easily diffused in an interstitial-loaded grain boundary[44] (Figure 2.4).

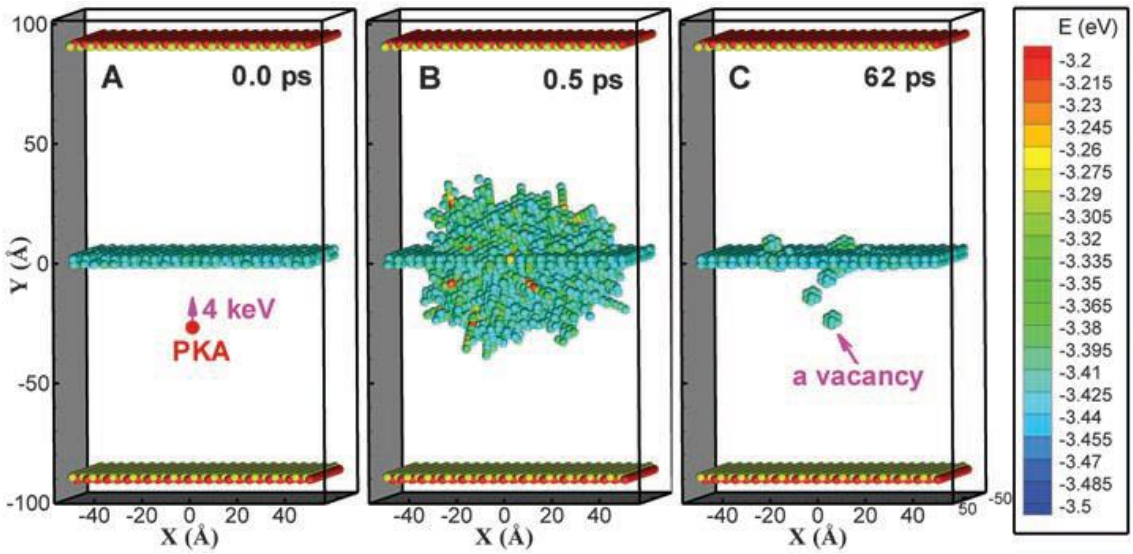

Figure 2. 3 Representative snapshots of a MD simulation of a collision cascade near a S11 symmetric tilt GB at 300 K. The atoms are colored by their potential energy; atoms with energies less than 3.43 eV are treated as non-defective and are not shown. The top and bottom layers are fixed surfaces. (A) Initially, a 4-keV PKA is initiated at 25 Å below the GB with its velocity directed perpendicularly toward the GB. (B) After 0.5 ps, the cascade reaches its maximum size. (C) After 62 ps, the cascade cools down with some vacancies remaining below and above the GB. In this display scheme, a vacancy is characterized as a

12-atom cluster, as indicated in (C), because of the increase in energy of the 12 nearest neighboring atoms of the vacancy[44].

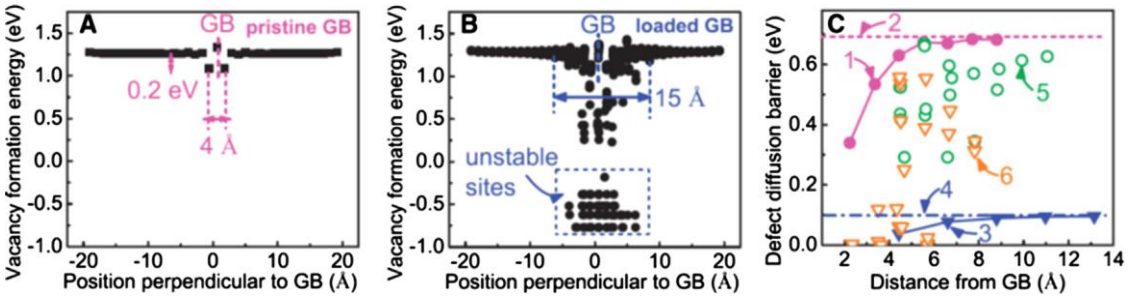

Figure 2. 4 Influence of interstitial loading on defect properties near the symmetric P 11 GB in Cu. (A) Vacancy formation energy profile of a pristine GB. (B) Vacancy formation energy profile of a GB loaded with 10 interstitials, representing the situation occurring after a collision cascade. (C) Defect diffusion barriers as a function of distance from a pristine and an interstitial-loaded GB. Number 1–6 represents vacancy diffusion barriers near the pristine GB, vacancy diffusion barrier in the bulk, interstitial diffusion barriers near the pristine GB, interstitial diffusion barrier in the bulk, vacancy diffusion barriers near the interstitial-loaded GB and interstitial emission barriers near the interstitial-loaded GB, respectively[44].

According to Chen et al.[45], cascade damage is absorbed by the boundary after the boundary structure accounts for the cascade damage. This study has demonstrated that the interactions are always mediated by the formation and annealing of chain-like defects that are interstitials and vacancies alternately positioned. In essence, point defects travel a long distance by travelling through chain-like defects to annihilate one another. For this reason, grain boundaries act as highly effective defect sinks that cannot fill up with debris under high levels of radiation. Also, self-ion irradiated NC Ni can produce damages that have a high vacancy content after cooling down. A complex partial dislocation network forms at higher

energies, and this is called a Truncated stacking fault tetrahedron (TSFT)[46]. The other significant aspect is understanding how GBs and the networks that accompany them move within NC materials due to the radiation damage and temperature rise. After cascade events but before GBs reach their final positions, the MD simulations demonstrate that GBs can move in ps. It was shown by Wolfgang Voegeli [47] and his colleagues that grain growth in response to ion beam irradiation is directly proportional to the amount of recrystallization of the thermal spike volume. Thus, the grain growth in an annealing simulation is fundamentally different from one recorded in a long-term thermal annealing simulation. In such a scenario, the cascade damage would be absorbed, or the thermal spike would result in fast GB migration.

2.5 Sink Strength of Grain Boundaries:

Generally, a grain boundary sink strength should be defined as the average level of defect concentration within a grain. Numerous simulations of the grain size effect have been performed by molecular dynamics [39–42]. Tschopp et al.[48] utilized molecular statistics simulations to analyze sink strength as a function of GB character. Several significant results were found in this study: (1) GB sites generally have a much lower vacancy/interstitial formation energy than bulk sites. There are situations, though, where such sites will preferentially eliminate radiation-induced point defects. (2) While both LAGBs and HAGBs are effective sinks for point defects, HAGBs are more efficient defect sinks because part of the reason for this is their lower point defect formation energy. (3) There is also a decrease in point defect (vacancy and interstitial) formation energies with increasing misorientation angles for LAGBs (less than 15^0) but not for HAGBs. (4) With increasing GB energy, point

defect formation energies decrease. In the boundary, the defect structure appears due to either the initial manufacturing process, mechanical deformation, or radiation damage in the past [49]. It is also predicted that a GB can hold several cascades without a decrease in sink efficiency. It will perform better under radiation than a single crystal of a similar configuration[45]. It is expected that the same structural evolution will not accompany the new cascade events. In contrast to conventional thoughts that GBs in NC metals serve as efficient sinks, there is a different principle than single-crystal tungsten has an advantage over nanocluster tungsten because SIA movement in this system is hindered[50]. In the current study, GBs in NC metals can incorporate defects resulting in multiple sequential cascades resulting in a typical radiation environment. Simulation results by Li et al. have demonstrated the complexity of the annihilation pathways involving trapped interstitials near a GB[51]. The GB contributes to reducing the formation energy and diffusion barriers near vacancies and interstitials. The authors continue to show that the extraordinarily large reduction in the interstitial formation energy alters the annihilation mechanism near the GB. The annihilation occurs through a concerted motion of several atoms with a low barrier, and the interstitial motion lags the vacancy.

2.6 Mechanical Properties:

We still lack a comprehensive understanding of the effect of radiation on NC mechanical properties and the formation and distribution of irradiation-induced defects in NC metals. Irradiation-induced defects induced by GBs are not fully understood from the corresponding atomistic mechanisms. Molecular dynamics (MD) can be applied to observe tools to determine mechanical behaviour's microscopic mechanisms.

2.6.1 Tensile Properties:

A molecular dynamics (MD) simulation can be used to study tensile properties of materials exposed to radiation[52] of nanosized single crystals of Ti-Al alloy nanoparticles with varying compositions using the Embedded Atom Method (EAM). Vacancy concentrations have been estimated for diverse sizes and temperatures of irradiated crystals in the hope that they will provide helpful information about the damage. As the velocity of the PK increases, A.Behera's[52] study shows that the damaging effect of the crystals also increases. The irradiated particle also significantly lost more strength and flexibility than the non-irradiated particle of the same size and composition.

The irradiation effects of nanocrystalline tungsten (W) have been studied by MD simulations[53] which reveal that the ideal tensile strength of monocrystalline and nanocrystalline W decreases and increases with increasing irradiation energy, respectively. Moreover, smaller tungsten nanoparticles possess higher tensile strength under irradiation because of more grain boundaries absorbed with more interstitial atoms. Min Li [54] and his colleague also worked on tungsten by injecting 50 eV to 50 keV tungsten atoms for sputtering. It was found that if the NP was smaller, the atoms sputtered more quickly since the cohesive energy of the atoms changed.

2.6.2 Oxide Dispersion Strengthened (ODS):

In next-generation reactors, more corrosive environments and higher temperatures require more radiation-tolerant structural materials. Materials that are popular for use in this

technology include oxide dispersion strengthened (ODS) steels. Fission reactors have proposed using ODS steel for duct, cladding, and structural purposes, whereas fusion reactors have proposed using ODS steel in the first wall and as a blanket material. In oxide dispersion steels (ODS), nanoclusters (NCs) were investigated for radiation resistance. Analyzing the generation of NC on ODS steels as a result of radiation, molecular dynamics simulations could be used. Y_2O_3 NCs have been shown by M.P.Higgins [55] to improve radiation resistance of ODS steel by diminishing peak defect production during the cascade within the Fe matrix. As a function of PKA energy, NC can also affect collision cascade morphology. In addition to absorbing defects and defect clusters, the NC boundary also modifies the cascade morphology, which leads to significant recombination of interstitials and vacancies away from the NC.

Further, M. Mustafa Azeem [56] has shown that the size of oxide plays a vital role in the depinning mechanism and oxides larger than 2 nm produce new dislocations around themselves. In contrast, more minor oxides allow dislocation bypassing without shearing. With his colleagues, M. Mustafa Azeem[57] showed that ODS displays better stability and recombination properties than regular steel under harsh environments.

2.7 Nanolayers Response on Irradiation:

In numerous nanolayer systems, various interfaces have been studied for their role in mitigating radiation damage. Each interface exhibits a unique efficiency for sinking radiation.

2.7.1 Dislocation:

Two important interface characteristics (i.e., misfit dislocation arrays and miscibility) are highlighted here to uncover their respective influences on interface-defect interactions. 1) Misfit dislocation arrays are defined by a missing or dangling bond in the lattice between two layers with different lattice constants. Radiation produces various vacancies and interstitial clusters. If these clusters migrate to layer interfaces, the interface may modify simultaneously by dissociating in point defects. During the removal or insertion of atoms, M. J. Demkowicz [58] demonstrates how interfaces shift between alternate planes, creating jogs that cover two planes in opposite directions. This extended jog makes CuNb interfaces virtually inexhaustible sinks for radiation-induced point defects and catalysts for efficient Frenkel pair recombination. The MD intersection density, which exhibits a higher density in Figure 2.5 (a–b)[59], can store more He atoms.

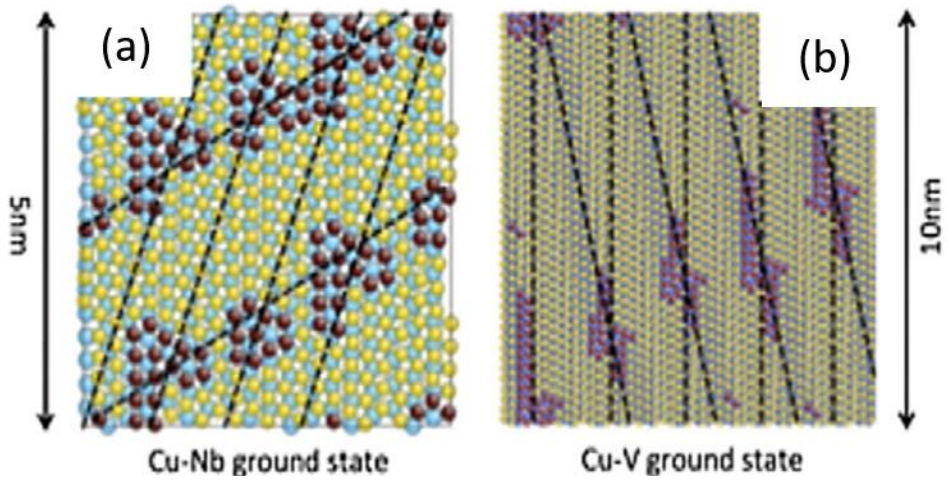

Figure 2. 5 (a) and (b) show the MDIs in Cu/Nb and Cu/V interfaces. The dashed lines indicate interface misfit dislocations[59].

2) Immiscible nanolayer interfaces can hold layer interfaces under irradiation because positive heat of mixing between the layer constituents thermodynamically prompt separate mixing to maintain chemically distinct layer interfaces during irradiation or annealing [60]. The opposite is documented by H.L.Heinisch and his co-worker [61], who demonstrated that nanolayers miscible with water could experience significant interdiffusion.

2.7.2 Dynamic Interactions of Interfaces with Vacancies and Interstitials:

Frenkel pair defects and cluster defects are considered the most direct atomic-level damage sustained by an irradiated material in a collision cascade[62]. These defects are responsible for many of the adverse effects of irradiation on material properties, such as void swelling, hardening, and radiation-induced segregation. After doing simulations on Cu–Nb interfaces, Kedarnath Kolluri et al. revealed that point defect clusters at interfaces are thermodynamically unstable concerning decomposition into isolated defects[63], and this observation has significant aftermath for the stability of these interfaces under irradiation, which leads to defects agglomerates (reduce cluster) and generate voids. The presence of reducing clusters could also lead to increased absorption of supersaturated interfacial point defects under irradiation. It is interesting to note that asymmetric tilt boundaries have similar behaviours concerning defect clustering and may have similar responses to radiation damage [64].

2.8 Radiation Damage Response in Nano-twinned (NT) Metals:

Nano-twinning in materials is identified in grain boundaries as a shifted segment of a crystal. The crystal lattices on each edge are linked across imaginary twin planes by mirror symmetry.

2.8.1 Coherent Twin Boundary (CTB) and Incoherent Twin Boundary (ITB):

Some simulations suggest that coherent twin boundary (CTB) has limited effects on alleviating radiation damage. Using high dose, He implantation near room temperature, Michael J. Demkowicz et al. described the collective impact of a high-volume fraction of Σ3 twin boundaries near the nanoscale. Although he found no evidence that it curtails the formation of vacancies or interstitial clusters[65], others have shown that twin boundaries (TB) can act as effective sinks in real-time. As a result of diffusion channels for radiation-induced defects, NT materials are more radiation-tolerant[66,67]. Recently, MD simulation revealed that CTBs could resist slip transmission. The slip has been shown to interact with the boundary differently depending on the material and strain applied by Z.H.Jin et al. [68]. When external forces force a 60° dislocation into a CTB, it dissociates into multiple partial dislocations that glide into the twin and along its boundary. The material-dependent energy barriers govern the interactions between the dislocations at the location where the distance between the dislocations intersects the boundary. Furthermore, Ting Zhu[69] has shown that slip transfer reaction is mediated by twin boundaries using atomistic reaction pathway calculations. In addition, the mechanism of controlling the plastic flow, the relatively high ductility of nano-twinned copper, and the hardening of twin boundaries are gradually lost to plastic deformation. CTB also interact with lattice dislocations to facilitate the multiplication

of partial dislocations and form imperfect/ defective CTBs [70,71]. A further study by Wang et al.[72] pointed out that as-grown CTBs in NT Cu are inherently defective with kink-like steps and curvatures. The imperfections on CTBs consist of incoherent segments and partial dislocations, which play a crucial role in the deformation mechanisms and defect-TB interactions. Σ {1 1 2} ITBs are of great interest as they are low-energy, thermally stable boundaries that separate one column from the others in NT metals. The structure and stability of Σ3 GBs in FCC metals like Cu with low SFE (Stacking fault energy) and Al with high SFE were examined using atomic simulations [73–77]. Many dislocations are generated during irradiation and frequently interact with the high density of CTBs, possibly due to the above mechanisms. Due to this, large quantities of incoherent twin boundary (ITB) steps are generated. Recent research revealed that CTBs could not absorb acceptable point defects due to their coherent nature[78]. Yet, no simulations have shown dislocation loop TB interactions during radiation. Based on molecular statics simulations, defects in NT Cu preferentially nucleate at ITBs and migrate more rapidly than those in the crystal lattice. Formation energy for an interstitial at ITBs (-1.3 eV) is much lower than that within a crystal lattice (~3 eV) (Figure 2.6), suggesting that interstitials prefer to stay at TBs[67].

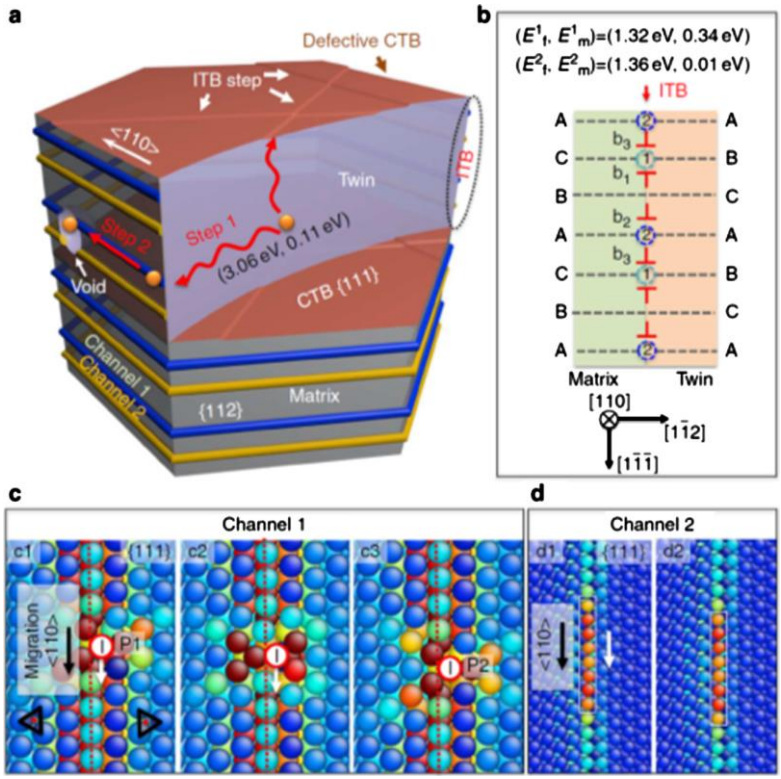

Figure 2. 6 Absorption and diffusion of interstitials in nanovoid-nanotwinned Cu. (a) Fast interstitial diffusion pipes enabled by ITB-CTB networks in NT Cu. (b) Two fast diffusion channels at ITBs and (c, d) the corresponding diffusion mechanisms. (c) For channel 1, an interstitial initially stays at a dislocation core in a {1 1 1} layer sandwiched between b1 and b3. The interstitial then migrates downward to another low-energy site, with energy at the same level as its initial low-energy site. (d) For channel 2, an interstitial has a spreading core associated with the distributed free volume along a dislocation line. The migration of the distributed interstitial requires a shallow energy barrier (0.01 eV) and shows a crowdion-type behaviour [67].

Incoherent twin boundaries (ITB – Incoherent twin boundary) have a plane that is not the same as the plane of the twin plane. The ITB response on radiation can be observed using MD simulations. ITBs can dissociate into two-phase boundaries (PBs), binding the hexagonal 9R phase containing multiple arrays of partial dislocations, Wang et al.[79]

reported. As a result of interface disconnections, ITBs with high stacking energies migrate and slide through interface disconnections, a process known as Interface Disconnection Glide (IDG). Based on MD simulations as shown in Figure 2.7, Niewczas and Hoagland [66] hypothesized that R3 [1 1 1] CTBs could destroy SFTs via interaction with partial dislocations (on CTBs). The explanation for these observations lies in atomistic simulations, which show that the formation energies of vacancies and interstitials at CTBs are nearly identical to those of Cu matrix high-angle GBs in NC metals [80].

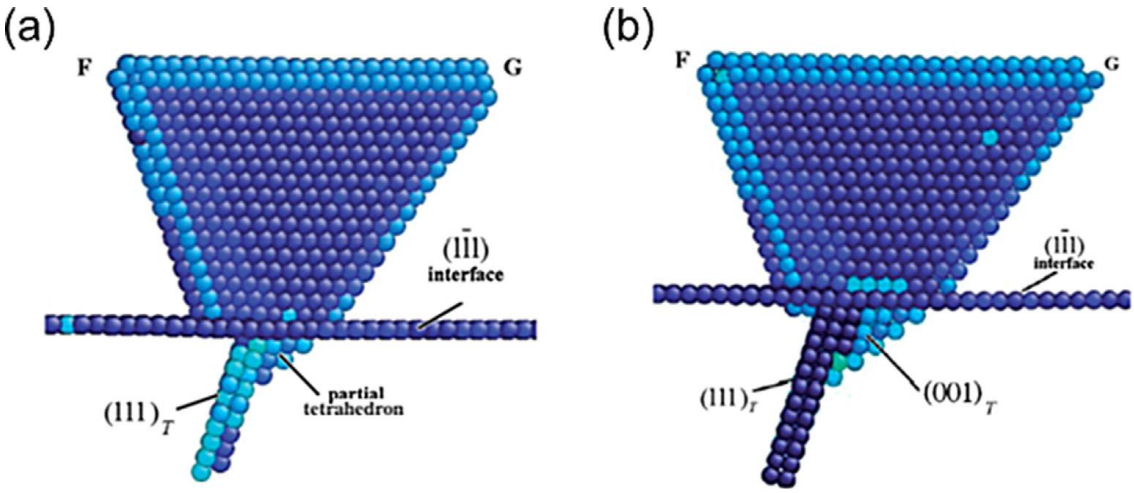

Figure 2. 7 MD simulation results show a growing twin's destruction of a large SFT in apex-down configuration [66]. (a) The parent SFT is partially incorporated into the twin lattice. (b) Destruction of the parent SFT during further twin growth.

2.8.2 Alleviation of Irradiation Damage by Nanovoid-Nanotwinned Architecture

Based on MD simulations, a neighbouring dislocation loop appears to heal the nanovoid (Figure 2.8). With cascade running, partial dislocation loops are nucleated near the Frank loop and spread toward the void, transferring atoms into voids. This lead to loops and voids is shrinking. PKA with higher energy generates a greater cascade so that the void can absorb

more Frank loops[81]. The initial growth along the longitudinal direction is also influenced by the slow nucleation kinetics of vacancies on basal facets and the anisotropic diffusivity of the vacancy layers, as suggested by Weizong Xu et al. [82].

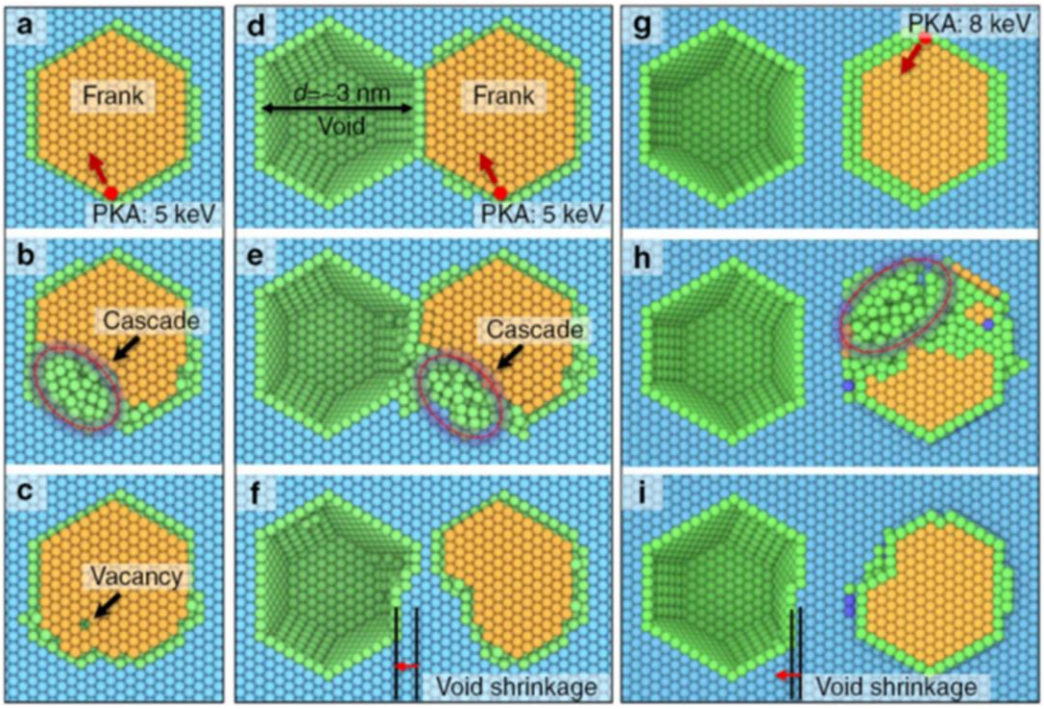

Figure 2. 8 Two-dimensional projected view of an interstitial loop–nanovoid interactions. (a) A 5 keV PKA generates a cascade at one corner of the loop for a stand-alone Frank loop (b). During the quenching process, the cascade shrinks, accompanied by recovery of the Frank loop. After the retreat of the cascade, the Frank loop evolves back to its original configuration, apart from a vacancy at the loop and an interstitial out of the loop (a Frenkel pair) (c). (d) A similar cascade was performed for a Frank loop immediately next to a void (d = 3 nm). (e) Accompanying retreat of the cascade, interstitials are absorbed into the void (f), leading to a shrinkage of the void and substantial removal of the Frank loop. No defects appeared outside the Frank loop. (g) For a Frank loop ~1 nm away from a void (d = 3 nm), a similar cascade generated by an 8 keV PKA was performed (h). The interstitials of the Frank loop were attracted into the void (i), leading to shrinkage of the void and Frank loop. No defects appeared outside the Frank loop in cases (d) and (h)[81].

As shown in Figure 2.9, Zhang et al.[83] found that the vacancy energy increased in Au nanowires from the surface to the bulk region from 0.96 to 1.02 eV. They found that the formation of vacancies becomes increasingly difficult when the distance between the vacancy and the surface is less than 1 nm. On the other hand, Misra et al. [9] demonstrated that defect formation energy varies depending on the material layer. For example, immiscible Cu/Nb multilayers decreased (from ~1.25 to ~0.2 eV in Cu and ~2.75 to ~1.1 eV in Nb) their defect formation energies from the bulk region to the layer interface, respectively, relative to nanowires.

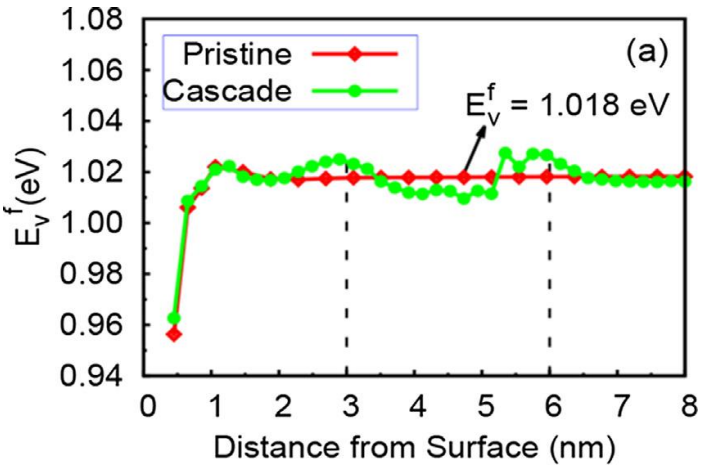

Figure 2. 9 Vacancy formation energy vs vacancy-to-surface distance in Au nanowires [83].

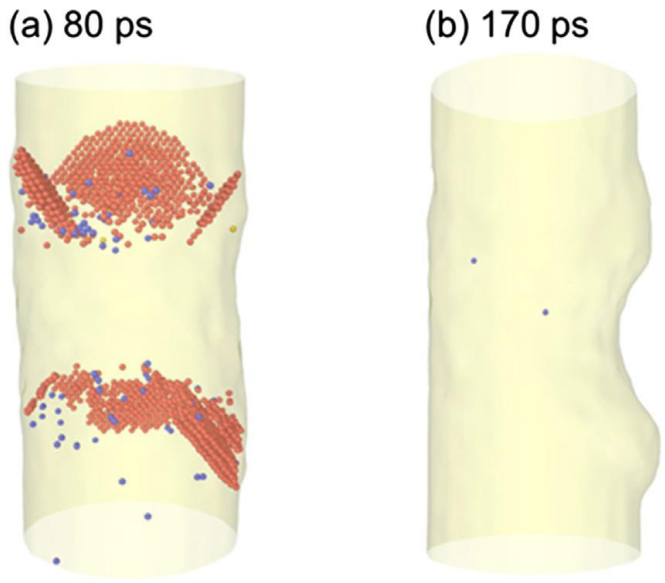

Figure 2. 10 MD simulations illustrate surface roughening in an 8.2 nm-thick Au nanowire after 20 keV self-ion irradiation[84]. (a) Irradiation process at 80 ps, and (b) a crater formed on the surface of the Au nanowire after 170 ps, leading to a rough surface.

The MD simulations can demonstrate a fascinating phenomenon after irradiating Au nanowires with 20 keV self-ions, as shown in Figure 2.10[84]. A gold nanowire had a relatively smooth surface after 80 ps of ion bombardment (Figure 2.10a), but it exhibited a large crater after 170 ps of bombardment. It is hypothesized that the micro explosion of hot atoms could affect the stability of metallic nanowires when the PKA energy is sufficiently high (over 10 keV).

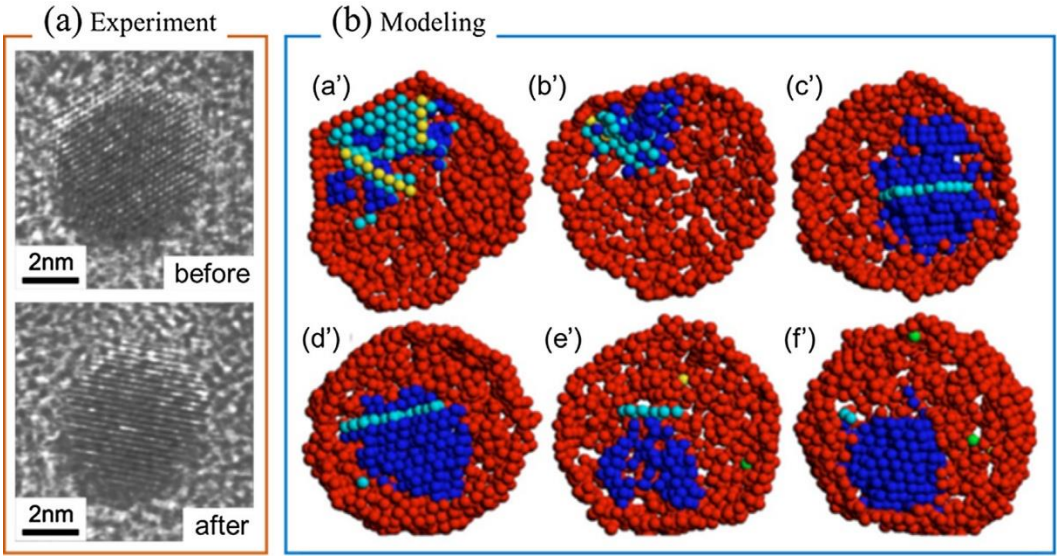

Figure 2. 11 Radiation-induced crystal structure changes of FePt nanoparticles (experiment (a) and modelling (b)). (a) A FePt nanoparticle, which exhibited multiple twinned structure before irradiation (top) transformed into an FCC single crystal particle (bottom) after 5 keV He irradiation at a fluence of $3 * 10^{17}$ ions/cm^2. (b) MD simulation results show the transition from icosahedral to single-crystal morphology in a partly molten cluster. The upper part shows images of the transition. The atoms are FCC (blue), surface (red), HCP (light blue), and fivefold symmetry axis (yellow); liquid atoms are not shown. Initially (a'), the cluster was a partly molten icosahedron. After some point the liquid part almost completely absorbed the solid (b'). The solid then recrystallized with only one TB between two FCC components (c'). The boundary existed for several nanoseconds (d') but migrated in the crystalline part of the cluster. After some time, it reached the liquid boundary (e') and vanished, leaving a single-crystal solid (f')[85].

MD simulations can illustrate how objects change after cascading. Earlier results by Javri et al. demonstrated the transition from icosahedral to single-crystalline morphology can be achieved from just one cascade event. According to their findings, the nanoparticle melted and resolidified as it transitioned, as illustrated in Figure 2.11b. It is possible to observe energy barriers for pure metals and multiphase metal composites through atomistic

simulation models. Near interfaces, defect migration is observed to be lower than in bulk. In addition, defects near an interface often exhibit less barrier diffusion into the interface [44,48,86]. There are many incoherent GBs that contain sites with zero or negative vacancy formation energies. These boundaries are all expected to behave like perfect sinks. Similar results have been observed at heterophase interfaces [87,88].

2.9 Summary:

To develop the advanced nuclear energy systems, novel nanostructured materials are an essential requirement. It allows designers and fabricators to design and fabricate refined nuclear fuels, capture fission products, provide radiation-resistant materials such as ODS, do corrosion-resistant nanocoating, and develop environmental remediation materials. Research on radiation damage in nanostructured materials has grown into an interdisciplinary field that connects nanostructured materials, radiation effects, physics, mechanics, modelling, and simulation. This review focuses primarily on direct damage; however, we also give a brief overview of the physics and simulation tools that can address the changes brought about by the primary event. The reviews demonstrate the significant progress made toward determining the radiation effects of nanostructured materials. Despite that, there are still a lot of unanswered scientific questions. Many defect sinks transform as they interact with radiation-induced defects, and these defect sinks could become incapable of continuously absorbing or eliminating radiation-induced defect clusters. Interfaces' ability to absorb point defects depends on how they are crystallographically arranged and what kind of defect is being absorbed. Interface sink efficiency differs depending on the competition between defect annihilation and trapping at interfaces. The damaged structure of the interface, radiation, temperature, and the damage process itself, determine all these factors.

Researchers cover several types of nanostructure material for observing the radiation effect using computational methods. Having said that radiation effect mechanism on core-shell nanoparticles is still unknown. Qiang and his group[89] found that core-shell NP can sense the radiation using its resistivity. They have used Si ion irradiation and found super-exponential decay with the dose. However, the research for radiation effects on nanomaterials and nanotechnologies in the field of nuclear energy has just started. Further research and mechanism are still a critical need to avoid various scientific hindrances in the NNT. As computer capabilities continue to improve, new algorithms are developed, and artificial intelligence is developed, computational modelling will predict radiation effects from first principles at a broad time and length scale.

2.10 Reference:

[1] D.G. Vaishnav, Chapter - INTRODUCTION TO NANOMATERIALS, (2016).

[2] Y. Qiang, J. Antony, A. Sharma, J. Nutting, D. Sikes, D. Meyer, Iron/iron oxide core-shell nanoclusters for biomedical applications, J. Nanoparticle Res. 8 (2006) 489–496. https://doi.org/10.1007/s11051-005-9011-3.

[3] X.Y. Zhang, L.D. Zhang, G.H. Li, L.X. Zhao, Template sysnthesis of well-graphitized carbon nanotube arrays, Mater. Sci. Eng. A. 308 (2001) 9–12. https://doi.org/10.1016/S0921-5093(00)02036-0.

[4] Y. Tamaura, M. Tahata, Complete reduction of carbon dioxide to carbon using cation-excess magnetite, Nature. 346 (1990) 255–256. https://doi.org/10.1038/346255a0.

[5] J.T. Nurmi, P.G. Tratnyek, V. Sarathy, D.R. Baer, J.E. Amonette, K. Pecher, C. Wang, J.C. Linehan, D.W. Matson, R.L. Penn, M.D. Driessen, Characterization and properties of metallic iron nanoparticles: Spectroscopy, electrochemistry, and kinetics, Environ. Sci. Technol. 39 (2005) 1221–1230. https://doi.org/10.1021/es049190u.

[6] C.B. Wang, W.X. Zhang, Synthesizing nanoscale iron particles for rapid and complete dechlorination of TCE and PCBs, Environ. Sci. Technol. 31 (1997) 2154–2156. https://doi.org/10.1021/es970039c.

[7] R.A. Andrievski, A. V Khatchoyan, Springer Series in Materials Science 230 Nanomaterials in Extreme Environments Fundamentals and Applications, n.d. http://www.springer.com/series/856.

[8] M.J. Demkowicz, P. Bellon, B.D. Wirth, Atomic-scale design of radiation-tolerant nanocomposites, 35 (2010) 992–998.

[9] a Misra, M.J. Demkowicz, X. Zhang, R.G. Hoagland, of Ultra-High Strength Nanolayered Composites STABILITY UNDER ION, Jom. 59 (2007) 3–6.

[10] W.F. van Gunsteren, X. Daura, N. Hansen, A.E. Mark, C. Oostenbrink, S. Riniker, L.J. Smith, Validation of Molecular Simulation: An Overview of Issues, Angew. Chemie - Int. Ed. 57 (2018) 884–902. https://doi.org/10.1002/anie.201702945.

[11] W. Windl, T.J. Lenosky, J.D. Kress, A.F. Voter, First-principles investigation of radiation induced defects in Si and SiC, Nucl. Instruments Methods Phys. Res. Sect. B Beam Interact. with Mater. Atoms. 141 (1998) 61–65. https://doi.org/10.1016/S0168-583X(98)00082-2.

[12] B.J. Cowen, M.S. El-Genk, Probability-based threshold displacement energies for oxygen and silicon atoms in α-quartz silica, Comput. Mater. Sci. 117 (2016) 164–171. https://doi.org/10.1016/j.commatsci.2015.12.041.

[13] M. Robinson, N.A. Marks, K.R. Whittle, G.R. Lumpkin, Systematic calculation of threshold displacement energies: Case study in rutile, Phys. Rev. B - Condens. Matter Mater. Phys. 85 (2012) 1–11. https://doi.org/10.1103/PhysRevB.85.104105.

[14] M. Robinson, N.A. Marks, G.R. Lumpkin, Structural dependence of threshold displacement energies in rutile, anatase and brookite TiO2, Mater. Chem. Phys. 147 (2014) 311–318. https://doi.org/10.1016/j.matchemphys.2014.05.006.

[15] X.M. Bai, B.P. Uberuaga, Multi-timescale investigation of radiation damage near TiO 2 rutile grain boundaries, 2012. https://doi.org/10.1080/14786435.2011.648229.

[16] K. Nordlund, J. Wallenius, L. Malerba, Molecular dynamics simulations of threshold displacement energies in Fe, Nucl. Instruments Methods Phys. Res. Sect. B Beam Interact. with Mater. Atoms. 246 (2006) 322–332. https://doi.org/10.1016/j.nimb.2006.01.003.

[17] K. Trachenko, E. Zarkadoula, I.T. Todorov, M.T. Dove, D.J. Dunstan, K. Nordlund, Modeling high-energy radiation damage in nuclear and fusion applications, Nucl. Instruments Methods Phys. Res. Sect. B Beam Interact. with Mater. Atoms. 277 (2012) 6–13. https://doi.org/10.1016/j.nimb.2011.12.058.

[18] K. Trachenko, M.T. Dove, E. Artacho, I.T. Todorov, W. Smith, Atomistic simulations of resistance to amorphization by radiation damage, Phys. Rev. B - Condens. Matter Mater. Phys. 73 (2006) 1–15. https://doi.org/10.1103/PhysRevB.73.174207.

[19] B.J. Cowen, M.S. El-Genk, K. Hattar, S.A. Briggs, A study of irradiation effects in TiO2 using molecular dynamics simulation and complementary in situ transmission electron microscopy, J. Appl. Phys. 124 (2018). https://doi.org/10.1063/1.5045491.

[20] L.A. Zepeda-Ruiz, S. Han, D.J. Srolovitz, R. Car, B.D. Wirth, Molecular dynamics study of the threshold displacement energy in vanadium, Phys. Rev. B - Condens. Matter Mater. Phys. 67 (2003) 1–5. https://doi.org/10.1103/PhysRevB.67.134114.

[21] H.Y. Xiao, F. Gao, X.T. Zu, W.J. Weber, Threshold displacement energy in GaN: Ab initio molecular dynamics study, J. Appl. Phys. 105 (2009). https://doi.org/10.1063/1.3153277.

[22] M. Robinson, N.A. Marks, G.R. Lumpkin, Sensitivity of the threshold displacement energy to temperature and time, Phys. Rev. B - Condens. Matter Mater. Phys. 86 (2012) 1–8. https://doi.org/10.1103/PhysRevB.86.134105.

[23] G.R. Odette, M.J. Alinger, B.D. Wirth, Recent developments in irradiation-resistant steels, Annu. Rev. Mater. Res. 38 (2008) 471–503. https://doi.org/10.1146/annurev.matsci.38.060407.130315.

[24] E. Zarkadoula, S.L. Daraszewicz, D.M. Duffy, M.A. Seaton, I.T. Todorov, K. Nordlund, M.T. Dove, K. Trachenko, The nature of high-energy radiation damage in iron, J. Phys. Condens. Matter. 25 (2013). https://doi.org/10.1088/0953-8984/25/12/125402.

[25] R.E. Voskoboinikov, Y.N. Osetsky, D.J. Bacon, Computer simulation of primary damage creation in displacement cascades in copper. I. Defect creation and cluster statistics, J. Nucl. Mater. 377 (2008) 385–395. https://doi.org/10.1016/j.jnucmat.2008.01.030.

[26] D.J. Bacon, F. Gao, Y.N. Osetsky, Primary damage state in fcc, bcc and hcp metals as seen in molecular dynamics simulations, J. Nucl. Mater. 276 (2000) 1–12. https://doi.org/10.1016/S0022-3115(99)00165-8.

[27] J. Marian, B.D. Wirth, J.M. Perlado, Mechanism of Formation and Growth of [Formula presented] Interstitial Loops in Ferritic Materials, Phys. Rev. Lett. 88 (2002) 4. https://doi.org/10.1103/PhysRevLett.88.255507.

[28] M.Z.H. Khan, L. Khanal, Y. Qiang, Radiation effect on BCC Fe nanoparticle with varying radiation energy by molecular dynamics simulation, Materialia. 14 (2020) 100930. https://doi.org/10.1016/j.mtla.2020.100930.

[29] H. Xu, R.E. Stoller, Y.N. Osetsky, D. Terentyev, Solving the puzzle of 100 Interstitial Loop Formation in bcc Iron, Phys. Rev. Lett. 110 (2013) 1–5. https://doi.org/10.1103/PhysRevLett.110.265503.

[30] B.D. Wirth, V. Bulatov, T. Diaz De La Rubia, Atomistic simulation of stacking fault tetrahedra formation in Cu, J. Nucl. Mater. 283–287 (2000) 773–777. https://doi.org/10.1016/S0022-3115(00)00262-2.

[31] B.P. Uberuaga, R.G. Hoagland, A.F. Voter, S.M. Valone, Direct transformation of vacancy voids to stacking fault tetrahedra, Phys. Rev. Lett. 99 (2007) 1–4. https://doi.org/10.1103/PhysRevLett.99.135501.

[32] D.J. Bacon, A review of computer models of point defects in hcp metals, J. Nucl. Mater. 159 (1988) 176–189. https://doi.org/10.1016/0022-3115(88)90092-X.

[33] D.J. Bacon, Point defects and clusters in the hcp metals: their role in the dose transition, J. Nucl. Mater. 206 (1993) 249–265. https://doi.org/10.1016/0022-3115(93)90127-K.

[34] L.W. Hobbs, F.W. Clinard, S.J. Zinkle, R.C. Ewing, Radiation effects in ceramics, J. Nucl. Mater. 216 (1994) 291–321. https://doi.org/10.1016/0022-3115(94)90017-5.

[35] T.D. Shen, S. Feng, M. Tang, J.A. Valdez, Y. Wang, K.E. Sickafus, Enhanced radiation tolerance in nanocrystalline Mg Ga2 O4, Appl. Phys. Lett. 90 (2007) 2–5. https://doi.org/10.1063/1.2753098.

[36] D.S. Aidhy, Y. Zhang, W.J. Weber, A fast grain-growth mechanism revealed in nanocrystalline ceramic oxides, Scr. Mater. 83 (2014) 9–12. https://doi.org/10.1016/j.scriptamat.2014.03.020.

[37] F. Xiong, M.F. Li, B. Malomo, L. Yang, Microstructural evolution in amorphous-nanocrystalline ZrCu alloy under neutron irradiation, Acta Mater. 182 (2020) 18–28. https://doi.org/10.1016/j.actamat.2019.10.026.

[38] M. Samaras, P.M. Derlet, H. Van Swygenhoven, M. Victoria, Computer Simulation of Displacement Cascades in Nanocrystalline Ni, Phys. Rev. Lett. 88 (2002) 4. https://doi.org/10.1103/PhysRevLett.88.125505.

[39] I. Adlakha, K.N. Solanki, Atomic-scale investigation of triple junction role on defects binding energetics and structural stability in α-Fe, Acta Mater. 118 (2016) 64–76. https://doi.org/10.1016/j.actamat.2016.07.026.

[40] G. Valles, M. Panizo-Laiz, C. González, I. Martin-Bragado, R. González-Arrabal, N. Gordillo, R. Iglesias, C.L. Guerrero, J.M. Perlado, A. Rivera, Influence of grain boundaries on the radiation-induced defects and hydrogen in nanostructured and coarse-grained tungsten, Acta Mater. 122 (2017) 277–286. https://doi.org/10.1016/j.actamat.2016.10.007.

[41] Z. Chen, L.J. Kecskes, K. Zhu, Q. Wei, Atomistic simulations of the effect of embedded hydrogen and helium on the tensile properties of monocrystalline and nanocrystalline tungsten, J. Nucl. Mater. 481 (2016) 190–200. https://doi.org/10.1016/j.jnucmat.2016.09.024.

[42] M. Samaras, P.M. Derlet, H. Van Swygenhoven, M. Victoria, Atomic scale modelling of the primary damage state of irradiated fcc and bcc nanocrystalline metals, J. Nucl. Mater. 351 (2006) 47–55. https://doi.org/10.1016/j.jnucmat.2006.02.030.

[43] L. Liu, Z. Tang, W. Xiao, Z. Wang, Self-healing mechanism of irradiation defects near Σ = 11 (113) grain boundary in copper, Mater. Lett. 109 (2013) 221–224. https://doi.org/10.1016/j.matlet.2013.07.088.

[44] X.M. Bai, A.F. Voter, R.G. Hoagland, M. Nastasi, B.P. Uberuaga, Efficient annealing of radiation damage near grain boundaries via interstitial emission, Science (80-.). 327 (2010) 1631–1634. https://doi.org/10.1126/science.1183723.

[45] D. Chen, J. Wang, T. Chen, L. Shao, Defect annihilation at grain boundaries in alpha-Fe, Sci. Rep. 3 (2013) 1–5. https://doi.org/10.1038/srep01450.

[46] M. Samaras, P.M. Derlet, H. Van Swygenhoven, M. Victoria, Stacking fault tetrahedra formation in the neighbourhood of grain boundaries, Nucl. Instruments Methods Phys. Res. Sect. B Beam Interact. with Mater. Atoms. 202 (2003) 51–55. https://doi.org/10.1016/S0168-583X(02)01829-3.

[47] W. Voegeli, K. Albe, H. Hahn, Simulation of grain growth in nanocrystalline nickel induced by ion irradiation, Nucl. Instruments Methods Phys. Res. Sect. B Beam Interact. with Mater. Atoms. 202 (2003) 230–235. https://doi.org/10.1016/S0168-583X(02)01862-1.

[48] M.A. Tschopp, K.N. Solanki, F. Gao, X. Sun, M.A. Khaleel, M.F. Horstemeyer, Probing grain boundary sink strength at the nanoscale: Energetics and length scales of vacancy and interstitial absorption by grain boundaries in α-Fe, Phys. Rev. B - Condens. Matter Mater. Phys. 85 (2012) 1–21. https://doi.org/10.1103/PhysRevB.85.064108.

[49] A. Arjhangmehr, S.A.H. Feghhi, Irradiation deformation near different atomic grain boundaries in α-Zr: An investigation of thermodynamics and kinetics of point defects, Sci. Rep. 6 (2016) 1–14. https://doi.org/10.1038/srep23333.

[50] N.Y. Park, P.R. Cha, Y.C. Kim, H.K. Seok, S.H. Han, S.C. Lee, S. Cho, H. Jung, Radiation damage in nano-crystalline tungsten: A molecular dynamics simulation, Met. Mater. Int. 15 (2009) 447–452. https://doi.org/10.1007/s12540-009-0447-3.

[51] X. Li, W. Liu, Y. Xu, C.S. Liu, Q.F. Fang, B.C. Pan, J.L. Chen, G.N. Luo, Z. Wang, An energetic and kinetic perspective of the grain-boundary role in healing radiation damage in tungsten, Nucl. Fusion. 53 (2013). https://doi.org/10.1088/0029-5515/53/12/123014.

[52] A. Behera, M.M. Ghosh, Effect of Irradiation on the Tensile Properties of Nano-sized Ti-Al Alloy Single Crystals: A Study Using Molecular Dynamics Simulations, Mater. Today Proc. 5 (2018) 20647–20651. https://doi.org/10.1016/j.matpr.2018.06.447.

[53] L. Chen, L.Q. Li, H.R. Gong, J.L. Fan, W. Li, Irradiation effect on mechanical properties of tungsten from molecular dynamic simulation, Mater. Lett. 241 (2019) 27–30. https://doi.org/10.1016/j.matlet.2019.01.043.

[54] M. Li, Q. Hou, J. Cui, B. Fu, Molecular dynamics simulations of tungsten bombardments on tungsten nanoparticles, Nucl. Instruments Methods Phys. Res. Sect. B Beam Interact. with Mater. Atoms. 450 (2019) 47–50. https://doi.org/10.1016/j.nimb.2018.04.028.

[55] M.P. Higgins, Q. Peng, L. Shao, F. Gao, Reduction of defect generation and development of sinks at nanocluster boundary in oxide dispersion-strengthened steel, J. Appl. Phys. 126 (2019). https://doi.org/10.1063/1.5102090.

[56] M.M. Azeem, Q. Wang, Z. Li, Y. Zhang, Dislocation-oxide interaction in Y2O3 embedded Fe: A molecular dynamics simulation study, Nucl. Eng. Technol. 52 (2020) 337–343. https://doi.org/10.1016/j.net.2019.07.011.

[57] M.M. Azeem, Z. Li, Q. Wang, Q.M.N. Amjad, M. Zubair, O.M.H. Ahmed, Classical molecular dynamics study for defect sink behavior in oxide dispersed strengthened alloys, Proc. 2018 15th Int. Bhurban Conf. Appl. Sci. Technol. IBCAST 2018. 2018-Janua (2018) 12–15. https://doi.org/10.1109/IBCAST.2018.8312177.

[58] M.J. Demkowicz, R.G. Hoagland, J.P. Hirth, Interface structure and radiation damage resistance in Cu-Nb multilayer nanocomposites, Phys. Rev. Lett. 100 (2008) 2–5. https://doi.org/10.1103/PhysRevLett.100.136102.

[59] M.J. Demkowicz, D. Bhattacharyya, I. Usov, Y.Q. Wang, M. Nastasi, A. Misra, The effect of excess atomic volume on He bubble formation at fcc-bcc interfaces, Appl. Phys. Lett. 97 (2010) 1–4. https://doi.org/10.1063/1.3502594.

[60] X. Zhang, K. Hattar, Y. Chen, L. Shao, J. Li, C. Sun, K. Yu, N. Li, M.L. Taheri, H. Wang, J. Wang, M. Nastasi, Radiation damage in nanostructured materials, Prog. Mater. Sci. 96 (2018) 217–321. https://doi.org/10.1016/j.pmatsci.2018.03.002.

[61] H.L. Heinisch, F. Gao, R.J. Kurtz, The effects of interfaces on radiation damage production in layered metal composites, J. Nucl. Mater. 329–333 (2004) 924–928. https://doi.org/10.1016/j.jnucmat.2004.04.142.

[62] D.J. Bacon, Y.N. Osetsky, Modelling atomic scale radiation damage processes and effects in metals, Int. Mater. Rev. 47 (2002) 233–242. https://doi.org/10.1179/095066002225006575.

[63] K. Kolluri, M.J. Demkowicz, Formation, migration, and clustering of delocalized vacancies and interstitials at a solid-state semicoherent interface, Phys. Rev. B - Condens. Matter Mater. Phys. 85 (2012) 1–15. https://doi.org/10.1103/PhysRevB.85.205416.

[64] B.P. Uberuaga, L.J. Vernon, E. Martinez, A.F. Voter, The relationship between grain boundary structure, defect mobility, and grain boundary sink efficiency, Sci. Rep. 5 (2015) 1–9. https://doi.org/10.1038/srep09095.

[65] M.J. Demkowicz, O. Anderoglu, X. Zhang, A. Misra, The influence of a’3 twin boundaries on the formation of radiation-induced defect clusters in nanotwinned Cu, J. Mater. Res. 26 (2011) 1666–1675. https://doi.org/10.1557/jmr.2011.56.

[66] M. Niewczas, R.G. Hoagland, Molecular dynamic studies of the interaction of a/6112 Shockley dislocations with stacking fault tetrahedra in copper. Part II: Intersection of stacking fault tetrahedra by moving twin boundaries, Philos. Mag. 89 (2009) 727–746. https://doi.org/10.1080/14786430902740703.

[67] Y. Chen, K.Y. Yu, Y. Liu, S. Shao, H. Wang, M.A. Kirk, J. Wang, X. Zhang, Damage-tolerant nanotwinned metals with nanovoids under radiation environments, Nat. Commun. 6 (2015). https://doi.org/10.1038/ncomms8036.

[68] Z.H. Jin, P. Gumbsch, K. Albe, E. Ma, K. Lu, H. Gleiter, H. Hahn, Interactions between non-screw lattice dislocations and coherent twin boundaries in face-centered cubic metals, Acta Mater. 56 (2008) 1126–1135. https://doi.org/10.1016/j.actamat.2007.11.020.

[69] T. Zhu, J. Li, A. Samanta, H.G. Kim, S. Suresh, Interfacial plasticity governs strain rate sensitivity and ductility in nanostructured metals, Proc. Natl. Acad. Sci. U. S. A. 104 (2007) 3031–3036. https://doi.org/10.1073/pnas.0611097104.

[70] M. Zhernenkov, M.S. Jablin, A. Misra, M. Nastasi, Y. Wang, M.J. Demkowicz, J.K. Baldwin, J. Majewski, Trapping of implanted He at Cu/Nb interfaces measured by neutron reflectometry, Appl. Phys. Lett. 98 (2011) 2009–2012. https://doi.org/10.1063/1.3600642.

[71] J. Wang, O. Anderoglu, J.P. Hirth, A. Misra, X. Zhang, Dislocation structures of σ3 {112} twin boundaries in face centered cubic metals, Appl. Phys. Lett. 95 (2009) 93–96. https://doi.org/10.1063/1.3176979.

[72] J. Li, K.Y. Yu, Y. Chen, M. Song, H. Wang, M.A. Kirk, M. Li, X. Zhang, In situ study of defect migration kinetics and self-healing of twin boundaries in heavy ion irradiated nanotwinned metals, Nano Lett. 15 (2015) 2922–2927. https://doi.org/10.1021/nl504677z.

[73] L. Zhu, H. Ruan, X. Li, M. Dao, H. Gao, J. Lu, Modeling grain size dependent optimal twin spacing for achieving ultimate high strength and related high ductility in nanotwinned metals, Acta Mater. 59 (2011) 5544–5557. https://doi.org/10.1016/j.actamat.2011.05.027.

[74] X. Zhou, X. Li, C. Chen, Atomistic mechanisms of fatigue in nanotwinned metals, Acta Mater. 99 (2015) 77–86. https://doi.org/10.1016/j.actamat.2015.07.045.

[75] Z.X. Wu, Y.W. Zhang, D.J. Srolovitz, Dislocation-twin interaction mechanisms for ultrahigh strength and ductility in nanotwinned metals, Acta Mater. 57 (2009) 4508–4518. https://doi.org/10.1016/j.actamat.2009.06.015.

[76] S. Jiao, Y. Kulkarni, Molecular dynamics study of creep mechanisms in nanotwinned metals, Comput. Mater. Sci. 110 (2015) 254–260. https://doi.org/10.1016/j.commatsci.2015.08.017.

[77] D. Chen, Y. Kulkarni, Elucidating the kinetics of twin boundaries from thermal fluctuations, MRS Commun. 3 (2013) 241–244. https://doi.org/10.1557/mrc.2013.37.

[78] S. Jiao, Y. Kulkarni, Radiation tolerance of nanotwinned metals – An atomistic perspective, Comput. Mater. Sci. 142 (2018) 290–296. https://doi.org/10.1016/j.commatsci.2017.10.023.

[79] J. Wang, A. Misra, J.P. Hirth, Shear response of $\Sigma 3\{112\}$ twin boundaries in face-centered-cubic metals, Phys. Rev. B - Condens. Matter Mater. Phys. 83 (2011) 1–8. https://doi.org/10.1103/PhysRevB.83.064106.

[80] M.R. Sørensen, Y. Mishin, Diffusion mechanisms in Cu grain boundaries, Phys. Rev. B - Condens. Matter Mater. Phys. 62 (2000) 3658–3673. https://doi.org/10.1103/PhysRevB.62.3658.

[81] Y. Chen, X. Zhang, J. Wang, Radiation Enhanced Absorption of Frank Loops by Nanovoids in Cu, Jom. 68 (2016) 235–241. https://doi.org/10.1007/s11837-015-1689-9.

[82] W. Xu, Y. Zhang, G. Cheng, W. Jian, P.C. Millett, C.C. Koch, S.N. Mathaudhu, Y. Zhu, In-situ atomic-scale observation of irradiation-induced void formation, Nat. Commun. 4 (2013). https://doi.org/10.1038/ncomms3288.

[83] C.G. Zhang, Y.G. Li, W.H. Zhou, L. Hu, Z. Zeng, Anti-radiation mechanisms in nanoporous gold studied via molecular dynamics simulations, J. Nucl. Mater. 466 (2015) 328–333. https://doi.org/10.1016/j.jnucmat.2015.08.003.

[84] W. Liu, P. Chen, R. Qiu, M. Khan, J. Liu, M. Hou, J. Duan, A molecular dynamics simulation study of irradiation induced defects in gold nanowire, Nucl. Instruments Methods Phys. Res. Sect. B Beam Interact. with Mater. Atoms. 405 (2017) 22–30. https://doi.org/10.1016/j.nimb.2017.05.016.

[85] T.T. Järvi, A. Kuronen, K. Nordlund, K. Albe, Structural modification of a multiply twinned nanoparticle by ion irradiation: A molecular dynamics study, J. Appl. Phys. 102 (2007). https://doi.org/10.1063/1.2825045.

[86] X.Y. Liu, B.P. Uberuaga, M.J. Demkowicz, T.C. Germann, A. Misra, M. Nastasi, Mechanism for recombination of radiation-induced point defects at interphase boundaries, Phys. Rev. B - Condens. Matter Mater. Phys. 85 (2012) 18–21. https://doi.org/10.1103/PhysRevB.85.012103.

[87] X.Y. Liu, R.G. Hoagland, J. Wang, T.C. Germann, A. Misra, The influence of dilute heats of mixing on the atomic structures, defect energetics and mechanical properties of fcc-bcc interfaces, Acta Mater. 58 (2010) 4549–4557. https://doi.org/10.1016/j.actamat.2010.05.008.

[88] K. Kolluri, M.J. Demkowicz, R.G. Hoagland, X.Y. Liu, Behavior of vacancies and interstitials at semicoherent interfaces, Jom. 65 (2013) 374–381. https://doi.org/10.1007/s11837-012-0540-9.

[89] W. Jiang, J.A. Sundararajan, T. Varga, M.E. Bowden, Y. Qiang, J.S. McCloy, C.H. Henager, R.O. Montgomery, In situ study of nanostructure and electrical resistance of nanocluster films irradiated with ion beams, Adv. Funct. Mater. 24 (2014) 6210–6218. https://doi.org/10.1002/adfm.201400553.

Chapter 3: Computational Methods

This chapter provides a brief introduction to MD methods and describes the features applied during the simulations.

3.1 Molecular Dynamics (MD) Simulations:

The Molecular Dynamics (MD) method predicts the movement of one atom under a force created by other atoms of a typical size of millions. For the trajectory of each particle, we solve Newton's law of motion F = ma. By computing coordinates and velocities based on atoms' trajectories, one can predict the system's state at any time. To provide information about the dynamics of a system at the microscopic level, MD simulations use accurate force fields to describe the interactions between the atoms of the system.

In 1957, Alder and Wainwright[1] first introduced MD methods to describe the hard-sphere interaction. In 1960, Rahman[2] performed MD simulation on argon, and later, Stillnger[3] with his colleagues did the MD simulation in liquid water. R.P. Webb and his colleague[4,5] were the first scientists who have used MD simulation for radiation damage research. After that, in the 1990s, several MD simulations were done on defects and displacements for radiation damage[6–9]. Since then, with the development of computer facilities, MD simulation has explained several experimental and predicted radiation damage[10,11]. Several radiation damage research has been done using MD simulation such as diffusion, grain growth, grain boundaries, and phase transitions[12–16].

The critical part of MD simulation is the force calculation, which depends on potentials. The accuracy of a MD simulation is determined by how accurate the interatomic potentials are.

These potentials must come from more complicated quantum mechanics treatments. In many cases, even the most advanced calculations cannot serve the purposes well, and a combination with experimental data is necessary to reflect the intrinsic properties of the materials. The primary approaches to get interatomic potentials include ab initio method, empirical method, and semi-empirical method. Examples of such potentials for metals are the Finnis-Sinclair potential, Mendelev et al. potential, Ackland et al potential, and Dudarev-Derlet potential, and their modifications in the embedded atom method (EAM) potential was applied. Other examples include the Tersoff potential for silicon, Ferrari et al. potential for phase transitions in potassium tetrachlorozincate, a modification of Fisler potential for a range of carbonate structures, Schelling et al. and Yu et al. potentials for zirconia, and Mendelev and Ackland potential for phase transformations in zirconium[17,18,27–30,19–26].

Several codes use MD techniques, for example, MOLDY, DYMOKA, LIVCAS, MDCASK, LAMMPS, and DLPOLY. The last two show scalable behavior meaning double the number of cores double the efficiency for calculation. Increasing with computing capabilities and the development of interatomic potential, MD code provides better and accurate results. The progress on code scalability, interatomic potential development, and computer capabilities set the stage for high energy radiation damage simulations in large systems, up to 1 billion atoms.

Several works on radiation damage have shown that the damage recovery results from the amorphization for different materials[31]. Based on extensive analysis of experimental data, theory, and ab initio simulations, it was proposed that the type of interaction and the nature of

chemical bonds play a crucial role in this process[31–33]. The results from radiation damage modelling are good fit with experimental34–36 results, implying that MD simulation can predict the radiation damage and explain experimental results.

3.2 Algorithms:

The foundation of the MD simulation is Newton's second law. To integrate Newton's equation, position and the velocity of each atom can be calculated by Taylor's expansion (3.1)

$$r(t+\delta t) = r(t) + v(t) + \frac{1}{2}a(t)\delta t^2 + \cdots \tag{3.1}$$

$$v(t+\delta t) = v(t) + a(t)\delta(t) + \frac{1}{2}b(t)\delta t^2 + \cdots$$

$$a(t+\delta t) = a(t) + b(t)\delta(t) + \cdots$$

where r is the position, v is the velocity, and a is the acceleration. we can rewrite the displacements at small time steps as

$$r(t+\delta t) = r(t) + v(t)\delta t + \frac{1}{2}a(t)\delta t^2 + \cdots \tag{3.2}$$

$$r(t-\delta t) = r(t) + v(t)\delta t + \frac{1}{2}a(t)\delta t^2 + \cdots$$

Summing these two equations, one obtains

$$r(t+\delta t) = 2r(t) - r(t-\delta t) + a(t)\delta t^2 + \cdots \tag{3.3}$$

The above formula uses positions at time t and $t-\delta t$ to calculate new positions at time $t+\delta t$. The advantage of the calculation is that it reduces the errors introduced when a relatively a larger time step is used. In MD simulations, this formula is used as basic integration

algorithms. Figure 3.1 schematically shows the MD simulation procedure. In the beginning, positions and velocities of all atoms are defined, then forces are calculated based on the potential gradients. Then, displacement equations are solved for all atoms in the system over time, and physical quantities of interest are extracted, such as temperature, energy, pressure, etc. If the total computational time satisfies $t < t_{max}$, the program will go back to the stage of calculating forces, so on repeating the steps within the loop, until finally $t = t_{max}$.

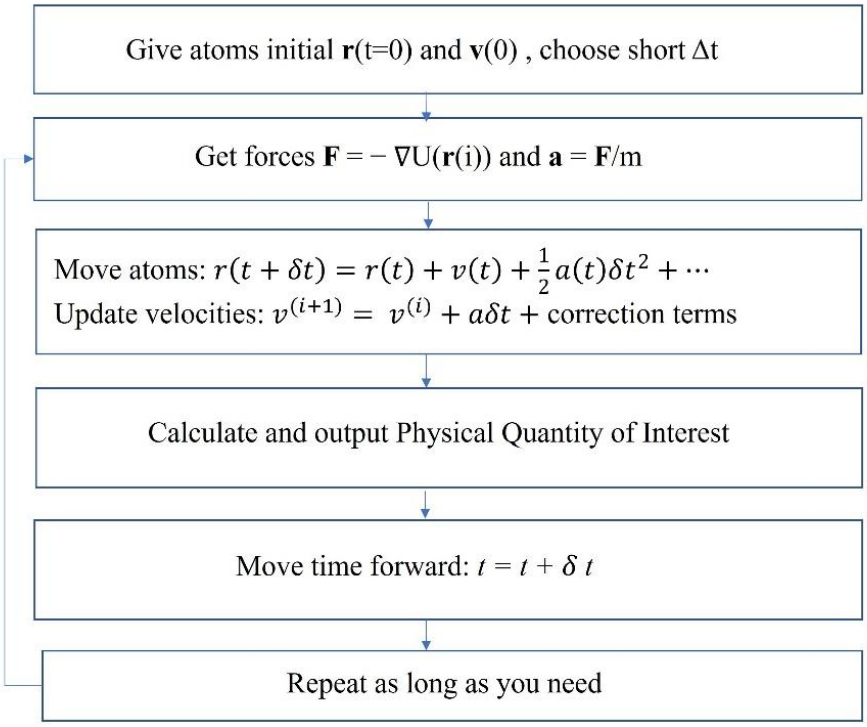

Figure 3. 1 The simulation proceeds of molecular dynamics simulation

3.3 Interatomic potential:

The critical part of MD simulation is the force calculation, which depends on potentials. The efficiency of a MD simulation is determined by how correct the interatomic potentials are. These potentials must come from more complicated quantum mechanics treatment. In many

cases, the advanced calculation cannot serve the purpose well, and a combination with experimental data is needed to reflect the materials' fundamental properties. The primary path to get interatomic potentials includes ab initio method, empirical method, and semi-empirical method.

Ab-initio methods rely on quantum mechanics. The potentials are created from solving a multi-body Schrödinger equation by the quantum mechanical calculation. The benefit of this method is that it starts from the first principles. However, some errors exist due to assumptions and approximations used to simplify the process.

Semi-empirical potentials are also based on quantum mechanics calculation, some items are ignored in the analysis, for example, in Hartree-Fock calculations, and experimental results replace this calculation.

The overlap of specific atomic orbitals is neglected for empirical potentials, and many free parameters are introduced to predict experimental observations.

In a molecular system, the potential is divided into two parts: inter-molecule potential and intra-molecule potential. These two parts can be considered separately.

$$U = U_{\text{intermolecular potential in pairs}} + U_{\text{intramolecular potential}} \quad (4)$$

A triple potential, which considers three-body interactions, can extremely slow down the simulation

$$U\left(\overrightarrow{r_1}, \overrightarrow{\Omega_1}; \overrightarrow{r_2}, \overrightarrow{\Omega_2} \dots \dots \overrightarrow{r_n}, \overrightarrow{\Omega_n}\right) = \sum_{\text{Pair,i,j}} U\left(\overrightarrow{r_1}, \overrightarrow{\Omega_1}; \overrightarrow{r_2}, \overrightarrow{\Omega_2}\right) \quad (5)$$

Intra-molecular potential consists of several parts: bond stretching, angle bending, torsion and improper torsion, as shown in Eq.6:

$$U_{intramolecular} = \sum_{bonds} k_b(r - r_0)^2 + \sum_{angles} k_\theta(\theta - \theta_0)^2 + \sum_{torsion} k_x[1 + \cos(nX_0 - \delta_0)] + \sum_{improper} k_\psi(\psi - \psi_0)^2 \quad (6)$$

where k is a force parameter, r_0 is the equilibrium bond length, θ_0 is the equilibrium angle, δ_0 is the twisting angle and ψ_0 is the equilibrium angle in improper torsion.

With respect to inter-molecular pair potential, the Lennard-Jones potential is the most used potential in spherical models:

$$U_{L,J}(r) = 4\varepsilon[(\frac{\sigma}{r})^{12} - (\frac{\sigma}{r})^{6}] \quad (7)$$

σ is the distance at which the particle-particle potential energy $U_{L,J}$is zero, ε is the depth of the potential well, and r is the distance between two interacting particles.

With respect to the electrostatics potential, partial atomic charges are used in Coulomb charge-charge interaction to the multi-polar potential

$$U_{electrostatics}(r) = \sum_{i>j} \frac{q_i * q_j}{r_{ij}} \quad (8)$$

Adding all the potential energy, the total potential of the molecular system will look like:

$$U = 4\varepsilon\left[\left(\frac{\sigma}{r}\right)^{12} - \left(\frac{\sigma}{r}\right)^{6}\right] + \sum_{i>j} \frac{q_i * q_j}{r_{ij}} + \sum_{bonds} k_b(r - r_0)^2 + \sum_{angles} k_\theta(\theta - \theta_0)^2 + \sum_{torsion} k_x[1 + \cos(nX_0 - \delta_0)] + \sum_{improper} k_\psi(\psi - \psi_0)^2 \quad (9)$$

3.4 Embedded Atom Model (EAM) Potential:

In the case of the metallic model, only the interatomic part is considered. Lennard-Jones (LJ) potential is appropriate in a system with weak bond interactions, e.g., gas. However, it is not suitable for solid bonding systems such as covalent, metallic, or ionic bonds. Furthermore,

metallic bonds are also dependent on the surrounding atoms[37]. For this reason, novel empirical many-body potentials have been developed for metallic bonds. In this potential, (1) the many-body term is introduced in the potential to capture the nature of many-body interactions in the metallic system, and (2) commonly used many-body potentials are Embedded Atom Method (EAM) potential[22] and Finnis-Sinclair (F-S) potential[29]. EAM potential is based on Density Functional Theory (DFT), and F-S model is based on Tight Binding Theory, and these two potentials can share the same[38] form Eq. 10:

$$U = \frac{1}{2}\sum_{i=1}^{N}\sum_{j-1}^{N-1} V(r_{ij}) + \sum_{i-1}^{N} F(\rho_i) \tag{10}$$

$V(r_{ij})$ is pairwise potential, $F(\rho_i)$ is the many bodies part, ρ_i is the electron density, and r_{ij} is the separation of atom i and j. In the F-S model, the $F(\rho_i)$ is in square root form. In the EAM model,

$$\rho_i = \sum_{j\neq i} \phi(r_{ij}) \tag{11}$$

Eq. 11 represents the electron density contribution at the position of atom i from all other atoms j. $F(\rho_i)$ is the corresponding embedding energy from putting one atom i in the electron environment. V is the electrostatic energy. Three parts are needed in EAM potential: two-body pair potential $V(r_{ij})$, electron density function r_{ij} and the embedding energy function F. Eq. (10) and Eq. (11) can combine:

$$U = \frac{1}{2}\sum_{i=1}^{N}\sum_{j-1}^{N-1} V(r_{ij}) + \sum_{i-1}^{N} F(\sum_{j\neq i} \phi(r_{ij})) \tag{12}$$

3.5 COMP Potential:

EAM potentials have been extensively applied in the metallic system during the past thirty years. However, the application of the EAM potential is limited in the metallic system; EAM potentials are incapable of handling a system with a complex bonding environment. To solve this problem, another potential formalism, Charge-optimized many-body (COMB) potential, has been developing in the past ten years[39–41]. The COMB3 formalism is a bond-order type potential with variable charge. The general form for COMB3 is: (1)

$$U_{tot} = U_{ele}(q, r) + U_{short}(q, r) + U_{vdW}(r) + U_{corr}(i, j, k)$$

where the total potential energy U_{tot} is given as the sum of the electrostatic energy $U_{ele}(q, r)$, the short-range energy $U_{short}(q, r)$, the long-range or van der Waals energy $U_{vdW}(r)$ and a correction term $U_{corr}(i, j, k)$. The comb3 potential is constructed by fitting to a large experimental database and comparing with other ab initio data.

The COMB3 potential can describe titanium, Titania, oxygen. The details of the COMB3 formalism and other examples of its applications are described elsewhere [42,43]. The development of potential for such a wide range of materials inevitably requires some compromises regarding the fidelity of any specific system. In particular, COMB3 successfully reproduces the relative stability of these phases of Ti, with the α(hcp) phases predicted to be the ground state phase. In addition, rutile is correctly expected to be more stable than the other standard, high pressure, or hypothetical AB_2 phases. The potential reproduces many of the properties of the three low Miller index rutile surfaces [(1 1 0), (0 0 1), and (1 0 0)]. This potential has been successfully used in the previous investigation of Ti and TiO_2 for various purposes. Therefore, it is good to examine metal clusters on TiO_2,

which are important heterogeneous catalysts [43–46]. They have developed metallic Ti and TiO_2 within the framework of the third generation COMB (COMB3) potential.

3.6 LAMMPS:

LAMMPS is a classical molecular dynamics code with a focus on materials modeling. It's an acronym for Large-scale Atomic/Molecular Massively Parallel Simulator. To use LAMMPS to run MD simulations, only three key pieces are needed. These essential pieces are an input script, an atom file, and a potential file.

The input script is a text file formatted in a way to instruct the LAMMPS program. This file gives LAMMPS such information as what units to use, coordinates/velocities of atoms, types of atoms, as well as what to do to the atoms such as heating the atoms, minimizing energy, and so on, and then finally how long the simulation will last given in terms of time steps. The typical structure of a LAMMPS script is as follows:

Initialization tells LAMMPS what units to use, what type of atom potential is used, and how to parse the use of the processors for parallelization.

Atom Definition can be done in one of three ways. i) Specific LAMMPS commands are from the input script to make and load atoms into memory, read atom positions and velocities from a specially formatted text file. ii) For any atomic arrangement other than the most basic structures, atoms are typically not created using the input script. Reading a specifically formatted text file containing the information about the atoms' position allows flexibility generated by other software. iii) Reading restart files are valuable if the script is continuing a simulation that was previously run. LAMMPS restart files are binary files that contain all the information about a previous simulation.

Settings allow the user to adjust several parameters in simulation such as temperature, pressure, labeling, and tracking certain groups of atoms, specify the output format, or constrain the system in many other ways. This is essentially where the user tells LAMMPS what actions to take.

Run: This command tells LAMMPS to start evaluating forces on each atom and integrate a specified number of steps over time. Steps three and four in the overall process may be repeated until the desired result is obtained.

Atom Files: Atom files are the text files that specify the location of the atoms. The first two lines of the atom file are comment lines meant to clarify what the file contains. The following three lines give the dimension of the simulation box or terms of the unit offered in the input script. Lines six and seven tell LAMMPS how many atoms and types of atoms are included in the simulation. The following lines are the heading followed by the list of atoms. Atoms are specified by their ID, type, and three-dimensional location.

Potential file: A potential file is necessary to read the atom-atom interaction. There are more than 50 styles of pair potentials that can be read into LAMMPS. However, each of these styles must be formatted correctly.

Features

Some features have been used for doing simulations that will be discussed in the below sections, including a brief description of the condition.

Units –tells LAMMPS what units to use: e.g., the keyword metal specifies the distance in angstroms, time in picoseconds, pressure in atmospheres, and so on

Atom_style – determines what type of information is associated with each atom

Boundary – specifies what kind of boundary to implement on each face of the simulation

box; this can have values of periodic (if an atom goes outside the boundary, it shows up on the opposite side; see Figure 3.2), fixed (atoms are lost if theygo past the boundary), or shrink-wrapped (non-periodic, but atoms are not lost if they go outside the boundary)

Periodic Boundary Conditions- If surface properties are not concerned in the simulation, periodic boundary conditions are typically implemented to diminish the property's calculation's surface effect. For example, in a 1000 atoms system, around half of the atoms are on the outer faces. Under the periodic boundary conditions, when one atom moves out of the simulation cubic, it will re-enter the cubic from the opposite side. In the cascade simulation, atomic collisions and thermal spike can cross the system boundary if the computational cell is quite small; thus, the cascade may interact. If the cross-boundary happens, the heat should be extracted by damping the boundary atoms or replacing the system with a sufficiently larger cubie[47,48]. In our modeling of radiation damage effects, we are interested in the nanosystem. We use fixed periodic boundary conditions (PBC) to replicate the nanoparticle, which imitates the initial MD cell in all directions. PBC enables the calculations to be performed from a small number of particles, increasing the calculation efficiency.

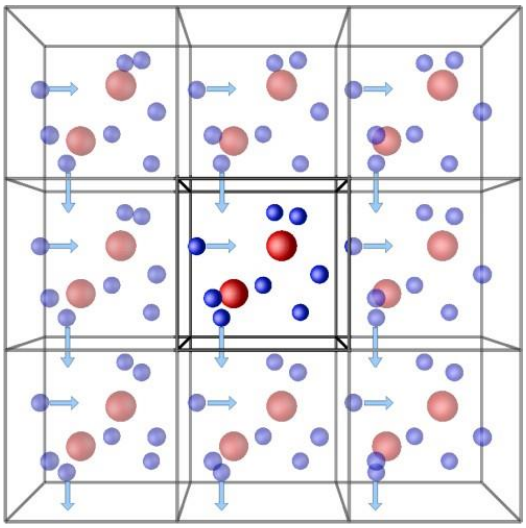

Figure 3. 2 Representation of periodic boundary conditions.

Newton – specifies Newton's 3rd law (two atoms exert equal and opposite forces on one another) when evaluating forces; turning this on gives aslight boost in performance in most circumstances

Read_data or read_restart – these commands read the atomic data from a textfile or a binary restart file, respectively

Pair_style – tells what type of potential is being used

Pair_coeff – this loads the potential file into memory and specifies what kind of atoms are used in the potential file

Velocity – gives the atoms some initial velocity based on a Gaussian distribution ofspeed as determined by the temperature

Fix – this command has a variety of purposes: for instance, this command can tell LAMMPS to raise the temperature from 300K to 600K

Unfix – removes the specified fix command

Thermo and thermo_modify – means LAMMPS to print thermodynamic informationand

modifies how or what is printed

Timestep – specifies how much simulation time to integrate over

Compute – tells LAMMPS to calculate specific quantities at every time step

Dump – in addition to a standard log file, LAMMPS can create custom output filesusing this command

run – simulate a specified number of time steps

minimize – adjusts the coordinates of each atom in such a way as to reduce thetotal energy of the system (also known as quenching)

NVE - The microcanonical ensemble represents a constant number of particles N, constant volume V, and constant energy E. The NVE ensemble was applied to all the system atoms, except for in the boundary layer for the cascade simulations where the electronic effect mechanisms are not implemented.

NPT - The isothermal-isobaric NPT ensemble in which the system is coupled to a Berendsen thermostat, an external bath with constant temperature and pressure[49]. The thermosetting and barostatting are achieved by adding dynamic variables coupled to the particle velocities (thermostatting) and simulation domain dimensions (barostatting). In addition to basic thermostatting and barostatting, these fixes can also create a chain of thermostats coupled to the particle thermostat and another chain of thermostats coupled to the barostat variables.

System equilibration - Core-shell systems are equilibrated in the NPT ensemble coupled to a Berendsen thermostat for 20 ps, with a constant timestep of 0.001 ps. The system's temperature is rescaled after each step during equilibration. We then allow the system to relax for 2-3ps using the same timestep until the atoms settle in their equilibrium positions.

Variable timestep - We have used variable timestep for the simulations of the collision

cascades, which accounts for the different dynamics of the system during the cascade evolution. The variable timestep is the practical approach because at the beginning of the simulation, the atomic motion is fast due to the atoms' high energy, and then a tiny timestep is needed. When the development of the cascade slows down, an enormous value of timestep is required. The initial timestep can be 0.005 fs, reaching the order of 0.01 fs as the system relaxes.

Boundary Thermostat - In our core-shell simulations, a layer of the MD box is coupled to a constant temperature to replicate the effect of energy dissipation into the sample. In this case, the velocity of the atoms is contained and scaled after each time step which is necessary for the highly non-equilibrium process to replicate heat transfer by phonons.

3.7 Displaced and Defect Atoms:

The Wigner-Seitz (W-S)[50] method is applied in this work, and the advantage of this method is to be convenient for identifying defects (vacancies and interstitial atoms). A W-S cell is constructed around every atom in the simulations; these cells consist of all points closer to a given atom than any other atom. They have the property that is guaranteed to contain exactly one atom. This network of W-S cells is then superimposed on the simulation output that contains defects, and the number of atoms in each cell is counted. A cell containing zero atoms is counted as a vacancy, while two atoms are counted as an interstitial. Cells that have precisely one atom are treated as being defect-free. The detailed procedure is outlined in Figure 3.3 (a) The atom lattice position in the stable equilibrium structure after relaxation before irradiation. (b) W-S cells are superimposed on equilibrium structure and count no defects because each cell contains a single atom. (c) displaced atoms after radiation and (d)

W-S cells are superimposed on the displaced structure and counted. It has been found some cells contain more than one atom that considers as an interstitial, no atom as a vacancy, and a single atom believes to a defect-free.

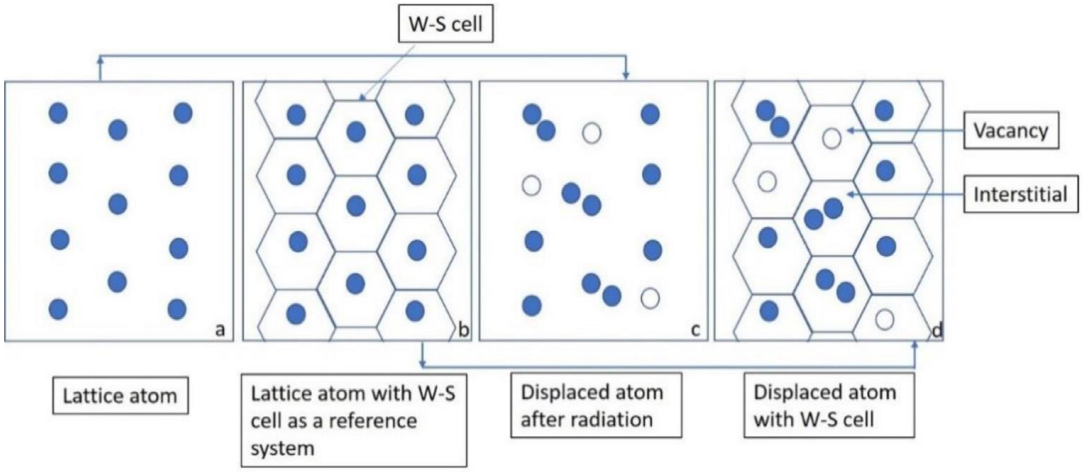

Figure 3. 3 Weigner-Seitz (W-S) method for counting point defects: (a) equilibrium lattice atom, (b) reference system with W-S cell, (c) displace atoms (d) displace atoms with W-S cell.

3.8 Reference:

1. Alder, B. J. & Wainwright, T. E. Phase transition for a hard sphere system. *J. Chem. Phys.* **27**, 1208–1209 (1957).
2. Rossky, P. J. Perspective on 'correlations in the motion of atoms in liquid argon'. *Theor. Chem. Acc.* **103**, 263–264 (2000).
3. Stillinger, F. H. & Rahman, A. Improved simulation of liquid water by molecular dynamics. *J. Chem. Phys.* **60**, 1528–1532 (1974).
4. Webb, R. P. ~ I P~ End. 698–702 (1800).
5. Webb, R. P. & Harrison, D. E. Computer simulation of pit formation in metals by ion bombardment. *Phys. Rev. Lett.* **50**, 1478–1481 (1983).
6. Diaz De La Rubia, T. & Guinan, M. W. New mechanism of defect production in metals: A molecular-dynamics study of interstitial-dislocation-loop formation in high-energy displacement cascades. *Phys. Rev. Lett.* **66**, 2766–2769 (1991).
7. Computational, A. of defects a. **48**, 22–30 (1993).
8. Phythian, W. J., English, C. A., Yellen, D. H. & Bacon, D. J. Collapse of displacement cascades in h.c.p. metals. *Philos. Mag. A Phys. Condens. Matter, Struct. Defects Mech. Prop.* **63**, 821–833 (1991).
9. Zhu, H., Averback, R. S. & Nastasi, M. Molecular dynamics simulations of a 10keV cascade in β-NiAl. *Philos. Mag. A Phys. Condens. Matter, Struct. Defects Mech. Prop.* **71**, 735–758 (1995).
10. High-performance computing in the chemistry and physics of materials. *Proc. R. Soc. A Math. Phys. Eng. Sci.* **467**, 1880–1884 (2011).

11. Catlow, R. *et al.* Computer modelling of inorganic materials. *Annu. Reports Prog. Chem. - Sect. A* **101**, 513–547 (2005).

12. Keblinsk, P., Wolf, D., Phillpot, S. R. & Gleiter, H. Self-diffusion in high-angle fcc metal grain boundaries by molecular dynamics simulation. *Philos. Mag. A Phys. Condens. Matter, Struct. Defects Mech. Prop.* **79**, 2735–2761 (1999).

13. Sastre, G., Catlow, C. R. A. & Corma, A. Diffusion of benzene and propylene in MCM-22 zeolite. A molecular dynamics study. *J. Phys. Chem. B* **103**, 5187–5196 (1999).

14. Schelling, P. K. & Phillpot, S. R. Mechanism of Thermal Transport in Zirconia and Yttria-Stabilized Zirconia by Molecular-Dynamics Simulation. *J. Am. Ceram. Soc.* **84**, 2997–3007 (2001).

15. Haslam, A. J., Phillpot, S. R., Wolf, D., Moldovan, D. & Gleiter, H. Mechanisms of grain growth in nanocrystalline fcc metals by molecular-dynamics simulation. *Mater. Sci. Eng. A* **318**, 293–312 (2001).

16. Fuchs, A. H. & Pawley, G. S. Molecular dynamics simulation of the plastic to triclinic phase transition in clusters of SF6. *J. Phys.* **49**, 41–51 (1988).

17. Yu, J., Devanathan, R. & Weber, W. J. Unified interatomic potential for zircon, zirconia and silica systems. *J. Mater. Chem.* **19**, 3923–3930 (2009).

18. Cygan, R. T., Wright, K., Fisler, D. K., Gale, J. D. & Slater, B. Atomistic models of carbonate minerals: Bulk and surface structures, defects, and diffusion. *Mol. Simul.* **28**, 475–495 (2002).

19. Archer, T. D. *et al.* An interatomic potential model for carbonates allowing for polarization effects. *Phys. Chem. Miner.* **30**, 416–424 (2003).

20. Ferrari, E. S., Roberts, K. J., Thomson, G. B., Gale, J. D. & Catlow, C. R. A. Interatomic potential parameters for potassium tetrachlorozincate and their application to modelling its phase transformations. *Acta Crystallogr. Sect. A Found. Crystallogr.* **57**, 264–271 (2001).

21. Dynamics, M. & Propagation, C. ン き 裂伝 ぱ の 解 析.

22. Foiles, S. M., Baskes, M. I. & Daw, M. S. Embedded-atom-method functions for the fcc metals Cu, Ag, Au, Ni, Pd, Pt, and their alloys. *Phys. Rev. B* **33**, 7983–7991 (1986).

23. Malerba, L. *et al.* Comparison of empirical interatomic potentials for iron applied to radiation damage studies. *J. Nucl. Mater.* **406**, 19–38 (2010).

24. Bacon, D. J. & Diaz de la Rubia, T. Molecular dynamics computer simulations of displacement cascades in metals. *J. Nucl. Mater.* **216**, 275–290 (1994).

25. Souidi, A. *et al.* Dependence of radiation damage accumulation in iron on underlying models of displacement cascades and subsequent defect migration. *J. Nucl. Mater.* **355**, 89–103 (2006).

26. Dudarev, S. L. & Derlet, P. M. A 'magnetic' interatomic potential for molecular dynamics simulations. *J. Phys. Condens. Matter* **17**, 7097–7118 (2005).

27. Ackland, G. J., Bacon, D. J., Calder, A. F. & Harry, T. Computer simulation of point defect properties in dilute fe-cu alloy using a many-body interatomic potential. *Philos. Mag. A Phys. Condens. Matter, Struct. Defects Mech. Prop.* **75**, 713–732 (1997).

28. Mendelev, M. I. *et al.* Development of new interatomic potentials appropriate for crystalline and liquid iron. *Philos. Mag.* **83**, 3977–3994 (2003).

29. Finnis, M. W. & Sinclair, J. E. A simple empirical N-body potential for transition metals. *Philos. Mag. A Phys. Condens. Matter, Struct. Defects Mech. Prop.* **50**, 45–55 (1984).

30. Bacon, D. J., Osetsky, Y. N., Stoller, R. & Voskoboinikov, R. E. MD description of damage production in displacement cascades in copper and α-iron. *J. Nucl. Mater.* **323**, 152–162 (2003).

31. Trachenko, K. Understanding resistance to amorphization by radiation damage. *J. Phys. Condens. Matter* **16**, (2004).

32. Trachenko, K., Pruneda, J. M., Artacho, E. & Dove, M. T. How the nature of the chemical bond governs resistance to amorphization by radiation damage. *Phys. Rev. B - Condens. Matter Mater. Phys.* **71**, 1–5 (2005).

33. Trachenko, K., Pruneda, M., Artacho, E. & Dove, M. T. Radiation damage effects in the perovskite CaTiO3 and resistance of materials to amorphization. *Phys. Rev. B - Condens. Matter Mater. Phys.* **70**, 1–6 (2004).

34. Li, F., Ishimaru, M., Lu, P., Afanasyev-Charkin, I. V. & Sickafus, K. E. Damage evolution in Xe-ion irradiated rutile (TiO2) single crystals. *Nucl. Instruments Methods Phys. Res. Sect. B Beam Interact. with Mater. Atoms* **166**, 314–321 (2000).

35. Wang, S. X., Wang, L. M. & Ewing, R. C. Ion irradiation-induced amorphization of two GeO2 polymorphs. *Nucl. Instruments Methods Phys. Res. Sect. B Beam Interact. with Mater. Atoms* **175**–**177**, 615–619 (2001).

36. Wang, S. X., Wang, L. M., Ewing, R. C. & Doremus, R. H. Ion beam-induced amorphization in MgO-Al2O3-SiO2. I. Experimental and theoretical basis. *J. Non. Cryst. Solids* **238**, 198–213 (1998).

37. Adams, J. B. *et al.* Atomic-level computer simulation. *J. Nucl. Mater.* **216**, 265–274 (1994).

38. Daw, Murray, S., Foiles, Stephen, M. & Baskes, Michael, I. The embedded-atom method : a review of theory and applications. *Mater. Sci. Reports* **9**, 251–310 (1993).

39. Noordhoek, M. J., Liang, T., Chiang, T. W., Sinnott, S. B. & Phillpot, S. R. Mechanisms of Zr surface corrosion determined via molecular dynamics simulations with charge-optimized many-body (COMB) potentials. *J. Nucl. Mater.* **452**, 285–295 (2014).

40. Noordhoek, M. J. *et al.* Charge-optimized many-body (COMB) potential for zirconium. *J. Nucl. Mater.* **441**, 274–279 (2013).

41. Choudhary, K., Liang, T., Chernatynskiy, A., Phillpot, S. R. & Sinnott, S. B. Charge optimized many-body (COMB) potential for Al2O3 materials, interfaces, and nanostructures. *J. Phys. Condens. Matter* **27**, (2015).

42. Phillpot, S. R. *et al.* Charge Optimized Many Body (COMB) potentials for simulation of nuclear fuel and clad. *Comput. Mater. Sci.* **148**, 231–241 (2018).

43. Rodríguez, J. A. *et al.* High water-gas shift activity in TiO 2(110) supported Cu and Au nanoparticles: role of the oxide and metal particle size. *J. Phys. Chem. C* **113**, 7364–7370 (2009).

44. Panagiotopoulou, P., Kondarides, D. I. & Verykios, X. E. Mechanistic study of the selective methanation of CO over Ru/TiO 2 catalyst: Identification of active surface species and reaction pathways. *J. Phys. Chem. C* **115**, 1220–1230 (2011).

45. Lira, E. *et al.* Growth of Ag and Au nanoparticles on reduced and oxidized rutile TiO 2(110) surfaces. *Top. Catal.* **56**, 1460–1476 (2013).

46. Galhenage, R. P. *et al.* Understanding the nucleation and growth of metals on TiO2: Co compared to Au, Ni, and Pt. *J. Phys. Chem. C* **117**, 7191–7201 (2013).

47. Calder, A. F. & Bacon, D. J. A molecular dynamics study of displacement cascades in α-iron. *J. Nucl. Mater.* **207**, 25–45 (1993).

48. Bacon, D. J., Calder, A. F. & Gao, F. Defect production due to displacement cascades in metals as revealed by computer simulation. *J. Nucl. Mater.* **251**, 1–12 (1997).

49. Berendsen, H. J. C., Postma, J. P. M., Van Gunsteren, W. F., Dinola, A. & Haak, J. R. Molecular dynamics with coupling to an external bath. *J. Chem. Phys.* **81**, 3684–3690 (1984).

50. Zou, P. F. & Bader, R. F. W. A topological definition of a Wigner–Seitz cell and the atomic scattering factor. *Acta Crystallogr. Sect. A* **50**, 714–725 (1994).

Chapter 4: Radiation Effect on BCC Fe Nanoparticle with Varying Radiation Energy by Molecular Dynamics Simulation

Mohammad Zahidul Hossain Khan, Lokendra Khanal, and You Qiang*

Department of Physics, University of Idaho, Moscow, ID-83844, USA

*: Email: youqiang@uidaho.edu

4.1 Abstract:

Molecular dynamics simulations were conducted to explore primary radiation damages on body-centered cubic (BCC) Fe nanoparticle. A series of 6 cascades for each primary knock-on atom (PKA) energy (5 keV, 10 keV, 20 keV, 30 keV and 40 keV) was simulated to assure statistical precision. It has been observed that defects created due to the interactions have stayed as single to several size clusters. Most of the clusters are either single interstitials (SIAs) or vacancies (Vs). In each of the energy cases, it produces one block of a big cluster. The block cluster of SIAs stays at the near surface of the nanoparticle; however, Vs stay inside the nanoparticle. The study has shown that the total number of vacancy defects is larger than the total number of interstitial defects because more PKA energy gives more mobility that some SIAs can get enough energy to leave the Fe nanoparticle.

4.2 Introduction:

Nanomaterials are materials where at least one dimension is less than 100 nanometers. In this nanoscale, unique optical, magnetic, electrical and other properties emerge, which show the potential for great impacts in applications of electronics, medicine, radiation protection and other fields[1]. Over the past few years, iron-based magnetic nanoparticles have been discovered for potential applications in various areas, including drug delivery, enhanced

magnetic resonance imaging, information storage, reduction of carbon dioxide, and groundwater remediation[2–6]. Recently, nuclear scientists have found their interest in magnetic nanoparticles (NPs) to be used as a nuclear radiation sensing material to be utilized in upcoming generation IV nuclear reactors for safe and secure production of nuclear energy[7].

It was previously reported that Fe-Fe_3O_4 core-shell NPs with Fe_3O_4 as the shell and body-centred cubic (BCC) Fe as the core have very sensitive electrical conductivity and magnetic properties under Si^{2+} ion irradiation, even at shallow dose ion flux regime with the minimal effect of the temperature up to 200 °C[8]. Also, studies have shown that the average size of the Fe in the Fe-Fe_2O_3/Fe_3O_4 core-shell structure decreases[9], and Fe core reduces its Fe valence[10] under irradiation.

Core-shell nanoparticles are highly functional nanomaterials with modified properties. These properties can be changed by changing the core to shell ratio[11]. Scientists confirmed for core-shell Fe-Fe_2O_3/Fe_3O_4 NPs, iron core is BCC structure. There is an interface between core and shell, which can act as a defect sink[12]. It is necessary to know how defect reaches from core to surface or interface and how they distribute during the irradiation. This information will help to explain the reason for the size change of Fe-Fe_2O_3/Fe_3O_4 core-shell structure in the presence of radiation.

Moreover, BCC Fe with other material NPs is currently of interest for high radiation dose applications, specifically where the dose is more significant than 20 displacements per atom (dpa)[13,14]. These high radiation dose conditions induce significant microstructure changes, including defect clustering, dislocation loop formation, void, and bubble formation[13]. Thus, it is essential to understand the behavior of the Fe NP alone under irradiation to investigate further the scientific reason for forming defect clusters or void formation. It will also help

describe the scientific reasoning behind the structure of the change in Fe-core behavior in the core-shell NP. By far, it has been no report of this type of research that has been conducted to understand the irradiation behavior of the BCC Fe NP.

For the intended purpose, Our simulation work will be in two steps. In 1st step, we performed a molecular dynamics (MD) simulation on the BCC Fe NPs. We investigated defect production, defect orientation, and cluster (as an aggregate) formation and distribution with varying the radiation energy from 5 keV to 40 keV, which is for this journal. In 2nd step, core-shell Fe- Fe_2O_3/Fe_3O_4 will be used for MD simulation to observe the radiation effect.

4.3 Methodology

MD simulations were carried out using a Large-scale Atomic/Molecular Massively Parallel Simulator (LAMMPS)[15] to study the effects of primary irradiation damage in Fe NPs. The available visual tool (OVITO)[16] was utilized to analyze microstructural evolutions during the cascade collision. The model Fe NP was spherical with a diameter ~14.5 nm. The previous work[17,18] has shown that the average size of the BCC Fe nanoparticles is in the range of 15 nm in diameter. The x, y and z directions correspond to the [1 0 0], [0 1 0] and [0 0 1] crystal axes of the BCC-Fe, respectively. Mendelev et al.[19] had developed an embedded atom model (EAM) potential, which could properly predict the Fe-Fe interaction in radiation damage studies. This paper also describes the cohesive energy (-4.3 eV) and defect (interstitial (4.1 eV) and vacancy (1.8 eV)) formation energy. Three-dimensional boundary conditions have been used as fixed[20,21,22] to represent only isolate Fe nanoparticle. The simulation was run with boundary regions at 300 K for 22 ps. To prepare the Fe NP for collision cascade simulations, the outermost layer of the simulation box with 10 Å thickness was equilibrated using a Berendsen thermostat at 300 K for 22 ps that acted as a heat source. The remaining

innermost atoms could evolve dynamically using the microcanonical (No. of atoms, volume and energy are constant) ensemble. For the simulations of the collision cascades, adaptive timestep was used, which was accounted for the different dynamics of the system during the cascade evolution. We considered maximum distance for an atom to move in one timestep is 0.05 Å and maximum new timestep 0.001 ps between two integrations and the simulations were stable. A random atom was selected as a primary knock-on atom (PKA) and provided the initial energy (neutron recoil energy is converted to the PKA energy and this PKA energy is converted into a velocity to apply on the PKA) and the incident direction as random direction.

Post simulation, a new position of each lattice atom was obtained, and the new structure was compared with the reference structure before radiation. The Wigner-Seitz (W-S)[23] method is applied in this work, and the advantage of this method is to be convenient for identifying defects (vacancies and interstitial atoms).

A W-S cell is constructed around every atom in the simulations; these cells consist of all points closer to a given atom than any other atom. They have the property that is guaranteed to contain exactly one atom. This network of W-S cells is then superimposed on the simulation output that contains defects, and the number of atoms in each cell is counted. A cell containing zero atoms is counted as a vacancy, while two atoms are counted as an interstitial. Cells that have precisely one atom are treated as being defect-free.

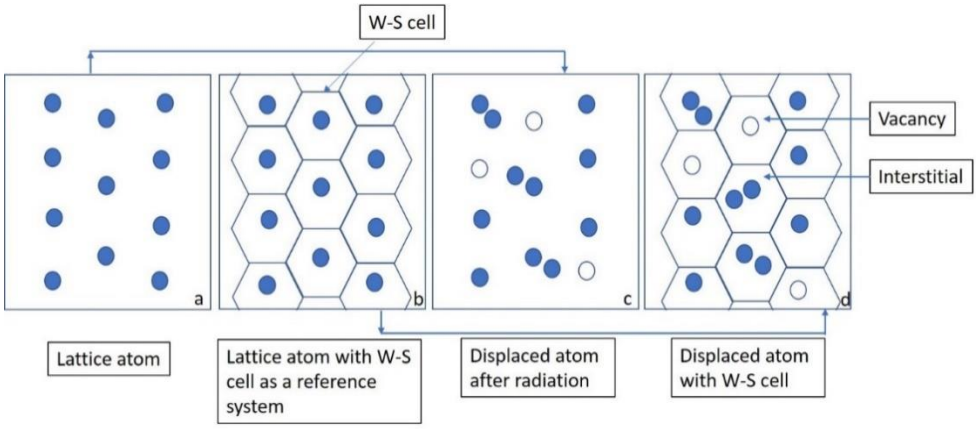

Figure 4. 1 Weigner-Seitz (W-S) method for counting point defects: (a) equilibrium lattice atom, (b) reference system with W-S cell, (c) displace atoms (d) displace atoms with W-S cell

The detailed procedure is outlined in Fig. 4.1. (a) the atom lattice position in the stable equilibrium structure after relaxation before irradiation. (b) W-S cells are superimposed on equilibrium structure and count no defects because each cell contains a single atom. (c) displaced atoms after radiation, and (d) W-S cells are superimposed on the displaced structure and counted. Some cells contain more than one atom that considers interstitial, no atom has a vacancy, and a single atom is considered defect-free.

4.4 Result and Discussion

4.4.1 Evolution of Primary Damage

Prior irradiation produces point defects in the Fe NP, containing self-interstitials (SIAs) and vacancies (Vs). Figure 4.2 has shown the dynamic evolution of defects (SIAs) (Figure 2a) and Vs. (Figure 2b). The defect evolution can be described in 4 stages: (i) Collision, (ii) Thermal spike, (iii) Quench or recombination, and (iv) Anneal or stabilization. In the (i) collisional stage, the primary recoil atom initiates a cascade for developing collision, and it continues till the atom contains enough energy to create further displacement. This stage lasts

around 1ps that as shown in Figure 4.2. During this time, defects include SIAs and Vs., though stable defects do not form yet. In the (ii) thermal spike stage, the energetic SIAs atoms share their energy with neighbor atoms and generate a high energy density deposited region. This region also resembles the molten or liquid material[24]and Fe NP temperature increase average 986K and 813K for 40keV and 30keV. After that, neighbor atoms share energy with their neighbors, and energy is transferred to the surrounding atoms, and the molten region becomes condensed. The (iii) stage is called the quenching stage. The quenching stage in Figure 4.2 takes around 10 ps. In this stage, SIAs and Vs are reunited in maximum quantities, and the rest form some stable defects as a single defect or a cluster of defects. In (iv) the annealing stage (11 ps to 22 ps), further rearrangement occurs by thermally activated diffusion of mobile defects[24], and the numbers of SIAs and Vs remain almost the same.

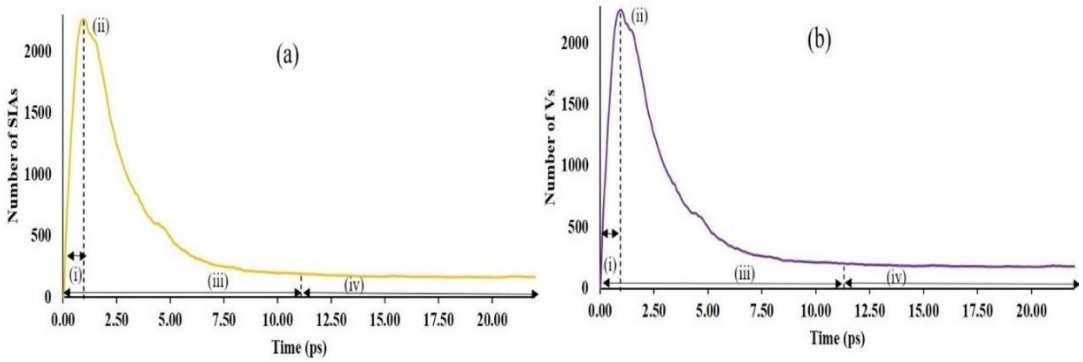

Figure 4. 2 The dynamic evolution of (a) SIAs (yellow) and (b) Vs (purple) under 40 keV of PKA directed in a random direction. The stages of (i), (ii), (iii), and (iv) are the collisional, thermal spike, quenching, and annealing stages, respectively.

4.4.2 Peak Time Features

A plot of the SIAs evolution of different PKA energy as a function of time during the cascade collision is shown in Figure 4.3(a). For characterizing the damage peak, the time interval

between cascade initiation and the moment, when the number of generated atomic point defects reached its maximum (i.e., peak time). The damage peak time as a function of PKA energy has been shown in Figure 4.3(b), including error bars in the figures denote the standard error of the average dataset for each case. It follows the power law

$$T_{PKA} = 0.1E_{PKA}^{0.7} \quad (1)$$

where T_{PKA} and E_{PKA} are the time for maximum defect and PKA energy, respectively. It illustrates that the damage peak takes more time with increasing PKA energy. The larger PKA energy reaches the more neighbor atoms to distribute the energy, which takes more time than smaller PKA energy. It is also seen that the slope of the curve decreases with increasing the PKA energy. The reason is that sub-cascades form by splitting atomic displacement cascades triggered by secondary knock-on atoms (SKAs) with energy lower than the PKA energy. These sub-cascades generated by SKAs have shorter peak times than the main cascade, decreasing the peak time linearly with increasing PKA energy[25].

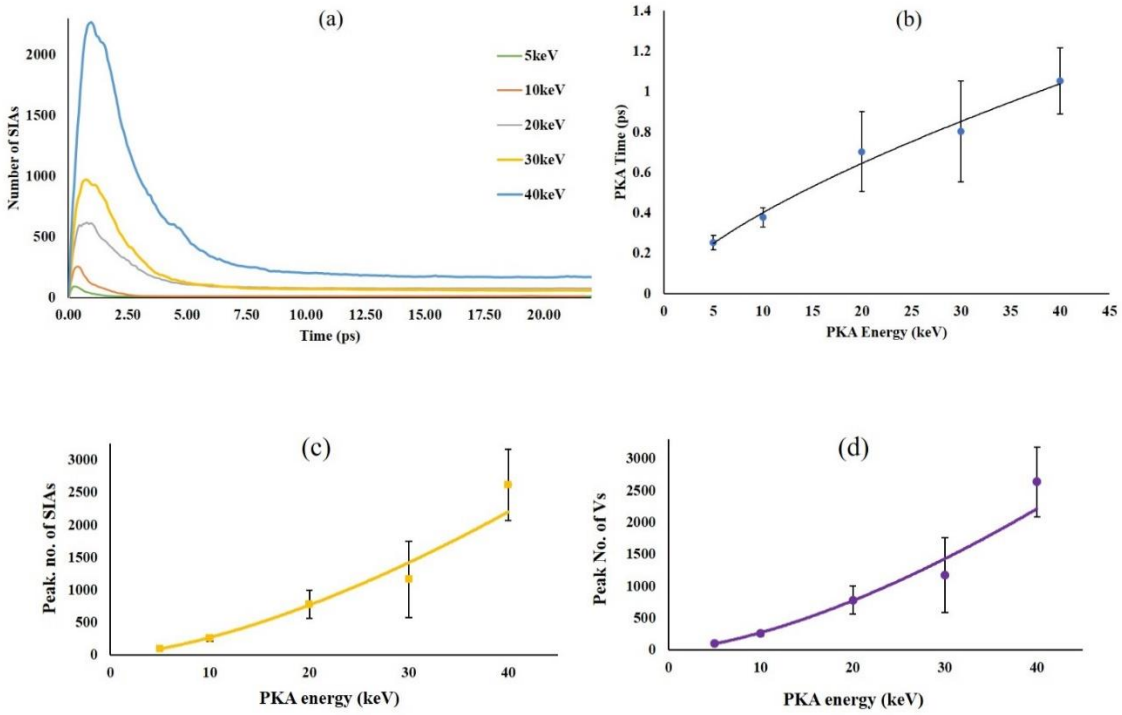

Figure 4. 3 (a) Number of SIAs dynamic evolution and with several PKA energy, (b) damage peak average time shift with changing the PKA energy with standard deviation, (c) number of SIAs at peak as a function of PKA energy and (d) number of Vs at peak as a function of PKA energy

The number of defects at peak time as a function of PKA energy has been shown in Figure 4.3 (c and d). The number of defects during peak time increase as a power law

$$N_{peak} = aE_{pka}^{b} \quad (2)$$

by increasing PKA energy, where N_{peak} is the number of defects (SIA and Vs) during damage peak, E_{pka} is the PKA energy, a = 7.9 and b = 1.5 (for both SIAs and Vs) are constant. It is expected to do if the computer-generated defect numbers for presentation at COSIRES'94[26] model are considered for the ballistic phase except for 40 keV. The deviation for maximum defects (for 40 keV) during peak time from the linear dependence could be

associated with the generation of shock waves by a cascade that increases the number of displaced atoms[27].

4.4.3 Surviving Defects

The number of survived defects produced by the end of a cascade evolution is primarily interested in estimating radiation damage. The surviving atomic defects may contribute to subsequent defect mobility or radiation-induced microstructural changes in the nanomaterials. After the recombination or quenching stage, only a reduced fraction of defects generated in the collisional phase survived through the thermal-spike-enhanced recombination phase. An average number of surviving defects after the cascade simulation (∼20 ps) has been shown in Figure 4.4 as a function of PKA energy. These results demonstrate that PKA energy has a significant influence on equilibrated defects. The surviving number of defects increases with increasing PKA energy. The number of surviving defects N_{NRT} produced per cascade is conventionally expressed by the Norgett-Robinson-Torrens (NRT) formula[28]

$$N_{NRT} = 0.4\ \frac{E_P}{\overline{E_d}} \tag{3}$$

where $\overline{E_d}$, is the average threshold energy for defects formation and Fe is equal to 40 eV and E_P is the damage energy available for elastic collisions and approximately equal to E_{PKA} when electronic losses are not considered. This expression is based on a binary collision description and neglects the many-body effects in the thermal-spike phase. The below empirical power presents an alternative way of expressing the above equation result law[29]

$$N_F = a(E_{PKA})^b \tag{4}$$

where N_F is the number of defects, and E_{PKA} is the primary knock-on atom energy, a and b are fitting parameters. The surviving defects increase gradually with an increase in the PKA energy. The reason is that the PKA produced a subsequent chain of atomic displacement events in the sample material as soon as energy is provided to the PKA. The energy of the PKA is then transferred to many other atoms of the sample material during multiple atomic interactions, and these collisional events continue until the energy transfer to the PKA is distributed over the entire volume of the simulation cell, and no atom has energy greater than the threshold displacement energy of that material[24]. In the case of Fe, for 10 keV, Stoller[30] showed the number of surviving defects follow the empirical power law where a = 5.67 and b = 0.779 for 100 K; however, our results follow the empirical power law, but coefficient values are: a = 1.096 and b = 1.282 for SIAs and a = 1.036 and b = 1.333 for Vs. This difference could be the reason for the bulk Fe system and Fe NP system. Moreover, these coefficients also depend on temperature[31], and the maximum number of defects were observed at room temperature. At higher temperatures, atom recombination and return to atomic sites are higher because the atoms are in higher energy level[31]. Another reason could be the size of our particle system because the scientist uses a bulk system for larger PKA energy. Figure 4.4 demonstrates that vacancy defects remain more than interstitial defects. This reason is, SIAs are mobile than Vs[32], and more PKA energy gives more mobility that some SIA can get enough energy to leave the Fe NP.

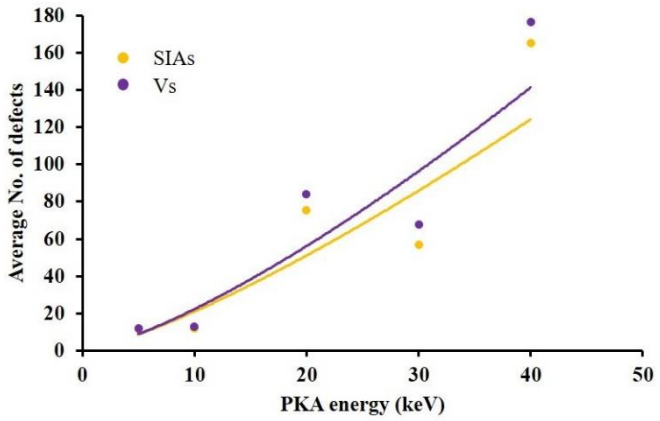

Figure 4. 4 Number of surviving defects as a function of PKA energy in Fe (yellow represents SIAs and purple for Vs) at 300 K

4.4.4 Cluster Size Analysis

The propensity of defect cluster formation and the production mechanism of large defect clusters are always pointed to practical interest for analyzing the radiation damages. This is because the defect clusters of smaller sizes behave as nuclei for the evolution of prolonging defects that eventually may lead to changes in the physical and mechanical properties of the irradiated nanomaterials. Besides the production of survived defects, we have examined the SIAs and Vs cluster size with respect to the PKA energies. We define clusters (aggregates) based on defects being within 3 Å of a defect, i.e., for vacancy-vacancy (V-V) distance and interstitial – interstitial (SIA-SIA) distance less than 3 Å. The cluster size distributions of interstitials and vacancies for Fe over the six random directions at each of the PKA energies explored are presented in Figure 4.5 (a) and (b), where Figure 4.5a and 4.5b for SIAs and Vs, respectively. The cascade cluster graphs show most of the interstitial and vacancy clusters are single for Fe. D.J Bacon et. al. observed[29] that most interstitial and vacancy clusters contain single defects for cascade in Fe for PKA energies 10 keV and 50 keV. In addition, lower PKA energy produces smaller size cluster defects compared with large PKA energy. However, in

most cases, vacancy clusters are bigger than SIA clusters, and almost in all cases, bigger clusters are available at the surface of the Fe nanoparticle.

This trend explains that vacancies in the irradiated materials remain close to the PKA path, whereas interstitials are scattered away from the path[24,33]. Generally, during the collisional phase,

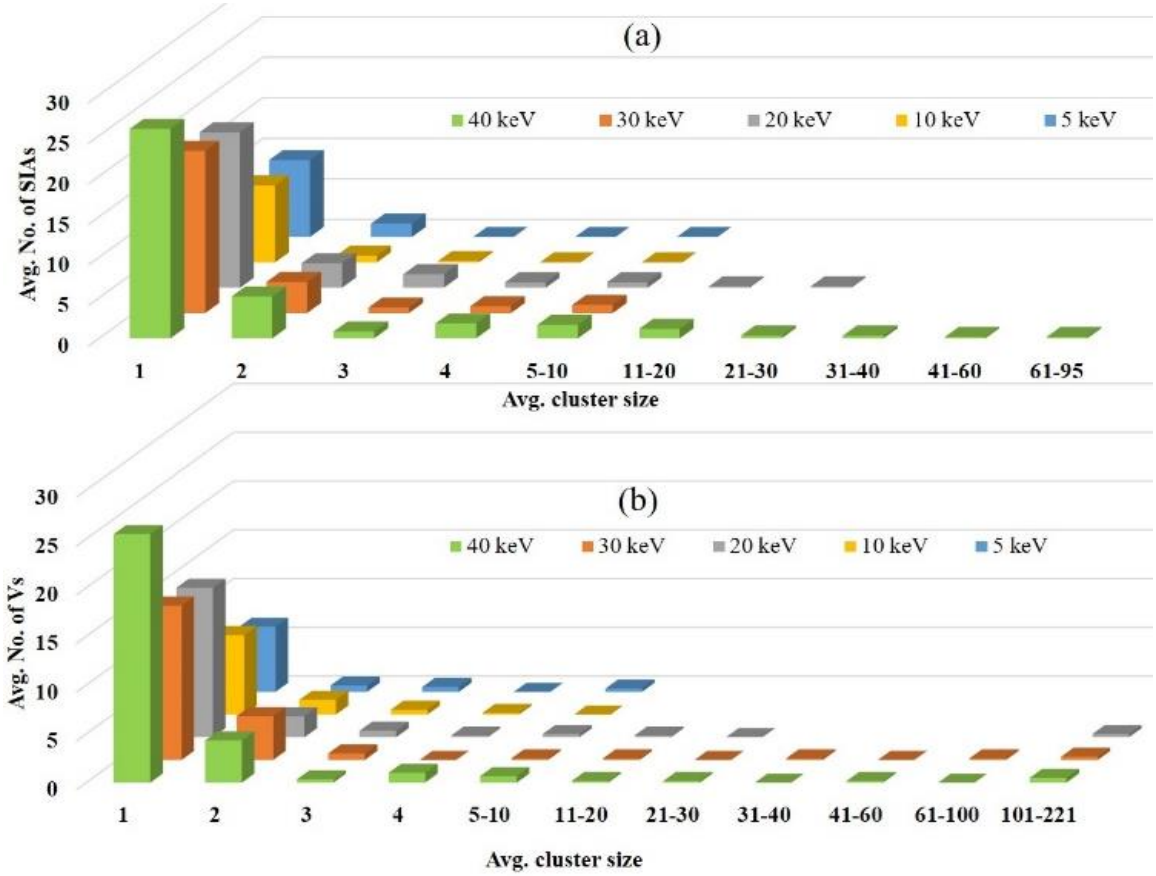

Figure 4. 5 Distribution of cluster sizes for all cascades as a function of PKA energy. (a) The average number of SIAs and (b) the average number of Vs.

PKA's energy displaces many energetic atoms along the cascade path. Those energetic atoms use their energies either by replacement collisions with neighbors or by moving away from

the path of the PKA into the surrounding crystal. In both cases, vacancies are left near the PKA path to form a depleted zone, and they can aggregate to form large clusters.

4.4.5 Cluster Orientation

The largest SIA cluster has been found at the end of the simulation, which contains around 92 SIAs (Figure 4.6(b) the largest SIA (yellow) cluster) for 40 keV, where 86% of them are single clusters and 13% are smaller size clusters. Large vacancy clusters have been observed with the 124 vacancies (Figure 4.6(b), the largest V (purple) cluster). In all the cases, damage creates one big SIA and one V cluster. Figure 4.6(a) represents the orientation of the defects after a simulation time of 22 ps. To better understand the defect orientation, a supplementary video has been provided. In Figure 4.6(a), it is shown that 152 of the vacancy defects stay inside the Fe nanoparticle, whereas SIA defects reach the nanoparticle's surface. During the irradiation in heavy, dense metals, 92 interstitials are formed at the outskirts of the cascades; vacancies are left in the thermal spike. It has a strong tendency to rearrange perfectly. In that case, the empty volume of the liquid is pushed towards the center of the cascade, and it forms a loose network of single vacancies or vacancy clusters[34]. For the interstitials, two mechanisms have been reported[34], one of them is atom rearrangement after the thermal spike stage and isolating a molten zone with an excess of atoms and leaving behind SIA clusters[35]. The other mechanism is that the interaction of two hypersonic recoils produces supersonic shock fronts near the thermal spike region and leads to the stronger front injecting atoms into the low-density core of the other one, thus leading to the formation of SIA rich region[36]. Later, it is found that interstitials are more mobile than vacancies[32], and They can produce stable damage near to the surface[37].

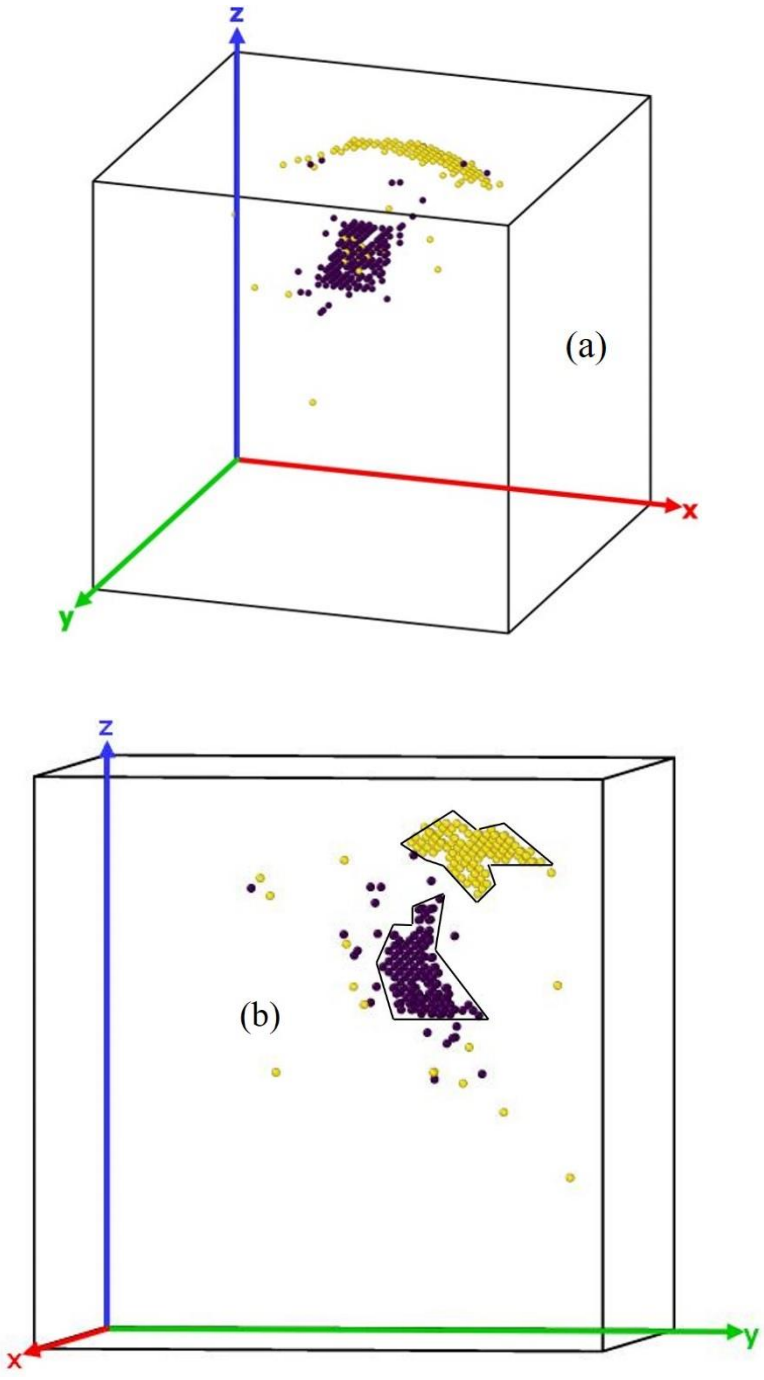

Figure 4. 6 (a) SIAs (yellow) and Vs (purple) orientation for 40 keV with different positions. (b) big SIA cluster (92 SIAs) and big V cluster (124 Vs). Axis positions are different, just for the best view of the cluster defects

4.5 Conclusion

In summary, we have discussed our MD simulation on high energy radiation damages in Fe NPs, which could serve as the radiation detection used in nuclear reactors. This work has shown that the radiation creates a small number (average 0.114 % SIAs and 0.122% Vs for 40 keV) of defects. The defects are either single SIAs or Vs. In each of the cases, they produce one chunk of a big cluster. The cluster of SIAs stays near the nanoparticle's surface; however, the Vs one stays inside the nanoparticle. The Fe SIA clusters, which remain near the surface, could predict the reason for NP structure change[38–41] and cluster formation[42] during the irradiation. The Vs clusters inside the NPs also anticipate the formation of voids in the irradiated BCC Fe NP.

Acknowledgment

This work was supported by the U.S. Department of Energy (DOE) under Contract DE-FC07-08ID14926 by the INL-LDRD administered by CAES under the DOE Contract DE-AC07-05ID14517. This research has also been used of Idaho National Laboratory computing resources supported by the Office of Nuclear Energy of the U.S. Department of Energy and the Nuclear Science User Facilities under Contract No. DE-AC07-05ID14517.

4.6 References:

1. Manasreh, O. *Introduction to Nanomaterials and Devices*. *National Centre for Catalysis Research* (John Wiley & Sons, Inc., 2011). doi:10.1002/9781118148419
2. Qiang, Y. *et al.* Iron/iron oxide core-shell nanoclusters for biomedical applications. *J. Nanoparticle Res.* **8**, 489–496 (2006).
3. Zhang, X. X. *et al.* Magnetic properties of Fe nanoparticles trapped at the tips of the aligned carbon nanotubes. *J. Magn. Magn. Mater.* **231**, 9–12 (2001).
4. Tamaura, Y. & Tahata, M. Complete reduction of carbon dioxide to carbon using cation-excess magnetite. *Nature* **346**, 255–256 (1990).
5. Nurmi, J. T. *et al.* Characterization and properties of metallic iron nanoparticles: Spectroscopy, electrochemistry, and kinetics. *Environ. Sci. Technol.* **39**, 1221–1230 (2005).
6. Wang, C. B. & Zhang, W. X. Synthesizing nanoscale iron particles for rapid and complete dechlorination of TCE and PCBs. *Environ. Sci. Technol.* **31**, 2154–2156 (1997).
7. Khanal, L. R., Williams, T. & Qiang, Y. High-temperature investigation on morphology , phase and size of iron / iron- oxide core – shell nanoclusters for radiation nanodetector. (2018).
8. Jiang, W. *et al.* In situ study of nanostructure and electrical resistance of nanocluster films irradiated with ion beams. *Adv. Funct. Mater.* **24**, 6210–6218 (2014).
9. Signorini, L. *et al.* Size-dependent oxidation in iron/iron oxide core-shell nanoparticles. *Phys. Rev. B - Condens. Matter Mater. Phys.* **68**, 1–8 (2003).

10. Zhang, G., Liao, Y. & Baker, I. Surface engineering of core/shell iron/iron oxide nanoparticles from microemulsions for hyperthermia. *Mater. Sci. Eng. C* **30**, 92–97 (2010).

11. Oldenburg, S. J., Averitt, R. D., Westcott, S. L. & Halas, N. J. Nanoengineering of optical resonances. *Chem. Phys. Lett.* **288**, 243–247 (1998).

12. Beyerlein, I. J., Demkowicz, M. J., Misra, A. & Uberuaga, B. P. Defect-interface interactions. *Prog. Mater. Sci.* **74**, 125–210 (2015).

13. Zinkle, S. J. & Busby, J. T. Structural materials for fission & fusion energy. *Mater. Today* **12**, 12–19 (2009).

14. Zinkle, S. J. & Snead, L. L. Designing Radiation Resistance in Materials for Fusion Energy. *Annu. Rev. Mater. Res.* **44**, 241–267 (2014).

15. Plimpton, S. Fast parallel algorithms for short-range molecular dynamics. *Journal of Computational Physics* **117**, 1–19 (1995).

16. Stukowski, A. Visualization and analysis of atomistic simulation data with OVITO-the Open Visualization Tool. *Model. Simul. Mater. Sci. Eng.* **18**, (2010).

17. Theil Kuhn, L. *et al.* Core-shell iron-iron oxide nanoparticles: Magnetic properties and interactions. *J. Magn. Magn. Mater.* **272**–**276**, 1485–1486 (2004).

18. Lacroix, L. M. *et al.* Stable single-crystalline body centered cubic Fe nanoparticles. *Nano Lett.* **11**, 1641–1645 (2011).

19. Mendelev, M. I. *et al.* Development of new interatomic potentials appropriate for crystalline and liquid iron. *Philos. Mag.* **83**, 3977–3994 (2003).

20. Nguyen, N. H., Henning, R. & Wen, J. Z. Molecular dynamics simulation of iron nanoparticle sintering during flame synthesis. *J. Nanoparticle Res.* **13**, 803–815 (2011).

21. Ou, X. Molecular dynamics simulations of fcc-to-bcc transformation in pure iron: a review. *Mater. Sci. Technol. (United Kingdom)* **33**, 822–835 (2017).

22. Byshkin, M. & Hou, M. Phase transformations and segregation in Fe-Ni alloys and nanoalloys. *J. Mater. Sci.* **47**, 5784–5793 (2012).

23. Zou, P. F. & Bader, R. F. W. A topological definition of a Wigner–Seitz cell and the atomic scattering factor. *Acta Crystallogr. Sect. A* **50**, 714–725 (1994).

24. Was, G. S. *Fundamentals of radiation materials science: Metals and alloys,Springer-Verlag Berlin*. *Fundamentals of Radiation Materials Science: Metals and Alloys* (2007). doi:10.1007/978-3-540-49472-0

25. Terentyev, D. A. *et al.* Displacement cascades in Fe-Cr: A molecular dynamics study. *J. Nucl. Mater.* **349**, 119–132 (2006).

26. Bacon, D. J., Calder, A. F. & Gao, F. Defect production due to displacement cascades in metals as revealed by computer simulation. *J. Nucl. Mater.* **251**, 1–12 (1997).

27. Zolnikov, K. P., Korchuganov, A. V. & Kryzhevich, D. S. Molecular dynamics simulation of primary radiation damage in Fe-Cr alloy. *J. Phys. Conf. Ser.* **774**, (2016).

28. Norgett, M. J., Robinson, M. T. & Torrens, I. M. A proposed method of calculating displacement dose rates. *Nucl. Eng. Des.* **33**, 50–54 (1975).

29. Bacon, D. J., Gao, F. & Osetsky, Y. N. Computer simulation of displacement cascades and the defects they generate in metals. *Nucl. Instruments Methods Phys. Res. Sect. B Beam Interact. with Mater. Atoms* **153**, 87–98 (1999).

30. Stoller, R. E. Point defect survival and clustering fractions obtained from molecular dynamics simulations of high energy cascades. *J. Nucl. Mater.* **233**–**237**, 999–1003 (1996).

31. Sahi, Q. U. A. & Kim, Y. S. Primary radiation damage characterization of α-iron under irradiation temperature for various PKA energies. *Mater. Res. Express* **5**, 0–12 (2018).

32. Avdeeva, A. V. The kinetics of point defects in metals under ion irradiation. *J. Phys. Conf. Ser.* **653**, (2015).

33. Sand, A. E., Dudarev, S. L. & Nordlund, K. High-energy collision cascades in tungsten: Dislocation loops structure and clustering scaling laws. *Epl* **103**, (2013).

34. Nordlund, K. *et al.* Primary radiation damage: A review of current understanding and models. *J. Nucl. Mater.* **512**, 450–479 (2018).

35. Nordlund, K., Ghaly, M. & Averback, R. Defect production in collision cascades in elemental semiconductors and fcc metals. *Phys. Rev. B - Condens. Matter Mater. Phys.* **57**, 7556–7570 (1998).

36. Calder, A. F., Bacon, D. J., Barashev, A. V & Osetsky, Y. N. On the origin of large interstitial clusters in displacement cascades. *Philos. Mag.* **90**, 863–884 (2010).

37. Nordlund, K., Keinonen, J., Ghaly, M. & Averback, R. S. Coherent displacement of atoms during ion irradiation. *Nature* **398**, 49–51 (1999).

38. Nita *, N., Schaeublin, R., Victoria, M. & Valiev, R. Z. Effects of irradiation on the microstructure and mechanical properties of nanostructured materials. *Philos. Mag.* **85**, 723–735 (2005).

39. Nita, N., Schaeublin, R. & Victoria, M. Impact of irradiation on the microstructure of nanocrystalline materials. *J. Nucl. Mater.* **329**–**333**, 953–957 (2004).

40. Radiguet, B., Etienne, A., Pareige, P., Sauvage, X. & Valiev, R. Irradiation behavior of nanostructured 316 austenitic stainless steel. *J. Mater. Sci.* **43**, 7338–7343 (2008).

41. Lian, J. *et al.* Ion beam-induced amorphous-to-tetragonal phase transformation and grain growth of nanocrystalline zirconia. *Nanotechnology* **20**, (2009).

42. Li, J. *et al.* In situ heavy ion irradiation studies of nanopore shrinkage and enhanced radiation tolerance of nanoporous Au. *Sci. Rep.* **7**, 1–10 (2017).

Chapter 5: Molecular Dynamics Simulation of Radiation Effects on Core-Shell Ti-TiO_2 Nanoparticles

Mohammad Zahidul Hossain Khan, Lokendra Khanal, Rabindra Khanal, Jinming Zhang and You Qiang*

Department of Physics, University of Idaho, Moscow, ID-83844, USA

*: Email: youqiang@uidaho.edu

5.1 Abstract:

The core-shell nanoparticles (CS-NPs) and NP-assembled nanomaterials have become an important research area in the last decades due to their potential applications in various fields like catalysts, magnetic and biomedical applications, and radiation detection applications. In this work, the radiation effects on core-shell Ti-TiO2 nanoparticles were studied by molecular dynamics simulations. A series of several cascades for each neutron recoil energy (50 keV, 100 keV, 150 keV, 200 keV, and 250 keV) were simulated for different temperatures (100 K, 300 K, and 500 K) to assure statistical precision. The simulation results have shown that radiation creates a small number of defects with either single interstitials (SIAs) and/or vacancies (Vs). In each case, the accumulated defects are both on the surface of NPs and in the interface zone between the core and shell. In all cases, the core remains intact, but the mean square displacement for CS-NPs changes with increasing recoil energy.

5.2 Introduction:

In the domain of nanotechnology, nanoparticles (NPs) with size in the range of 1-100 nm [1,2]occupy a significant position. . Being on the edge of the macroscopic and atomic realm,

NPs show several enthralling properties which emerge at the frontier between materials physics and chemistry, and many other fields, such as electronics, biomedical, pharmaceutical, optics, and catalysis. Among the NPs, core-shell (CS) NPs are gradually attracting more attention. These CS-NPs can consist of different combinations in close interaction, including inorganic/inorganic, inorganic/organic, organic/inorganic, and organic/organic nanomaterials.

CS-NPs are widely used in different applications such as biomedical [3–6] and pharmaceutical applications [7], catalysis [8], electronics [9], enhancing photoluminescence [10], creating photonic crystals [11], etc. Recently, the development of metallic core/TiO_2 shell particles offers activity under radiation. For instance, Ag@TiO_2 nanoparticles exhibit substantial photocatalytic activity under UV irradiation because of the accumulation of the electrons photogenerated by TiO_2 in the metallic Ag core and their discharge in the presence of electron acceptors [12]. It was also informed that TiO_2-coated titanium nanorods demonstrate enhanced photocurrent efficiency in the vis region compared with pristine TiO_2 nanotubes [13]. Moreover, it was also proclaimed that a simple and environmentally friendly synthesis of Ti-TiO_2 CS-NPs exhibiting vigorous photothermal catalytic activity in the reaction of hydrogen generation under vis/NIR light irradiation in the absence of any noble metals [14]. More importantly, the active interfaces between individual components within a CS-NP might give rise to outstanding new properties.

It was previously reported that Fe-Fe_3O_4 core-shell NPs with Fe_3O_4 as the shell and body-centered cubic (BCC) Fe as the core have very sensitive electrical conductivity and magnetic properties under Si^{2+} ion irradiation, even at shallow dose ion flux regime with the minimal effect of the temperature up to 200 °C [15]. Also, studies have shown that the average size of

the Fe in the Fe-Fe_2O_3/Fe_3O_4 core-shell structure decreases [16], and Fe core reduces its Fe valence [17] under irradiation. In addition, since the metal core-shell NPs exhibit radiation sensitivity even for low dose flux and Ti-TiO_2 CS-NPs have sensitivity for radiation, it is essential to investigate the radiation effect on core-shell Ti-TiO_2.

The TEM image Figure 5.1 shows that the Ti-TiO_2 CS-NPs with uniform and spherical shape is synthesized by nanocluster deposition system in our lab; the NP size has an average 15 nm in diameter. The CS-NPs have been utilized to make a radiation detector irrdiated by neutron beam in the near future, like what has been done for the Fe-Fe_3O_4 nanodetectors[15].

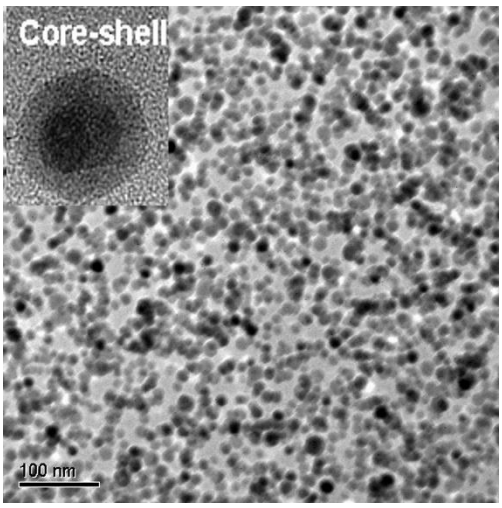

Figure 5. 1 TEM image of Ti-TiO_2 CS-NPs with a mean size of 15 nm.

For the intended purpose before actual irradiation experiments, we performed a molecular dynamics (MD) simulation on the core-shell Ti-TiO_2 NPs and investigated defect production, defect orientation, mean square displacement for all atoms with varying radiation energy under different temperatures.

5.3 Force Field Model:

For doing MD simulations, a force field is a crucial factor, so that Third-generation Charge Optimized Many-Body (COMB3) have been chosen. The COMB3 formalism is a bond-order type potential with variable charge. The general form for COMB3 is:

$$U_{tot} = U_{ele}(q,r) + U_{short}(q,r) + U_{vdW}(r) + U_{corr}(i,j,k) \quad (1)$$

where the total potential energy U_{tot} is given as the sum of the electrostatic energy $U_{ele}(q,r)$, the short-range energy $U_{short}(q,r)$, the long-range or van der Waals energy $U_{vdW}(r)$ and a correction term $U_{corr}(i,j,k)$. The COMB3 potential is constructed by fitting to an extensive experimental database and compare with other ab initio data.

The COMB3 potential can describe Titanium, Titania, Oxygen. The details of the COMB3 formalism and other examples of its applications are described elsewhere [18,19]. The development of potential for such a wide range of materials inevitably requires some compromises regarding the fidelity of any specific system. In particular, the COMB3 successfully reproduces the relative stability of these phases of Ti, with the *α*(*hcp*) phases predicted to be the ground state phase. In addition, rutile is correctly expected to be more stable than the other standard, high pressure, or hypothetical AB_2 phases[20]. The potential reproduces many of the properties of the three low Miller index rutile surfaces [(1 1 0), (0 0 1), and (1 0 0)]. This potential has been successfully used in the previous investigation of Ti and TiO_2 for various purposes. Therefore it is an excellent choice to examine metal clusters on TiO_2, which are essential heterogeneous catalysts [19,21–23]. They have developed parameters for metallic Ti and TiO_2 within the framework of the COMB3 potential.

5.4 Simulation Method

The MD simulations were conducted using the Large-scale Atomic Molecular Massively Parallel Simulator (LAMMPS) code developed by Sandia National Laboratory [24]. Results were visualized in Open Visualization Tool (OVITO) developed by Stukovski [25].

The Ti-TiO_2 CS-NP was spherical with a diameter ~15 nm, where ~10 nm was core diameter, and ~ 2.5 nm was shell thickness, as shown in figure 5.1. The previous work [26] has shown that the core-shell nanoparticles' average size is 15–21 nm, and the thickness of the oxide shell is ~2.6 nm, where the core diameter is 9-15 nm. The core-shell Ti-TiO_2 structure was constructed by two grains with perfect lattice, as introduced by Pierre Hirel in his work [27]. Ti-TiO_2 NPs were constructed from an hcp core of Ti and a rutile shell of TiO_2. The Ti core diameter ~10 nm contains 31531 Ti atoms, and the thickness of the TiO_2 shell contains 116783 atoms. Core-shell Ti-TiO_2 NPs were separated by a gap of 3.0 Å between the core and shell atoms, as illustrated in the structure of core-shell shown in Figure 5.2. The x, y and z directions correspond to the [1 0 0], [0 1 0] and [0 0 1] crystal axes of the core-shell Ti-TiO_2, respectively.

The system was equilibrated using isothermal-isobaric (npt) at 300 K for 20 ps. Then the molecular statics (MS) technique was used by the conjugate gradient (CG) to find the most stable structure of the core-shell system.

The simulation box had a cubic geometry containing about 148314 atoms, and the recoil neutron energies were set to vary the radiation energy from 50 keV to 250 keV during the whole study. To prepare the core-shell configurations for collision cascade simulations, the outermost layer of the simulation box with 5 Å thickness was fixed throughout the collision

cascade simulation. To control the temperatures, the outer part of the box is defined as the thermostat region. Berendsen and Nose-Hoover temperature control methods[28] were applied to the outer region to control the temperature of the whole system during the relaxation and incidence period, respectively. The cascade simulation has a total length of 22 picoseconds, divided into two stages. In the first stage, cover the most period of the thermal spike effect, and the number of displaced atoms reached its peak, and the timestep was set up to 0.2 femtoseconds each step. The last stage included the system's cooling and recombination of defects; therefore, it is relatively longer in simulation time. The periodic boundary conditions were adopted at the X, Y, and Z directions, corresponding to the crystal orientations.

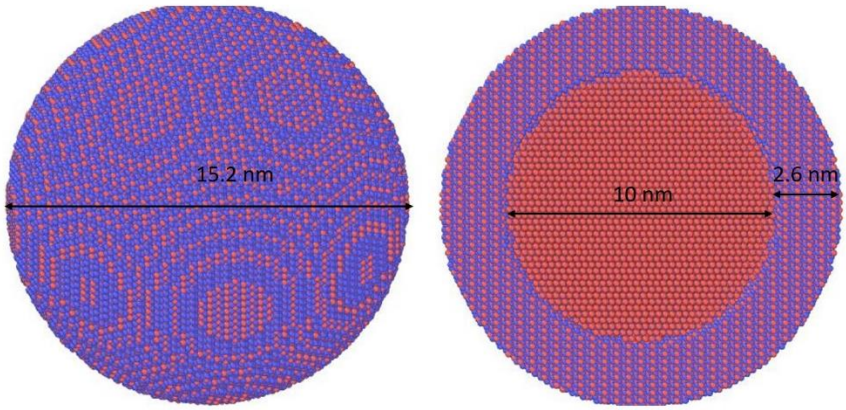

Figure 5. 2 Core-shell NP. The left side image illustrates the entire system, and the right-side image cross-sectional view. The core is constructed by Ti (hcp phase), and the shell has been built by TiO_2 (rutile)

The simulations were run at 100 K, 300 K, and 500 K to study the different temperature effects of the cascade on core-shell structures. To incorporate statistical variations in the simulations, for each core-shell configuration, 10 simulations were carried out.

Wigner-Seitz method was used to analyze the defects during the MD simulations [29]. The reference structure was the initial structure at the start of the simulation before the recoil energy was initiated. The initial structure was divided into cells, and only one atom was supposed to be in each cell. During the cascade simulation, atom numbers in every cell are checked every timestep. For every cell, if the atom number is zero, it is defined as a vacancy. Similarly, interstitial is determined if there are two or more atoms in one cell. The atom type is also analyzed in the process of defining the interstitials.

5.5 Defect Formation Energy (DFE):

Single interstitial (SIA) and vacancy (V) formation energies (E_S^f and E_V^f respectively) were calculated in shell, interface, and core using the MS technique. An interstitial was created by adding an extra atom, and a vacancy was created by deleting an atom. The system was first equilibrated by isothermal-isobaric (npt) at 300 K for 20 ps. Then MS technique was used by the conjugate gradient (CG) to find the most stable structure of the core-shell system, and the system's energy was calculated. The E_S^f and E_V^f ware calculated as the difference in energy between the initial configuration and the configuration with interstitial/vacancy

$$E_S^f = E_f - \frac{N_0 + 1}{N_0} * E_i \qquad (2)$$

$$E_V^f = E_f - \frac{N_0 - 1}{N_0} * E_i$$

where E_f, E_i, and N_0 represent the final energy after the atom is adding/removed from the cell, the initial energy before the atom was adding/removed, and N_0 is the total number of atoms in the cell before the interstitial/vacancy. Several simulations have been done for SIAs/Vs at different locations from shell to core through the interface to determine the defect

formation energy as a distance function. A total of 59 simulations were executed by either adding an atom or removing an atom. These simulations were accomplished starting from 25 Å (angstrom) from one side and 30 Å on the other side with a step size of 2.5 Å.

From the simulations, the defect formation energy, mean square displacement of atoms, the number of Frenkel pairs (FPs), and defect distribution was determined for core-shell Ti-TiO_2 under irradiation. This study on core-shell NP could understand the ability of defect accumulation near the core-shell interface. Figure 5.3 illustrates the simulation summary. Initially, the CS nanoparticle was equilibrated, and DFE was calculated using the MS technique. Finally, the MD was used to produce a cascade simulation using recoil energy.

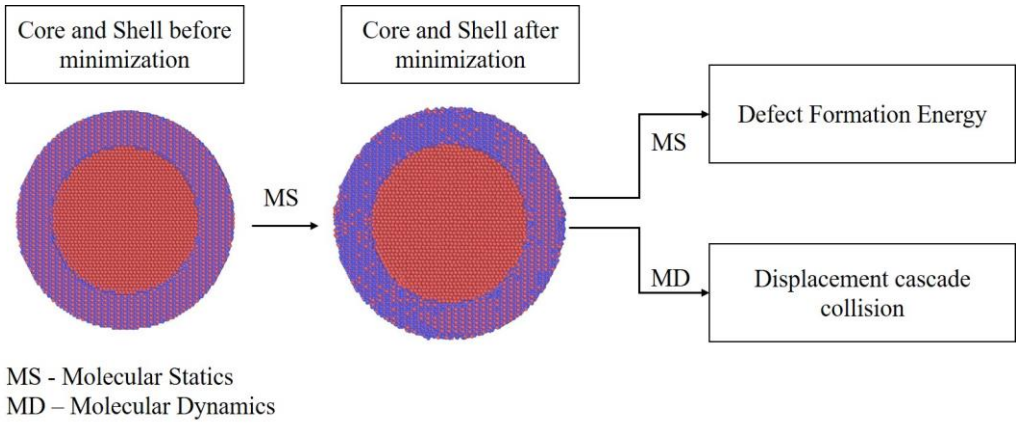

Figure 5. 3 Workflow of the collision cascade simulation for core-shell Ti-TiO_2

5.6 Results and Discussion:

The results were obtained by averaging ten MD cascade simulations for each combination of temperature and PKA energy. Cascade simulations continued until recombination of vacancy

and interstitial was achieved. When the recoil energy transferred to PKA, a sequence of atomic displacements occurred to evolve in the simulation system. The displacement cascade produced several defects, interstitials, and vacancies. After displacement cascade initiation, the peak number of atomic defects and the surviving number of Frenkel pairs were analyzed. As soon as the energy was transferred to PKA (i.e., the ballistic phase), the number of atomic displacements and the size of the radiation damage region increased simultaneously via temporal evolution. A total number of displaced atoms reached its maximum in the ballistic stage, which recombined and got a relatively stable number of Frenkel pairs. We found a similar temporal behavior of thermal spike, its lifetime and produced several defects for each given recoil energy. To obtain a clear dependence of energy and temperature, detailed comparisons of damage properties are shown below.

5.6.1 Defect Formation Energy (DEF):

The defect formation energies for core-shell Ti-TiO_2 are shown in Figure 5.4, which illustrates that the defect formation energies were relatively lower in the interface of the core-shell NPs than in the shell and core side. This could be because of the spatial atomic arrangement in the interface giving extra space for the accommodation of defects. The lower defect formation energy at the interface would also favor the trapping of these defects at interfaces. A positive defect formation energy signifies an endothermic process and a negative one an exothermic process [30]. The decrease in E_V^f means, vacancies can be created easily and attracted between vacancies and interface whereas negative E_V^f implies energy of the system actually drops by creating vacancies [31]. Further investigation also reveals that the sites where E_V^f are negative consider as an unstable site and tend to recombine with the

available interstitials [32,33]. This means that irradiation-created vacancies at these sites or the vacancies coming from the bulk will be instantly annihilated with the interstitial.

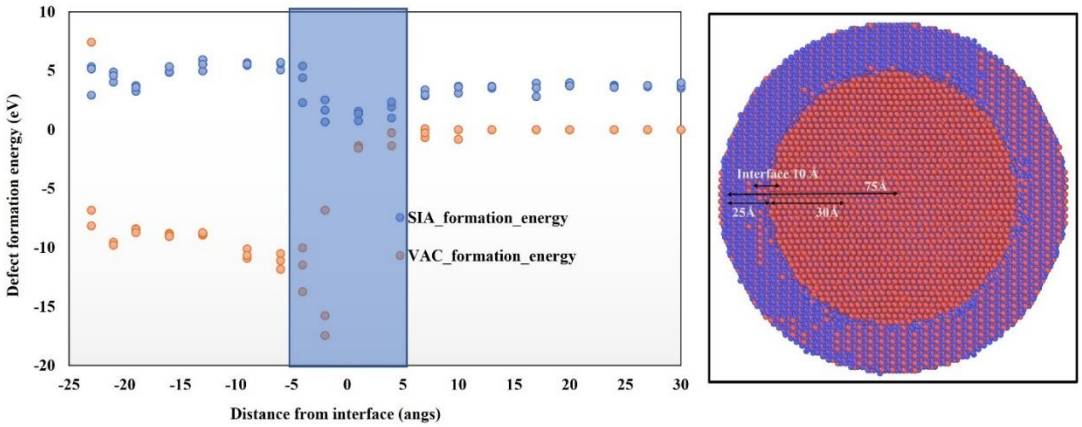

Figure 5. 4 Defect formation energies for interstitials and vacancies for core-shell Ti-TiO_2. The blue region -5 to 5 is the interface between the core and shell that occurred the DFE drops.

5.6.2 Peak Time Features and Ballistic Stage

For understanding the cascade, the maximum number of damages during the thermal spike period and the survived number of defects (Frenkel pairs) as a function of recoil energy have been studied for different temperatures.

In cascade simulations, the peak number of defects generated is also one of the main features for characterizing the ballistic/peak displacement cascade stage. We determined the dependence of atomic point defects caused at peak number of defects as a function of PKA energy (Figure 5.5). The peak number of defects increases linearly by increasing PKA energy. As described earlier, sub-cascades appear as the several lower energy cascades for high PKA energy. Moreover, these peak numbers of defects also exhibit a small but clear temperature dependence. This difference also tends to increase with PKA energy going up.

Overall, the range of the number of defects generated with high energy PKAs at different temperatures was larger than those with low cascade energy, which can be attributed to the much more extended period of the thermal spike for higher irradiation temperature and recoil energy.

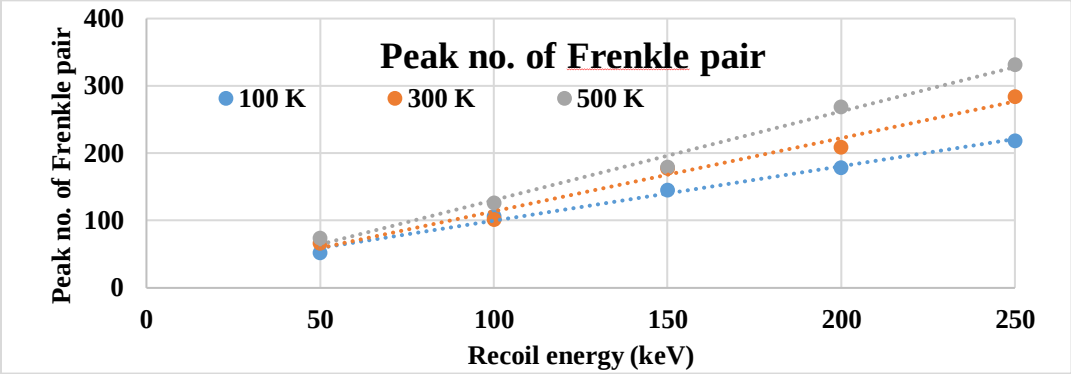

Figure 5. 5 Number of defects at peak time versus recoil energy at different temperatures

5.6.3 Surviving Frenkel Pairs and Recombination Stage

The surviving number of Frenkel pairs (FPs) generated by the end of a cascade evolution is a parameter of primary interest for estimating the radiation damage because the surviving atomic defects may contribute to radiation-induced microstructural changes and subsequent defects mobility in the material. After the recombination/relaxation stage, only a reduced fraction of defects generated in the ballistic phase survived through the thermal-spike-enhanced recombination phase. An average number of surviving Frenkel pairs after the cascade simulation (~20 ps) is given in figure 5.6 as a function of irradiation temperature and recoil energy, respectively. These results demonstrate that irradiation temperature considerably influences the number of equilibrated defects. The surviving number of defects increased with an increase in irradiation temperature, attributed to the increased motion and recombination of defects at a higher temperature. The chances of surviving FPs are larger at

elevated temperatures because the atoms are in higher energy levels. The period of thermal spikes increases at elevated temperatures, allowing defects to be more mobile before equilibrium, leading to more vacancies and interstitials. The number of surviving Frenkel pairs versus PKA energy indicates a continuous rise with the increasing PKA energy (figure 5.6), which could be well-described by the empirical power law [5]. For different PKA energies, the power law is given as follows.

$$N_{FP} = A(E_{PKA})^{b} \quad (3)$$

Where E_{PKA} is the energy of the PKA, and A and b are constants. As seen in figure 6, the values of constant A = 0.5, 0.9, and 2.1, and exponent b = 1.0, 0.9, and 0.8 are for the temperatures of 100, 300, and 500 K, respectively.

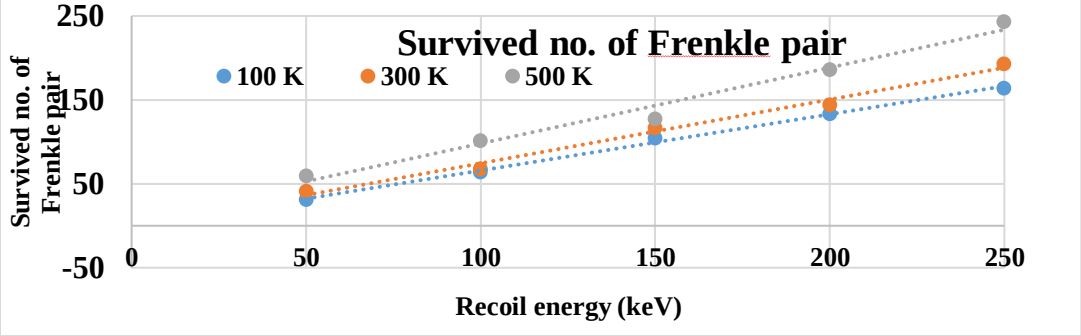

Figure 5. 6 Survived defects versus recoil energy at different temperatures

5.6.4 Mean Square Displacement:

In MD simulation, the movement of the particles happens continuously with time, and each particle has changed position at each instant. Mean square displacement (MSD) is the average of the square of particle displacement, which is often used to analyze the mobility of particles [34]. As the atoms can only move around their equilibrium positions in the ideal solid, the MSD quickly saturates. Figure 5.7 illustrates the MSD for core-shell Ti-TiO_2 NP at

300 K temperature as a function of time for several recoil energy. MSD for core-shell Ti-TiO_2 NP at 100 K and 500 K temperature has been provided in supplementary materials. At 300 K, the MSD of Ti-TiO_2 atoms increased almost linearly in the ballistic phase with the increasing recoil energy, which eventually leveled off during the whole system underwent a recombination process. During the recombination process (1 ps to 11 ps), high dense collisions transfer from the thermal spike zone to the whole particle system.

For this reason, MSD fluctuates for time which is shown in figure 5.7. The Ti and O atoms vibrated at the lattice position upon the recombination, and their MSDs were stabilized at specific values. Figure 5.7 also demonstrates a big MSD gap between 100 keV and 150 keV recoil energy. The reason is that the sub cascade form by splitting atomic displacement cascades triggered by secondary knock-on atoms (SKAs) with energy lower than the PKA energy. These sub-cascades generated by SKAs have shorter peak times than the main cascade, decreasing the peak time linearly with increasing PKA energy [35]. It is also supported by figure 5.5, where the peak number of FPs changes 100 keV to 150 keV.

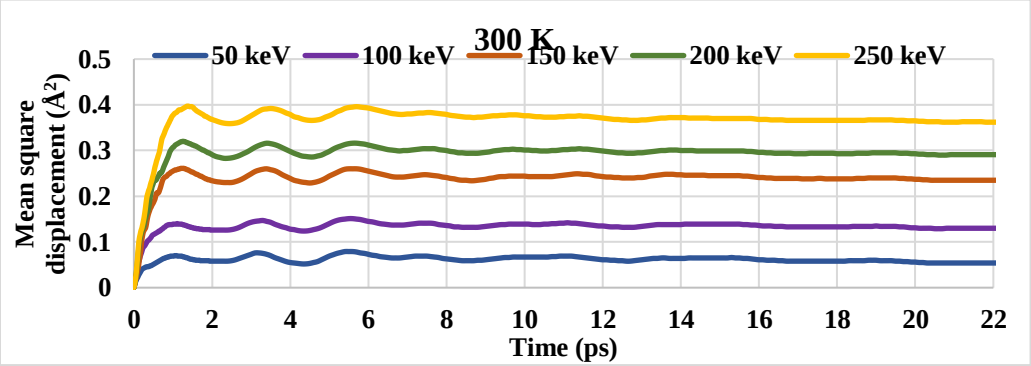

Figure 5. 7 Mean square displacement as a function of simulation time for several recoil energy for 300 K.

5.6.5 Defect Distribution:

Figure 5.8 illustrates one simulation’s survival defect distribution for 250 keV recoil energy with the surrounding temperature at 500 K. Figure 5.8(a) represents the interstitial defects distribution, and figure 5.8(b) represents the vacancies defects distribution. Several colors have been used in this figure 5.8 for illustrating the Ti (yellow) and O (violet) from rutile and metal Ti (aqua). In all the cases, defects accumulate either at the surface of the core-shell NP and interface between core and shell at the end of the simulation. Interfaces, such as free surfaces, phase, and grain boundaries, are known for trapping defects. Generally, interface sites have much lower defect formation energies than bulk sites. Some sites' vacancy/interstitial energy is higher than the bulk lattice, thus indicating that these sites will be more prone to capturing radiation-induced defects[36]. On average, 4.4% of vacancies and 3.5% of interstitials stay as a single defect, whereas the rest of the defects remain as a cluster defect. About 59% of vacancies and 64% of interstitial defects gather at the core and shell interface, whereas the rest stay near the shell's surface and bulk side of the NP. More interstitial defects accumulate near the interface of the core and shell, and the reason is interstitial defects have more mobility energy than vacancy defects.

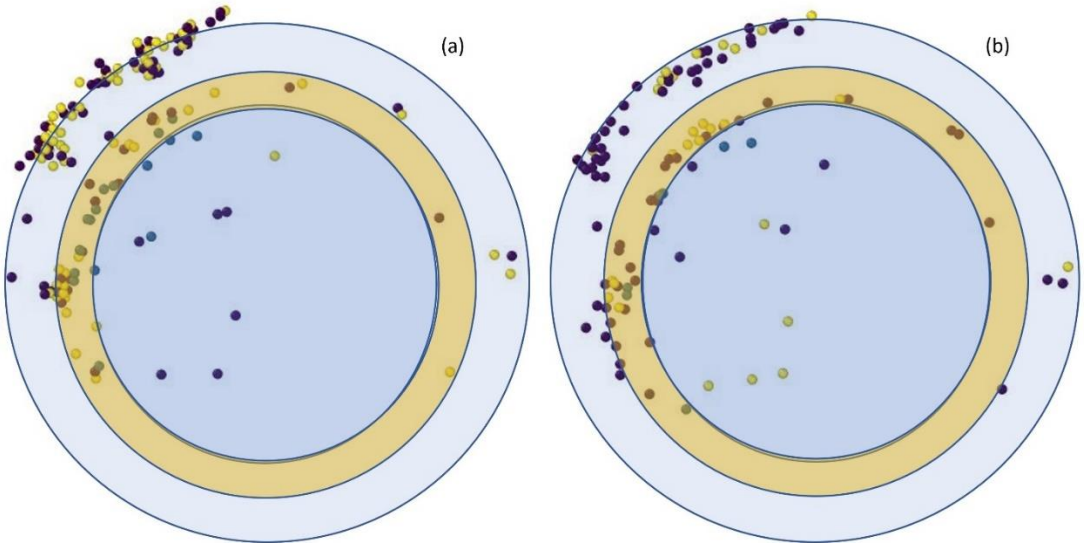

Figure 5. 8 Survived defect distribution. (a) represents the interstitial defect distribution at the end of the simulation where yellow, purple, and aqua represent the charged Ti, charged O, and metal Ti respectively. (b) represents the vacancy defect distribution at the end of the simulation where yellow, violet, and aqua represent the charged Ti, charged O, and metal Ti respectively.

5.7 Conclusion

In summary, we have discussed MD simulation on high energy radiation effects in core-shell Ti-TiO_2 NPs, which could serve as the radiation detection to be used in nuclear reactors. This work has shown that the radiation creates defects, and the defects are either SIAs or Vs. Surviving defects increase with increasing neutron energy and temperature. On average, 59% of vacancies and 64% of interstitials defect gather at the core and shell interface of the NPs, and the rest of the defects stay either surface or bulk side. In all cases, mean square displacement for core-shell NP changes with increasing the recoil energy and temperature. Nonetheless, the Core of the core-shell NP remains intact even after getting irradiation. So, it can predict that the shell protects the core of the NP during irradiation.

5.8 References:

[1] F. Acs, S. Series, A.C. Society, Nanoparticles : Synthesis, Stabilization, Passivation, and Functionalization, (2008).

[2] F. Baletto, R. Ferrando, Structural properties of nanoclusters: Energetic, thermodynamic, and kinetic effects, Rev. Mod. Phys. 77 (2005) 371–423. https://doi.org/10.1103/RevModPhys.77.371.

[3] S. Balakrishnan, M.J. Bonder, G.C. Hadjipanayis, Particle size effect on phase and magnetic properties of polymer-coated magnetic nanoparticles, J. Magn. Magn. Mater. 321 (2009) 117–122. https://doi.org/https://doi.org/10.1016/j.jmmm.2008.08.055.

[4] M.J. Kim, Y.H. Choa, D.H. Kim, K.H. Kim, Magnetic behaviors of surface modified superparamagnetic magnetite nanoparticles, IEEE Trans. Magn. 45 (2009) 2446–2449. https://doi.org/10.1109/TMAG.2009.2018606.

[5] S. Laurent, D. Forge, M. Port, A. Roch, C. Robic, L. Vander Elst, R.N. Muller, Magnetic iron oxide nanoparticles: Synthesis, stabilization, vectorization, physicochemical characterizations and biological applications, Chem. Rev. 108 (2008) 2064–2110. https://doi.org/10.1021/cr068445e.

[6] V. Salgueiriño-Maceira, M.A. Correa-Duarte, Increasing the complexity of magnetic core/shell structured nanocomposites for biological applications, Adv. Mater. 19 (2007) 4131–4144. https://doi.org/10.1002/adma.200700418.

[7] F. Caruso, Nanoengineering of particle surfaces, Adv. Mater. 13 (2001) 11–22. https://doi.org/10.1002/1521-4095(200101)13:1<11::AID-ADMA11>3.0.CO;2-N.

[8] M.C. Daniel, D. Astruc, Gold Nanoparticles: Assembly, Supramolecular Chemistry, Quantum-Size-Related Properties, and Applications Toward Biology, Catalysis, and Nanotechnology, Chem. Rev. 104 (2004) 293–346. https://doi.org/10.1021/cr030698+.

[9] C.F. Hoener, K.A. Allan, A.J. Bard, A. Campion, M.A. Fox, T.E. Mallouk, S.E. Webber, J.M. White, Demonstration of a shell-core structure in layered CdSe-ZnSe small particles by x-ray photoelectron and Auger spectroscopies, J. Phys. Chem. 96 (1992) 3812–3817. https://doi.org/10.1021/j100188a045.

[10] A. Mews, A. Eychmueller, M. Giersig, D. Schooss, H. Weller, Preparation, characterization, and photophysics of the quantum dot quantum well system CdS/HgS/CdS, J. Phys. Chem. 98 (1994) 934–941. https://doi.org/10.1021/j100054a032.

[11] P. Scodeller, V. Flexer, R. Szamocki, E.J. Calvo, N. Tognalli, H. Troiani, A. Fainstein, Wired-enzyme core-shell Au nanoparticle biosensor, J. Am. Chem. Soc. 130 (2008) 12690–12697. https://doi.org/10.1021/ja802318f.

[12] T. Hirakawa, P. V. Kamat, Charge separation and catalytic activity of Ag@TiO2 core-shell composite clusters under UV-irradiation, J. Am. Chem. Soc. 127 (2005) 3928–3934. https://doi.org/10.1021/ja042925a.

[13] Y. Pihosh, I. Turkevych, K. Mawatari, N. Fukuda, R. Ohta, M. Tosa, K. Shimamura, E.G. Villora, T. Kitamori, Ubiquitous element approach to plasmonic enhanced photocatalytic water splitting: The case of Ti@TiO_2 core-shell nanostructure, Nanotechnology. 25 (2014). https://doi.org/10.1088/0957-4484/25/31/315402.

[14] S.I. Nikitenko, T. Chave, C. Cau, H.P. Brau, V. Flaud, Photothermal Hydrogen Production Using Noble-Metal-Free Ti@TiO2 Core-Shell Nanoparticles under Visible-NIR Light Irradiation, ACS Catal. 5 (2015) 4790–4795. https://doi.org/10.1021/acscatal.5b01401.

[15] W. Jiang, J.A. Sundararajan, T. Varga, M.E. Bowden, Y. Qiang, J.S. McCloy, C.H. Henager, R.O. Montgomery, In situ study of nanostructure and electrical resistance of nanocluster films irradiated with ion beams, Adv. Funct. Mater. 24 (2014) 6210–6218. https://doi.org/10.1002/adfm.201400553.

[16] L. Signorini, L. Pasquini, L. Savini, R. Carboni, F. Boscherini, E. Bonetti, A. Giglia, M. Pedio, N. Mahne, N. Mahne, S. Nannarone, S. Nannarone, Size-dependent oxidation in iron/iron oxide core-shell nanoparticles, Phys. Rev. B - Condens. Matter Mater. Phys. 68 (2003) 1–8. https://doi.org/10.1103/PhysRevB.68.195423.

[17] Schmitt & Segert, 基因的改变NIH Public Access, Bone. 23 (2008) 1–7. https://doi.org/10.1016/j.msec.2009.09.003.Surface.

[18] S.R. Phillpot, A.C. Antony, L. Shi, M.L. Fullarton, T. Liang, S.B. Sinnott, Y. Zhang, S.B. Biner, Charge Optimized Many Body (COMB) potentials for simulation of nuclear fuel and clad, Comput. Mater. Sci. 148 (2018) 231–241. https://doi.org/10.1016/j.commatsci.2018.02.041.

[19] J.A. Rodríguez, J. Evans, J. Graciani, J.B. Park, P. Liu, J. Hrbek, J.F. Sanz, High water-gas shift activity in TiO 2(110) supported Cu and Au nanoparticles: role of the oxide and metal particle size, J. Phys. Chem. C. 113 (2009) 7364–7370. https://doi.org/10.1021/jp900483u.

[20] Y.T. Cheng, T.R. Shan, T. Liang, R.K. Behera, S.R. Phillpot, S.B. Sinnott, A charge optimized many-body (comb) potential for titanium and titania, J. Phys. Condens. Matter. 26 (2014). https://doi.org/10.1088/0953-8984/26/31/315007.

[21] P. Panagiotopoulou, D.I. Kondarides, X.E. Verykios, Mechanistic study of the selective methanation of CO over Ru/TiO 2 catalyst: Identification of active surface species and reaction pathways, J. Phys. Chem. C. 115 (2011) 1220–1230. https://doi.org/10.1021/jp106538z.

[22] E. Lira, J.O. Hansen, L.R. Merte, P.T. Sprunger, Z. Li, F. Besenbacher, S. Wendt, Growth of Ag and Au nanoparticles on reduced and oxidized rutile TiO 2(110) surfaces, Top. Catal. 56 (2013) 1460–1476. https://doi.org/10.1007/s11244-013-0141-z.

[23] R.P. Galhenage, H. Yan, S.A. Tenney, N. Park, G. Henkelman, P. Albrecht, D.R. Mullins, D.A. Chen, Understanding the nucleation and growth of metals on TiO2: Co compared to Au, Ni, and Pt, J. Phys. Chem. C. 117 (2013) 7191–7201. https://doi.org/10.1021/jp401283k.

[24] S. Plimpton, Fast Parallel Algorithms for Short-Range Molecular Dynamics, J. Comput. Phys. 117 (1995) 1–19. https://doi.org/https://doi.org/10.1006/jcph.1995.1039.

[25] A. Stukowski, Visualization and analysis of atomistic simulation data with OVITO-the Open Visualization Tool, Model. Simul. Mater. Sci. Eng. 18 (2010). https://doi.org/10.1088/0965-0393/18/1/015012.

[26] L. Theil Kuhn, A. Bojesen, L. Timmermann, K. Fauth, E. Goering, E. Johnson, M. Meedom Nielsen, S. Mørup, Core-shell iron–iron oxide nanoparticles: magnetic properties and interactions, J. Magn. Magn. Mater. 272–276 (2004) 1485–1486. https://doi.org/https://doi.org/10.1016/j.jmmm.2003.12.189.

[27] P. Hirel, Atomsk: A tool for manipulating and converting atomic data files, Comput. Phys. Commun. 197 (2015) 212–219. https://doi.org/https://doi.org/10.1016/j.cpc.2015.07.012.

[28] J.E. Basconi, M.R. Shirts, Effects of temperature control algorithms on transport properties and kinetics in molecular dynamics simulations, J. Chem. Theory Comput. 9 (2013) 2887–2899. https://doi.org/10.1021/ct400109a.

[29] P.F. Zou, R.F.W. Bader, A topological definition of a Wigner–Seitz cell and the atomic scattering factor, Acta Crystallogr. Sect. A. 50 (1994) 714–725. https://doi.org/10.1107/S0108767394003740.

[30] A. Arjhangmehr, S.A.H. Feghhi, Irradiation deformation near different atomic grain boundaries in α-Zr: An investigation of thermodynamics and kinetics of point defects, Sci. Rep. 6 (2016) 1–14. https://doi.org/10.1038/srep23333.

[31] X.M. Bai, A.F. Voter, R.G. Hoagland, M. Nastasi, B.P. Uberuaga, Efficient annealing of radiation damage near grain boundaries via interstitial emission, Science (80-.). 327 (2010) 1631–1634. https://doi.org/10.1126/science.1183723.

[32] X. Li, W. Liu, Y. Xu, C.S. Liu, Q.F. Fang, B.C. Pan, J.L. Chen, G.N. Luo, Z. Wang, An energetic and kinetic perspective of the grain-boundary role in healing radiation damage in tungsten, Nucl. Fusion. 53 (2013). https://doi.org/10.1088/0029-5515/53/12/123014.

[33] A. Arjhangmehr, S.A.H. Feghhi, A. Esfandiyarpour, F. Hatami, An energetic and kinetic investigation of the role of different atomic grain boundaries in healing radiation damage in nickel, J. Mater. Sci. 51 (2016) 1017–1031. https://doi.org/10.1007/s10853-015-9432-z.

[34] Q. Li, X. Peng, T. Peng, Q. Tang, X. Zhang, C. Huang, Molecular dynamics simulation of Cu/Au thin films under temperature gradient, Appl. Surf. Sci. 357 (2015) 1823–1829. https://doi.org/https://doi.org/10.1016/j.apsusc.2015.10.051.

[35] D.A. Terentyev, L. Malerba, R. Chakarova, K. Nordlund, P. Olsson, M. Rieth, J. Wallenius, Displacement cascades in Fe-Cr: A molecular dynamics study, J. Nucl. Mater. 349 (2006) 119–132. https://doi.org/10.1016/j.jnucmat.2005.10.013.

[36] X. Zhang, K. Hattar, Y. Chen, L. Shao, J. Li, C. Sun, K. Yu, N. Li, M.L. Taheri, H. Wang, J. Wang, M. Nastasi, Radiation damage in nanostructured materials, Prog. Mater. Sci. 96 (2018) 217–321. https://doi.org/10.1016/j.pmatsci.2018.03.002.

Chapter 6: Summary and Conclusion

This study contributes to the research in identifying the irradiation effects on nanomaterials. To meet the objective, research was mainly focused on the study defect distribution in nanomaterials due to irradiation. As this field of research is directly related to Nano Nuclear Technology (NNT), a literature review was done and presented in this dissertation, which unveils the ongoing study and research so far in this field. The present work studies irradiation cascades in Fe Nanoparticle and core-shell Ti-TiO_2 nanoparticles using atomic level method: molecular dynamics. The production, evolution, and dynamics of defects in nanoparticles have been explored. Several mechanisms of defect formation in nanoparticles have been discovered.

We observed defect structures in Fe NP that have not been observed before, which could serve as the radiation detection used in nuclear reactors. This work has shown that the radiation creates a small number (average 0.114 % SIAs and 0.122% Vs for 40 keV) of defects. The defects are either single SIAs or Vs. In each of the cases, they produce one chunk of a big cluster. The cluster of SIAs stays near the nanoparticle's surface; however, the Vs one stays inside the nanoparticle. The Fe SIA clusters, which remain near the surface, possibly could be used to predict the reason for NP structure change and cluster formation during the irradiation. The Vs clusters inside the NPs also be used to anticipate the formation of voids in the irradiated BCC Fe NP.

For the first time, we did an MD simulation on core-shell Ti-TiO_2 NPs and discussed high energy radiation effects, which could serve as the radiation detection used in nuclear reactors. This work has shown that the radiation creates defects, and the defects are either SIAs or Vs. Surviving defects increase with increasing neutron energy and temperature. On average, 59% of vacancies and 64% of interstitials defect gather at the core and shell interface of the NPs,

and the rest of the defects stay either surface or bulk side. In all cases, mean square displacement for core-shell NP changes with increasing the recoil energy and temperature.

Nonetheless, the Core of the core-shell NP remains intact even after getting irradiation. So, it can predict that the shell protects the core of the NP during irradiation. Since, in most of the cases, cores of NP are stable even after irradiation and property of nanoparticles at high temperature open new doors for application as radiation sensing material to monitor radiation fluxes in the high-temperature core of nuclear reactors and could positively contribute to the assurance of enhanced safety of the future reactors.

Appendix A: Supplemental materials

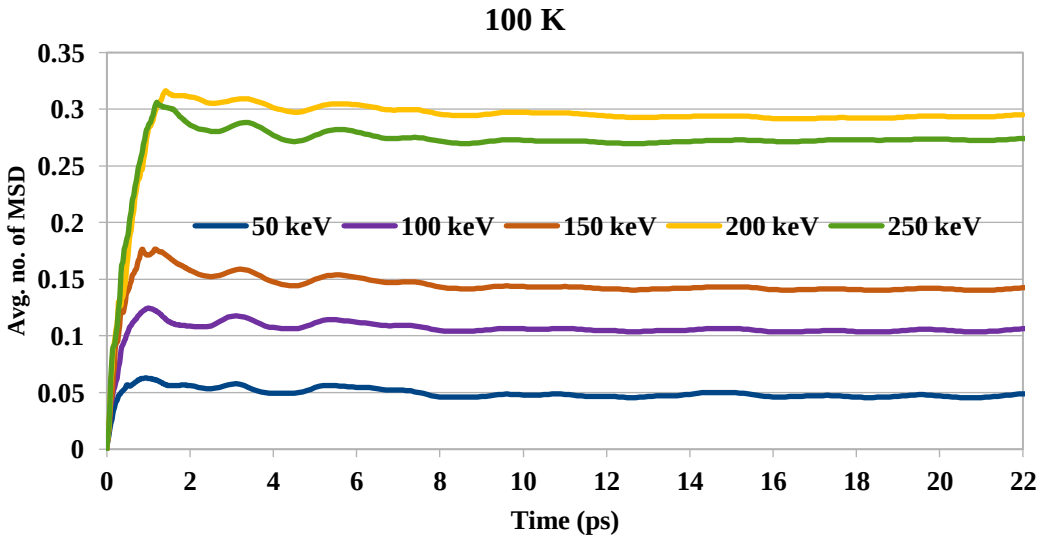

Mean square displacement as a function of simulation time for several recoil energy for 100K.

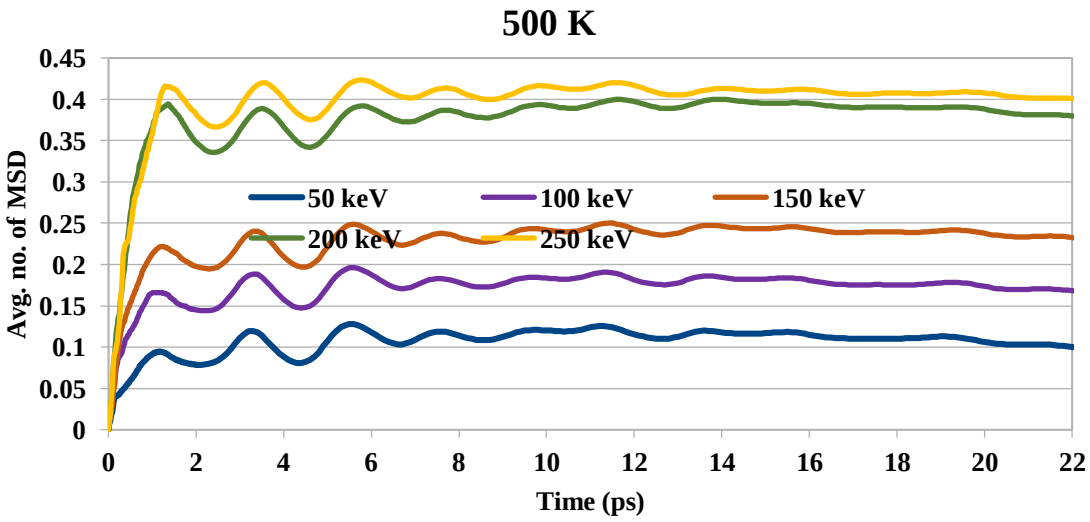

Mean square displacement as a function of simulation time for several recoil energy for 500K.